

UNIVERSITY OF CALIFORNIA

Santa Barbara

Electron Emission Spectroscopy of InGaN/GaN Light Emitting Diodes

A dissertation submitted in partial satisfaction of the  
requirements for the degree Doctor of Philosophy  
in Materials

by

Justin Thomas Iveland

Committee in charge:

Professor James Speck, Chair

Professor Claude Weisbuch

Professor Steven P. DenBaars

Professor Umesh K. Mishra

September 2015

The dissertation of Justin Thomas Iveland is approved.

---

Umesh K. Mishra

---

Steven P. DenBaars

---

Claude Weisbuch

---

James Speck, Chair

August 2015

Electron Emission Spectroscopy of InGaN/GaN Light Emitting Diodes

Copyright © 2015

by

Justin Iveland

## ACKNOWLEDGEMENTS

*To Ashley,*

*for keeping me grounded and reminding me of what is important*

**Curriculum Vitae  
Justin T. Iveland  
August 2015**

**Education**

*University of California Santa Barbara* 2011-present

Doctor of Philosophy, Material Science

*University of California Santa Barbara* 2006-2009

Bachelor of Science, Physics

*Allen Hancock College* 2004-2006

Associates, Transfer Studies

**Work & Research Experience**

Graduate Student Researcher 2011-present

Materials Department, UC Santa Barbara

Process Engineer 2009-2011

Soraa Inc., Fremont CA

Undergraduate Research 2008-2009

Materials Department, UC Santa Barbara

Interoperability Engineering Intern 2007-2008

Occam Networks Inc.

Undergraduate Research 2007

Physics Department, UC Santa Barbara

## Honors/Awards

**Outstanding Graduate Student Reacher** 2013  
UC Santa Barbara, Solid State Lighting and Energy Center

**IEE Research Communication Committee** 2013  
UC Santa Barbara, Institute for Energy Efficiency

## Conference Presentations

**Justin Iveland**, Marco Piccardo, Lucio Martinelli, Jacques Peretti, James S. Speck, Claude Weisbuch “Electron Emission Spectroscopy from Nitride Materials and Structures”  
27<sup>th</sup> International Symposium on Compound Semiconductors 2015

**Justin Iveland**, Marco Piccardo, Lucio Martinelli, Jacques Peretti, Joo Won Choi, Nathan Young, Shuji Nakamura, James S. Speck, Claude Weisbuch “Electron Emission Spectroscopy from Nitride Materials and Structures”  
56<sup>th</sup> Electronic Materials Conference 2014

Marco Piccardo, Lucio Martinelli, **Justin Iveland**, James S. Speck, Claude Weisbuch and Jacques Peretti “Use of Electron Emission Spectroscopy to Determine the First Satellite Valley in the Conduction Band of Wurtzite GaN”  
SPIE Photonics West 2014

## Publications

- [1] C. Weisbuch, M. Piccardo, L. Martinelli, **J. Iveland**, J. Peretti, and J. S. Speck, “The efficiency challenge of nitride light-emitting diodes for lighting,” *Phys. Status Solidi* **15**, n/a – n/a (2015) [doi:10.1002/pssa.201431868].
- [2] M. Piccardo, **J. Iveland**, L. Martinelli, S. Nakamura, J. W. Choi, J. S. Speck, C. Weisbuch, and J. Peretti, “Low-energy electro- and photo-emission spectroscopy of GaN materials and devices,” *J. Appl. Phys.* **117**(11), 112814 (2015) [doi:10.1063/1.4913928].

- [3] **J. Iveland**, M. Piccardo, L. Martinelli, J. Peretti, J. W. Choi, N. Young, S. Nakamura, J. S. Speck, and C. Weisbuch, “Origin of electrons emitted into vacuum from InGaN light emitting diodes,” *Appl. Phys. Lett.* **105**(5), 052103 (2014) [doi:10.1063/1.4892473].
- [4] J. Peretti, C. Weisbuch, **J. Iveland**, M. Piccardo, L. Martinelli, and J. S. Speck, “Identification of Auger effect as the dominant mechanism for efficiency droop of LEDs,” K. P. Streubel, H. Jeon, L.-W. Tu, and M. Strassburg, Eds., 90030Z (2014) [doi:10.1117/12.2038698].
- [5] M. Piccardo, L. Martinelli, **J. Iveland**, N. Young, S. P. DenBaars, S. Nakamura, J. S. Speck, C. Weisbuch, and J. Peretti, “Determination of the first satellite valley energy in the conduction band of wurtzite GaN by near-band-gap photoemission spectroscopy,” *Phys. Rev. B* **89**(23), 235124 (2014) [doi:10.1103/PhysRevB.89.235124].
- [6] **J. Iveland**, L. Martinelli, J. Peretti, J. S. Speck, and C. Weisbuch, “Direct Measurement of Auger Electrons Emitted from a Semiconductor Light-Emitting Diode under Electrical Injection: Identification of the Dominant Mechanism for Efficiency Droop,” *Phys. Rev. Lett.* **110**(17), 177406 (2013) [doi:10.1103/PhysRevLett.110.177406].
- [7] A. M. Limarga, **J. Iveland**, M. Gentleman, D. M. Lipkin, and D. R. Clarke, “The use of Larson–Miller parameters to monitor the evolution of Raman lines of tetragonal zirconia with high temperature aging,” *Acta Mater.* **59**(3), 1162–1167, Acta Materialia Inc. (2011) [doi:10.1016/j.actamat.2010.10.049].
- [8] M. C. Schmidt, C. Poblenz, Y. Chang, B. Li, M. J. Mondry, **J. Iveland**, M. R. Krames, R. Craig, J. W. Raring, et al., “High performance blue and green laser diodes based on nonpolar / semipolar bulk GaN substrates,” *SPIE Proc.* **8039**, 1–8 (2011) [doi:10.1117/12.884458].
- [9] J. W. Raring, M. C. Schmidt, C. Poblenz, Y.-C. Chang, M. J. Mondry, B. Li, **J. Iveland**, B. Walters, M. R. Krames, et al., “High-Efficiency Blue and True-Green-Emitting Laser Diodes Based on Non- c -Plane Oriented GaN Substrates,” *Appl. Phys. Express* **3**(11), 112101 (2010) [doi:10.1143/APEX.3.112101].

## ABSTRACT

### Electroemission Spectroscopy of InGaN/GaN Light Emitting Diodes

by

Justin Thomas Iveland

The effect of efficiency droop in light emitting diodes (LEDs) is a huge roadblock for consumer lighting adoption. To prevent loss of efficiency from droop, LEDs must be operated at lower current density, requiring a larger epitaxial area and increasing the overall cost. Proposed mechanisms responsible for droop include, among others, carrier delocalization from indium rich regions, overshoot and leakage current, and Auger recombination. Current methods used to understand droop mechanisms are indirect, and often rely on models that have no unique solution. It is clear that a direct measurement method and a deeper understanding of the fate of injected carriers not contributing to radiative recombination is needed to focus improvement efforts on materials and structures to help identify and mitigate the relevant droop mechanism(s). By analyzing the energy of vacuum emitted electrons from a forward biased LED, we can gain direct information of their origin internally.

The study of vacuum emitted electrons has existed for almost 130 years with the discovery of the photoelectric effect. Advancements in electron energy analysis techniques have led to

the direct measurement of conduction band structures and transport properties in many commonly used semiconductors such as: InP, GaAs, Si, and recently GaN.

The kinetic energy of the vacuum emitted electrons from an InGaN/GaN LED was analyzed and three peaks were identified: First, a low energy peak, resulting from photoexcited electrons generated by diode light. Second, a mid-energy peak, generated by the accumulation of thermalized electrons at the bottom of the  $\Gamma$  conduction band valley. Third, a high-energy peak is generated by an accumulation of electron at the bottom of a low lying side-valley “L”. Auger recombination is uniquely identifiable as it is the only proposed droop mechanism capable of generating hot carriers and solely responsible for the population of electrons found in the L-valley.

Two control experiments were carried out to strengthen our interpretation. First a simple GaN *pn* junction was measured and generated only a single  $\Gamma$ -valley peak. Second, selective detection of photoemission under modulated light from an LED in forward bias confirms that only the low energy peak is photogenerated and that LED light incapable of generating the higher energy  $\Gamma$  or L-valley peaks. Lastly, we discuss the new UCSB electron energy analyzer as well as some proposed future experiments to advance the electron emission technique.

# Contents

<b>Chapter 1: Introduction</b> .....	1
<b>1.1 Efficiency Droop in InGaN/GaN LEDs</b> .....	1
<b>1.2 Droop Mechanisms</b> .....	4
<b>1.3 Motivation to Measure Electrons Directly</b> .....	8
<b>1.4 Measuring Electrons Emitted into Vacuum</b> .....	10
<b>1.5 Negative Electron Affinity</b> .....	12
<b>1.6 Photoemission of Electrons</b> .....	13
<b>1.7 Electroemission of Electrons</b> .....	15
<b>1.8 Electron Energy Analysis for LED Droop Mechanisms</b> .....	16
<b>References</b> .....	17
<b>Chapter 2: Electroemission from InGaN LEDs</b> .....	23
<b>2.1 Introduction and Background</b> .....	23
<b>2.2 LED Samples &amp; Device Structure</b> .....	24
<b>2.3 Sample Preparation for NEA</b> .....	24
<b>2.4 Analyzer and Measurement</b> .....	25
<b>2.5 Energy Position and Scale</b> .....	28
<b>2.6 Measured Energy Distribution Curves</b> .....	28
<b>2.7 Modification of Peaks by Band Bending Region</b> .....	29
<b>2.8 Field Distortion Correction</b> .....	31
<b>2.9 Peak Shift with Applied Diode Voltage</b> .....	32
<b>2.10 Assignment of Peaks</b> .....	35
<b>2.11 <math>\Gamma</math>-L Transfer</b> .....	38

<b>2.12 Connecting Electron Current and Diode Light Intensity</b> .....	40
<b>2.13 Other Sources of Hot Electrons</b> .....	42
<b>2.14 Conclusions</b> .....	43
<b>References</b> .....	43
<b>Chapter 3: Electroemission Control Experiments</b> .....	46
<b>3.1 Introduction and Background</b> .....	46
<b>3.2 LED Sample &amp; Device Structure</b> .....	47
<b>3.3 Sample Preparation for NEA</b> .....	48
<b>3.4 Experimental Setup for Lock-in Detection</b> .....	49
<b>3.5 Measured EDCs</b> .....	50
<b>3.6 Measured Lock-in EDCs</b> .....	54
<b>3.7 Measurement of the <i>pn</i> Junction</b> .....	55
<b>3.8 Independent Measurements of the L-valley</b> .....	55
<b>References</b> .....	59
<b>Chapter 4 Current and Future Work</b> .....	61
<b>4.1 Electroemission with UCSB Spherical Sector Analyzer</b> .....	61
<b>4.2 Improvements to Electroemission Sample Design</b> .....	63
<b>4.3 Proposed Future Experiments</b> .....	65
<b>References</b> .....	72
<b>Appendix A: UCSB Electron Energy Analyzer</b> .....	75
<b>A1 Design and Operation Principles</b> .....	75
<b>A2 Fixed Transmission Energy Mode Operation</b> .....	78
<b>A3 Fixed Field Mode Operation</b> .....	79

<b>A4 Electrostatic Einzel Lens .....</b>	<b>80</b>
<b>A5 Energy Calibration .....</b>	<b>82</b>
<b>A6 Analyzer System Operation .....</b>	<b>91</b>
<b>A7 Cesium Procedure.....</b>	<b>93</b>
<b>A8 Potential Analyzer Problems .....</b>	<b>95</b>
<b>References.....</b>	<b>98</b>
<b>Appendix B: Electroemission Device Design.....</b>	<b>99</b>
<b>B1 LED Epitaxial Structure .....</b>	<b>99</b>
<b>B2 LED Device Design.....</b>	<b>100</b>
<b>B3 Sample Cleaning for NEA cathodes .....</b>	<b>102</b>
<b>B4 Device Process .....</b>	<b>104</b>
<b>References.....</b>	<b>112</b>

# Chapter 1: Introduction

*In this section efficiency droop mechanisms in InGaN light emitting diodes are discussed as a motivation for direct measurement of electrons. A brief overview of the history of measuring vacuum emitted electrons is reviewed. Photoemission processes and the concept of negative electron affinity are discussed. Lastly, I review emission of vacuum emission of electrons by electric field; the cold cathode pn junction.*

## 1.1 Efficiency Droop in InGaN/GaN LEDs

The first light emitting diode (LED) was demonstrated by H. J. Round in 1907.[1] Round observed “yellowish” light when a bias was applied to contacts made to a SiC crystal. The advancement of modern lighting technologies utilizing LEDs, however, would have to wait almost 100 years.

The first single-crystal of GaN, which was to become the basis of modern LED lighting, was grown by Maruska and Tietjen in 1969.[2] Demonstration of electroluminescence from GaN was later reported by Pankove in 1971.[3] Realization of modern GaN based LEDs, however, faced several obstacles. First, improvements in growth of GaN on lattice

## Chapter 1: Introduction

mismatched sapphire substrates were achieved by Akasaki in 1986 with the use of an AlN nucleation layer. Second, to form a  $pn$  junction, p-type doping needed to be achieved. Conductivity of p-GaN was first demonstrated by Amano in 1989 by electron beam irradiation of Zn and Mg doped GaN.[4] It was later explained by Nakamura that p-GaN conductivity of Mg doped samples could be restored by thermal annealing which suppressed the acceptor compensation of hydrogen.[5] In 1992 the first GaN  $pn$  junction was demonstrated by Akasaki.[6] Demonstration of the first high efficiency blue LED occurred in 1993 with work done by Nakamura.[7] This first viable blue LED was based on InGaN/GaN double heterostructure (DH), soon replaced by multiple quantum wells, which would eventually be the basic structure used for high efficiency solid state lighting.

Modern LEDs utilize a combination of heterostructures containing alloys from the AlN-GaN-InN system. By using different combinations of these alloys, the band gap structure within an LED can be engineered. With a room temperature band gap of around 0.77 eV [8], InN can be alloyed with GaN whose room temperature band gap is around 3.4 eV [9]. The resulting InGaN alloy has a reduced band gap allowing for the creation of light that spans the visible range. InGaN based quantum wells (QWs), which are used in modern LEDs, were first demonstrated by Nakamura in 1995.[10] AlN has a room temperature band gap of around 6.3 eV and can be alloyed with GaN to increase the band gap.[11] AlGaN alloys are used for a variety of application including electron blocking layers (EBLs) or to create barriers or wells for shorter wavelength LEDs. The basic epitaxial structure of a modern LED is shown below in **Fig. 1.1**.

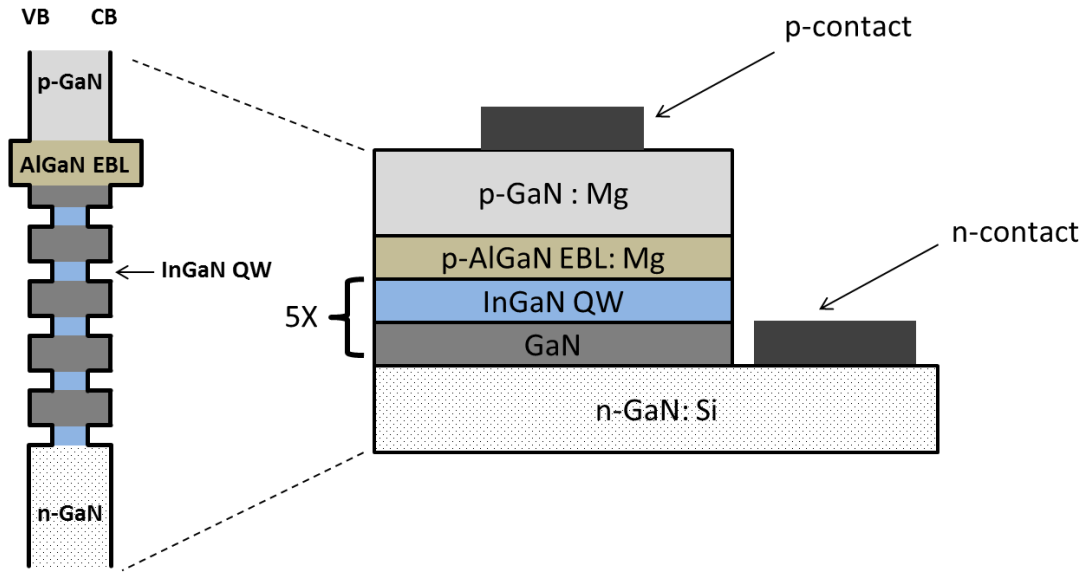


*Fig. 1.1* Figure showing the basic epitaxial structure of an LED.

A phenomenon known as efficiency droop is possibly the largest roadblock in preventing InGaIn/GaN LEDs from fully penetrating the consumer lighting market. Droop is a loss of efficiency at high carrier concentrations, associated with high current densities. This loss of efficiency is characterized by a sub-linear increase in optical power with increasing current. Efficiency droop was first reported around 1999 in InGaIn/GaN LEDs by Krames *et al.* and Mukai *et al.* [12], [13] The effects of droop require devices to be operated at lower current densities, thereby increasing the epitaxial area for a given desired lumen output, and as a result, increasing the LED cost. Efficiency droop can occur at current densities  $<10\text{A}/\text{cm}^2$  depending on device and materials configuration.[14], [15]

The efficiency droop in question is the decrease of internal quantum efficiency (IQE). IQE is defined as the following ratio[16]:

$$\eta_{IQE} = \frac{\# \text{ of photons emitted from active region per unit time}}{\# \text{ of electron - hole pairs injected into LED per unit time}}$$

## Chapter 1: Introduction

After generating a photon in the active region, it must escape the LED into free space. The efficiency of photon escape is given by extraction efficiency (EXE) defined by:

$$\eta_{EXE} = \frac{\# \text{ of photons emitted from LED into free space per unit time}}{\# \text{ of photons emitted in active region per unit time}}$$

In experiments that measure droop by electroluminescence, external quantum efficiency (EQE) is observed. EQE is the product of IQE and EXE:

$$\eta_{EQE} = \eta_{IQE} * \eta_{EXE}$$

### 1.2 Droop Mechanisms

When efficiency droop is observed in electro-luminescence experiments, the loss of efficiency corresponds to a loss in IQE. This is assuming that electrical injection and light extraction remain constant with drive current; a good assumption in a well-designed device, where the current injection is uniform over the device. The exact cause of efficiency droop (loss of IQE), however, remains controversial. Purposed mechanisms can be broken down into three main groups: Carrier delocalization [17], [18], carrier overflow/leakage [19], [20] and Auger recombination [21]–[23].

Let us start by discussing carrier de-localization. It would be a consequence of the alloy compositional fluctuations that can exist in the InGaN quantum wells (QWs) of an LED as measured by has been measured by atom probe tomography.[24] As a result of these fluctuations a potential landscape exists that can localize carriers in indium rich regions. In may be the reason why InGaN QWs exhibit a high quantum efficiency, despite having a large concentration of dislocations, much higher than other light emitting systems.[25] Indium rich

## Chapter 1: Introduction

regions may localize carriers, increasing the effective carrier concentration and radiative recombination rate, and at the same time carrier are prevented from reaching non-radiative centers. At high carrier concentrations, these localization centers are screened or filled and carriers can spill out into defect rich regions and can recombine non-radiatively. These alloy rich regions can also have implications on Auger recombination as well. An increase in Auger recombination rate at a given carrier density can occur due to a high local carrier density in the low potential (high Indium concentration) regions. [26]. Indium composition fluctuations in a quantum well region are shown schematically in **Fig. 1.2 right**.

Carrier leakage or carrier overshoot is another proposed mechanism that can be responsible for efficiency droop. [19], [20] Carrier overshoot occurs when electrons (or holes) are not captured by the InGaN quantum wells without recombining. As carriers miss these active high radiative recombination regions they end up in defect rich regions, such as the quantum well barrier region or p-GaN region. In these regions the radiative recombination rate is decreased and recombination occurs non-radiatively. Carrier leakage can also occur when electrons pass through or over an electron or hole blocking layer. It is believed that leakage occurs more easily for electrons as the hole has a larger effective mass and lower concentration.[27] An electron blocking layer (EBL) consists of a wider band gap material (AlGaN) is often employed to prevent electrons from leaving the active region and recombining non-radiatively with holes in the p-GaN. The effectiveness of EBLs is questionable in some structures where hole injection efficiency into the active region may be hindered by the EBL. [28] In addition, there may be alloy composition fluctuations in the

## Chapter 1: Introduction

AlGa<sub>x</sub>N barrier region. These variations in composition can allow for percolation pathways for electrons through the EBL, limiting their effectiveness.[29], [30]. It may also be possible for electrons to tunnel through the EBL region into the p-GaN. Carrier overshoot of a quantum well and carrier leakage through an EBL is shown in **Fig.1.2 center**.

Auger recombination, a three particle process, is another mechanism that has been proposed as the cause of efficiency droop.[21] In an Auger recombination process an electron and hole recombines, but rather than generating a photon, energy is given to a third carrier as kinetic energy. In an electron-electron-hole (eeh) process the recombination energy is given to an electron in the conduction band. In an electron-hole-hole process (ehh), the recombination energy is given to a hole in the valence band. The eeh and ehh processes are shown in **Fig.1.2 left**.

Both the eeh and ehh process can promote a carrier into the same band as the initial state or a different band, intra-band or inter-band respectively. It is believed, due to the large band gap and the requirement of momentum and energy conservation that an inter-band processes is dominant. [23] Even when allowing for inter-band scattering to occur, the Auger recombination rate is only large for a narrow range of Indium mole fractions in the In<sub>x</sub>Ga<sub>1-x</sub>N QW that that give hot electrons that are in resonance with a higher conduction band at 2.5eV. Calculations, however, of the higher conduction position around 2.5 eV are in question as we will discuss later in this document. Further, droop is observed over a large range of Indium mole fractions. [31] To account for this discrepancy, it has been suggested that indirect Auger recombination plays a large role in the GaN system.[22], [32] In an indirect Auger process,

## Chapter 1: Introduction

momentum is provided by scattering with a lattice phonon, by charged defects, or by alloy scattering. Calculations show that for indium mole fractions within the visible range, an eh processes is dominant, with phonon scattering being the primary scattering mechanism. [22]

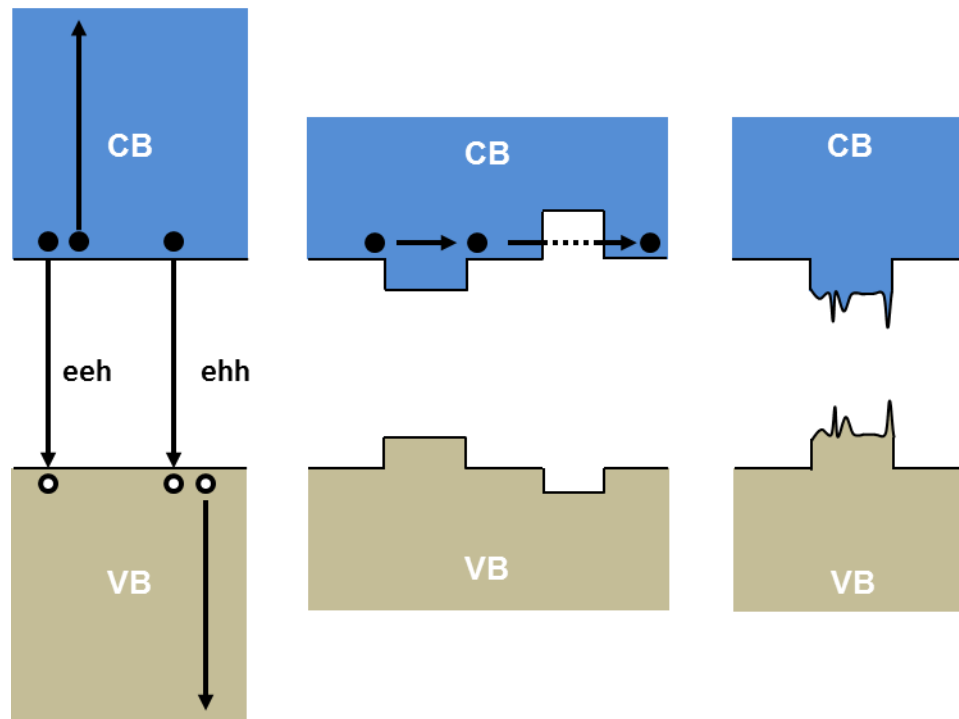


**Fig. 1.2** Figure showing the three proposed mechanism responsible for efficiency droop. (left) Auger recombination: An electron and hole recombine giving their energy to a third carrier an electron in the conduction band ( $e-e-h$ ) or hole in the valence band ( $e-h-h$ ). (Center) Carrier Overshoot: Electrons or holes overcome a quantum well region. Carrier leakage: electrons leak through an, electron blocking layer, hole blocking layers. (right) Carrier localization: Alloy fluctuations in the quantum well region generate localization centers.

### 1.3 Motivation to Measure Electrons Directly

Thus far, methods used to understand recombination processes in an LED rely upon measurements of emitted light in electroluminescence or photoluminescence as well as diode current voltage curves. Typically an EQE curve plotted as a function of current density ( $J$ ) is measured and fitted to a polynomial (ABC) model.[33] This polynomial contains the radiative and non-radiative recombination rates, which are each a function of carrier concentration. To obtain a fitting, an assumption must be made that the extraction efficiency (EXE) does not vary with current density. Constant EXE is a requirement to extract IQE as a function of current density. The system of equations relating current density and IQE are given by:

$$J = qd(An + Bn^2 + Cn^3)$$

$$\eta_{IQE} = \frac{Bn^2}{An + Bn^2 + Cn^3}$$

Here  $q$  is the electron charge,  $d$  is the active layer thickness,  $n$  is the carrier concentration,  $B$  is the radiative recombination coefficient,  $A$  and  $C$  are the non-radiative the Shockley-Read-Hall and Auger coefficients respectively.

Unfortunately, many assumptions must be made. For instance, for a given radiative recombination rate ( $Bn^2$ ) many different values for Shockley-Read-Hall and Auger ( $An$  and  $Cn^3$ ) can be found to fit the same EQE vs  $J$  curve, which has no unique solution. Furthermore, these rate coefficients do not take into account the non-homogeneities in the InGaN/GaN system. [17], [18] Aside from alloy fluctuations, non-uniform injection in the quantum wells can occur, as well as current crowding.[34] The ABC model assumes an active region volume

## Chapter 1: Introduction

that is unchanged at all current densities. If current crowding is occurring in the device, the active volume changes as a function of current density (yielding higher current densities near the contact). Current crowding, non-uniform injection, and alloy fluctuations all have the same effect on the ABC model calculation, a higher carrier concentration is present at a given current density than what is calculated from a space averaged current injection. An underestimate of the carrier concentration results in a higher effective Auger (C) coefficient needed for the curve fitting, leading to large discrepancies with the theoretical calculation.

More detailed studies, however, can be performed using time resolved photoluminescence or electroluminescence.[21], [31], [35] Time resolved studies involve optically pumping resonantly the active region into the droop regime or by applying a small AC voltage on top of the diode voltage. In the EL study it is shown that the non-radiative recombination rate scales roughly at  $n^3$  pointing to an Auger process as the culprit.[35] In addition, in the resonant photoluminescence studies droop is still observed with carriers just excited in the quantum well, ruling out leakage as a possible source. [21] Strong evidence of hot electrons, generated by Auger, exists in other studies as well. In photoluminescence, Binder et al. resonantly pumped a green quantum well and observed UV luminescence from a nearby UV quantum well populated at high carrier concentrations by Auger generated hot electrons.[36]

It is clear that a better understanding of the creation and eventual fate hot electrons created by non-radiative processes is important to improve device design. Auger recombination is unique amongst the proposed droop processes because it would generate hot electrons that could be measured. The eeh Auger process in 3nm thick  $\text{In}_{0.18}\text{Ga}_{0.82}\text{N}$  quantum wells (QWs)

## Chapter 1: Introduction

(which radiatively emit blue light at 2.75 eV under electrical injection) would produce a hot electron. The initial energy of the Auger electron is approximately 2.75 eV above the ground state electron level of the QW. The energy difference between the InGaN QW electron ground state and the bottom of the  $\Gamma$  point in the surrounding bulk GaN is estimated at 350 meV. The hot electron will, therefore, be launched from the QWs with an initial energy of 2.4 eV above the bottom of the conduction band in the bulk p-GaN layer. This uses rough estimates for the ground state level and the InGaN/GaN conduction band (CB) discontinuity.[37] By measuring the kinetic energy of electrons in the LED structure, it should therefore be possible to distinguish an eeh Auger process from other droop mechanisms. This can be achieved by analyzing the energy of electrons emitted in vacuum from an LED.

### **1.4 Measuring Electrons Emitted into Vacuum**

It was discovered almost 130 year ago, in 1887 by H. Hertz, that electrons could be photo-excited and emitted from a metal with ultraviolet light. [38] In the 20<sup>th</sup> century Einstein explained the photoelectric effect through the introduction of the concept of light quanta, the photons.[39] This meant that the photo-emitted electron energy is dependent on the frequency of exciting light and not on the light intensity. The relationship between energy and frequency of the exciting light photon is given by Planck's constant.

Experimental verification of Planck's constant occurred in 1916 with work done by Millikan. By measuring electron current between two metal plates at different applied bias and with varying exciting frequency Millikan was able to experimentally measure Planck's

## Chapter 1: Introduction

constant.[40], [41] An important result from of this measurement is that the measured electron kinetic energy is referenced to the work function of the collector (anode) and not dependent on emitter (cathode) work function. [42] This is important because the kinetic energy of emitted electrons is unchanged after being emitted into vacuum. Thus, to measure electron energy one only needs a calibrated value of the collector (anode) work function. This will be discussed further in later sections of this document.

In 1930 the quantum efficiency of these early metal cathodes was greatly increased with the discovery of the Cs-O-Ag cathode.[43] Other alkali metal cathodes followed, with increasing quantum efficiency.[44] The advent of semiconductor cathodes such as Cs<sub>3</sub>Sb further increased quantum efficiency. [45] In a semiconductor cathode, a band gap exists. The presence of this band gap will change the dominant scattering mechanism from electron-electron (in the case of a metal) to electron-phonon. In a metal, excited electrons can quickly lose energy through electron-electron scattering (producing e-h pairs of any energy). In a semi-conductor, however, there are far fewer electrons, and e-e collisions do not play a role. [46] As electron-electron scattering is not available, electrons lose their energy much more slowly from electron-phonon scattering, with each scattering event resulting in only a small energy loss (~35 meV for LO-phonon emission in GaAs).[47]

In 1965 a huge leap forward in quantum efficiency occurred with the discovery of the cesiated semiconductor cathode.[48] With their GaAs-Cs photocathode, Scheer and van Laar were able to demonstrate efficiency of greater than 50% for excitation energies a several times large than  $E_g$ .

## 1.5 Negative Electron Affinity

Electron affinity ( $\chi_A$ ) is defined as the energy required to excite an electron from the bottom of the conduction band into vacuum (to energy  $E_{vac}$ ). It was first shown in 1965 by Scheer and van Laar that a small layer of cesium can lower the vacuum level at the surface to below the conduction band level in the bulk. This condition is referred to as “negative electron affinity” NEA. NEA is achieved not just by the addition of low work function cesium, but by the negative downward band bending found in a p-type material whose Fermi level is pinned in the gap. A bare p-type surface and a cesiated p-type surface are shown in **Fig.1.3**. A further decrease in the electron affinity can be achieved by introducing oxygen to generate a cesium oxygen complex.[49] For GaAs the sample is cesiated, oxygen is introduced, and the sample then re-cesiated. Repeated cycles of cesiation, oxygenation, de-cesiation by heating, is repeated until subsequent cesiation no longer decreases the affinity. It is believed that the cesium or cesium-oxygen complex generates a surface dipole to lower the vacuum level.[47], [49]

The exact nature of the surface and the role of oxygen in forming the surface dipole are poorly understood. [50] W. E Spicer, a pioneer in the field, comments on this topic: “The most notable weakness in our fundamental knowledge of the NEA photocathodes is almost entirely associated with the Cs oxide surface layer and the interface between it and the 3-5 material.”[51] Part of this confusion is the role oxygen plays if and how it migrates on the surface or possibly tunnels under the cesium after introduction.[49] Further, it is speculated

## Chapter 1: Introduction

that the Cs<sub>2</sub>O complex has a smaller lattice constant than cesium metal, therefore the introduction of oxygen may increase the dipole moment density.[52] A further complication arises from surface preparation and termination. The exact Fermi level pinning position (and as a result the surface band bending) is dependent on both intrinsic surface states and modified metal induced states from the addition of cesium. [50], [53] For instance, some authors report a change in band bending upon cesiation and other do not.[54], [55] Doping will also play a role in surface band bending, as it can also influence the pinning position.[56] All these complexities, however, do not change the energy reference to the Fermi level in the bulk (away from the surface and band bending region) which will be discussed later in this document.

Having a photo-cathode brought into NEA dramatically increases the quantum efficiency by increasing the escape depth of an electron.[50] Any cathode operating with a positive electron affinity requires an electron in the conduction band to overcome the barrier  $\chi_A$ . The escape depth is short because an electron must still be hot from its initial creation energy to overcome this barrier. Electrons excited far from the surface cannot escape, as they will thermalize below  $\chi_A$  before reaching the surface. In an NEA cathode, the electrons can thermalize to the bottom of the conduction band diffuse to the surface and still escape as the vacuum level sits below the conduction band.

### **1.6 Photoemission of Electrons**

After NEA preparation techniques were established, direct measurement of bulk thermalized electrons became possible. The ability to measure electrons from the bottom of

## Chapter 1: Introduction

the conduction band upward allowed for a direct measurement of conduction band structures. In a photoemission experiment, light is shined onto a cesiated p-type semiconductor promoting electrons from the valence band into the conduction band. Cesium-GaAs NEA photocathodes are common and are the basis for many technologies, including photomultiplier tubes and night vision goggles.[57]

For suitably high incident photon energy excitation of valence band electrons into high density of states side conduction band valleys may be efficient. [58], [59] After electron scatter into conduction band side-valleys they are long lived as the  $\Gamma$ -valley  $\rightarrow$ side-valley transfer rate is much faster than the side-valley  $\rightarrow$   $\Gamma$ -valley back rate. [60], [61] Conduction band and side-conduction band valleys were measured in photoemission for GaAs.[58], [62], [63] Photoemission measurement to establish conduction band structure has also been applied to InP. [64] More recently Piccardo et al. measured conduction band energy using cesiated p-GaN; this will be discussed in more detail later in this document. [65]

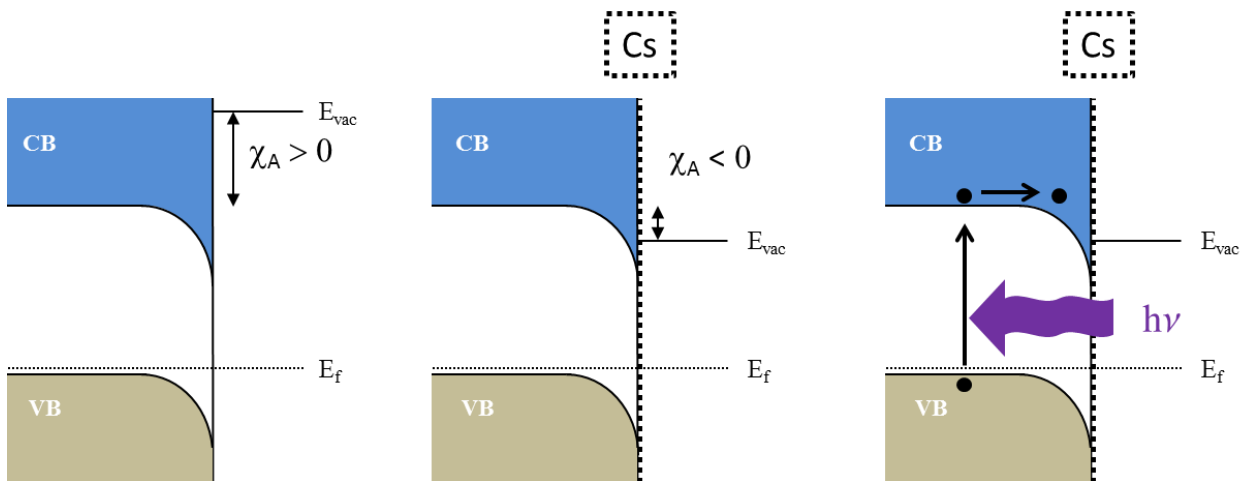


*Fig. 1.3 Showing a p-type surface (left), a p-type surface activated into NEA by cesiation (center), photoemission process for an NEA p-type surface (right).*

## 1.7 Electroemission of Electrons

An electron can be promoted into vacuum by electrical bias, rather than photo-excitation. Such emission is termed electroemission. Cold cathode emitters have been studied as a possible replacement for hot filament cathodes that are widely used in electron microscopy, cathode ray tubes, vacuum tubes, etc. Hot cathodes emit electrons by thermionic emission by heating a filament to high temperatures. Cold cathodes emit electrons by applying an electric bias. Cold cathode emitters existed as early as 1961 when Mead demonstrated a Tunnel-Emission device.[66] In 1969, after the realization of NEA, Williams and Simon demonstrated a  $pn$  junction cold cathode based on GaAs.[67] Later in 1973, Kohn demonstrated a silicon based  $pn$  junction cold cathode.[68] More recently in 2002, a GaN based  $pn$  junction cold cathode was demonstrated by Shaw et al. [69]

The basic principle behind an NEA  $pn$  junction cold cathode is the following: Upon applying a positive bias to the cathode (p-type) and a negative bias to the anode (n-type), electrons are injected from the cathode and holes from the anode. Electrons that pass beyond the depletion region into the p-type material are then minority carriers. These electrons can then diffuse through the p-type layer to the surface. In NEA, the vacuum level sits below the conduction band in the bulk which means that any excess electrons that have reached the

surface and pass through the band bending region (BBR) are able to escape. An un-biased and forward biased  $pn$  junction cold cathode is shown in **Fig.1.4**.

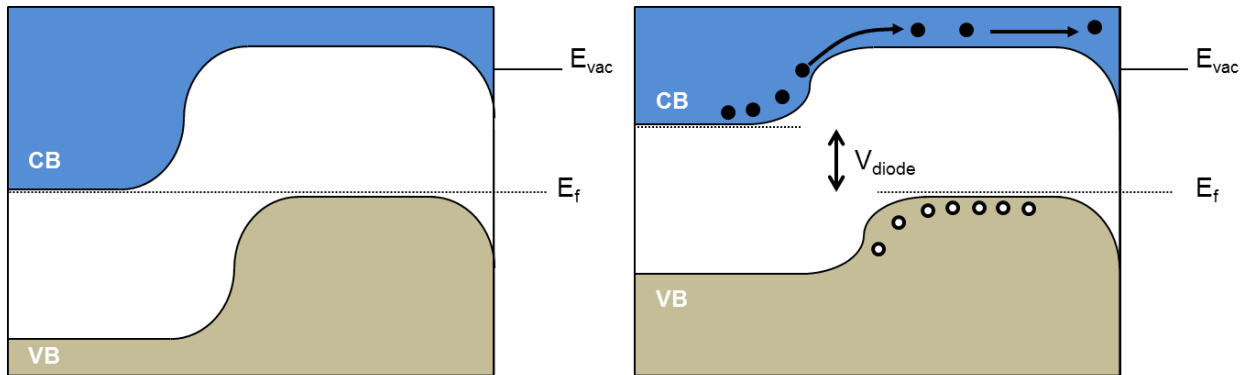


*Fig. 1.4* Figure showing an un-biased (left) and biased (right)  $pn$  junction.

## 1.8 Electron Energy Analysis for LED Droop Mechanisms

When an LED is driven into the droop regime, a large number of carriers recombining non-radiatively should be present. Some of these carriers will end up in the p-type region as minority carrier. By achieving negative electron affinity we have a method of probing these conduction band electrons as they escape into vacuum. Leakage and overshoot processes will generate a population of leakage electrons, which are already observed in the cold cathode  $pn$  junction. As discussed above an eeh Auger process will be uniquely identifiable as it generates a hot electron. By observing the energy and population of vacuum emitted we will have a better understanding of their origin and the role different droop mechanisms play in LED efficiency droop.

## Chapter 1: Introduction

### References

- [1] H. J. Round, "A note on carborundum," *Electr. World*, p. 309, 1907.
- [2] H. P. Maruska and J. J. Tietjen, "The preparation and properties of vapor-deposited single-crystal-line GaN," *Appl. Phys. Lett.*, vol. 15, no. 10, pp. 327–329, 1969.
- [3] J. I. Pankove, E. a. Miller, D. Richman, and J. E. Berkeyheiser, "Electroluminescence in GaN," *J. Lumin.*, vol. 4, no. 1, pp. 63–66, 1971.
- [4] H. Amano, M. Kito, K. Hiramatsu, and I. Akasaki, "P-Type Conduction in Mg-Doped GaN Treated with Low-Energy Electron Beam Irradiation (LEEBI)," *Jpn. J. Appl. Phys.*, vol. 28, no. Part 2, No. 12, pp. L2112–L2114, 1989.
- [5] S. Nakamura, N. Iwasa, and M. Senoh, "Method of manufacturing P-type compound semiconductor," US5306662 A1994.
- [6] I. Akasaki, H. Amano, K. Itoh, N. Koide, and K. Manabe, "GaN based UV/blue light-emitting devices," *Inst. Phys. Conf. Ser.*, vol. 129, no. 851, 1992.
- [7] S. Nakamura, M. Senoh, and T. Mukai, "P-GaN/N-InGaN/N-GaN Double-Heterostructure Blue-Light-Emitting Diodes," *Jpn. J. Appl. Phys.*, vol. 32, pp. L8–L11, 1993.
- [8] V. Y. Davydov, A. A. Klochikhin, R. P. Seisyan, V. V. Emtsev, S. V. Ivanov, F. Bechstedt, J. Furthmüller, H. Harima, a. V. Mudryi, J. Aderhold, O. Semchinova, and J. Graul, "Absorption and emission of hexagonal InN. Evidence of narrow fundamental band gap," *Phys. Status Solidi Basic Res.*, vol. 229, no. 3, pp. 1972–1974, 2002.
- [9] B. Monemar, "Fundamental energy gap of GaN from photoluminescence excitation spectra," *Phys. Rev. B*, vol. 10, no. 2, pp. 676–681, 1974.
- [10] S. Nakamura, N. Senoh, N. Iwasa, and S. I. Nagahama, "High-Brightness InGaN Blue, Green and Yellow Light-Emitting-Diodes with Quantum-Well Structures," *Japanese J. Appl. Phys. Part 2-Letters*, vol. 34, no. 7A, pp. L797–L799, 1995.
- [11] F. Yun, M. a. Reshchikov, L. He, T. King, H. Morkoç, S. W. Novak, and L. Wei, "Energy band bowing parameter in Al<sub>x</sub>Ga<sub>1-x</sub>N alloys," *J. Appl. Phys.*, vol. 92, no. 8, pp. 4837–4839, 2002.
- [12] M. R. Krames, G. Christenson, D. Collins, L. W. Cook, M. G. Craford, A. Edwards, R. M. Fletcher, N. Gardner, W. Goetz, W. Imler, E. Johnson, R. S. Kern, R. Khare, F. A. Kish, C. Lowery, M. J. Ludowise, R. Mann, M. Maranowski, S. Maranowski, P. S. Martin, S. O'Shea, D. Steigerwald, J. Thompson, J. J. Wierer, J. Yu, D. Basile, Y. Chang, G. Hasnain, M. Hueschen, K. Killeen, C. Kocot, S. Lester, J. Miller, J. Rosner, R. Schneider, T. Takeuchi,

## Chapter 1: Introduction

- and T. S. Tan, “High-brightness AlGaInN light-emitting diodes,” *SPIE Proc.*, vol. 3938, 2000.
- [13] T. Mukai, M. Yamada, and S. Nakamura, “Characteristics of InGaN-Based UV / Blue / Green / Amber / Red Light-Emitting Diodes,” *Jpn. J. Appl. Phys.*, vol. 38, no. 7, pp. 3976–3981, 1999.
- [14] J. Hader, J. V. Moloney, B. Pasenow, S. W. Koch, M. Sabathil, N. Linder, and S. Lutgen, “On the importance of radiative and Auger losses in GaN-based quantum wells,” *Appl. Phys. Lett.*, vol. 92, no. 26, p. 261103, 2008.
- [15] S.-C. Ling, T.-C. Lu, S.-P. Chang, J.-R. Chen, H.-C. Kuo, and S.-C. Wang, “Low efficiency droop in blue-green m-plane InGaN/GaN light emitting diodes,” *Appl. Phys. Lett.*, vol. 96, no. 23, p. 231101, 2010.
- [16] E. F. Schubert, “Light-Emitting Diodes,” in *Light-Emitting Diodes Second Edition*, Second., Cambridge University Press, 2006, pp. 86–87.
- [17] S. Chichibu, T. Sota, K. Wada, S. Nakamura, N. This, and I. Introduction, “Exciton localization in InGaN quantum well devices,” *J. Vac. Sci. Technol. B*, vol. 16, no. 4, pp. 2204–2214, 1998.
- [18] B. Monemar and B. E. Sernelius, “Defect related issues in the ‘current roll-off’ in InGaN based light emitting diodes,” *Appl. Phys. Lett.*, vol. 91, no. 18, p. 181103, 2007.
- [19] M.-H. Kim, M. F. Schubert, Q. Dai, J. K. Kim, E. F. Schubert, J. Piprek, and Y. Park, “Origin of efficiency droop in GaN-based light-emitting diodes,” *Appl. Phys. Lett.*, vol. 91, no. 18, p. 183507, 2007.
- [20] U. Ozgur and H. Morkoç, “GaN-Based Light-Emitting Diodes: Efficiency at High Injection Levels,” *Proc. IEEE*, vol. 98, no. 7, pp. 1180–1196, Jul. 2010.
- [21] Y. C. Shen, G. O. Mueller, S. Watanabe, N. F. Gardner, a. Munkholm, and M. R. Krames, “Auger recombination in InGaN measured by photoluminescence,” *Appl. Phys. Lett.*, vol. 91, no. 14, p. 141101, 2007.
- [22] E. Kioupakis, P. Rinke, K. T. Delaney, and C. G. Van de Walle, “Indirect Auger recombination as a cause of efficiency droop in nitride light-emitting diodes,” *Appl. Phys. Lett.*, vol. 98, no. 16, p. 161107, 2011.
- [23] K. T. Delaney, P. Rinke, and C. G. Van De Walle, “Auger recombination rates in nitrides from first principles,” *Appl. Phys. Lett.*, vol. 94, no. 19, 2009.

## Chapter 1: Introduction

- [24] R. Shivaraman, Y. Kawaguchi, S. Tanaka, S. P. Denbaars, S. Nakamura, and J. S. Speck, "Comparative analysis of 20-21 and 20-2-1 semipolar GaN light emitting diodes using atom probe tomography," *Appl. Phys. Lett.*, vol. 102, no. 25, 2013.
- [25] S. D. Lester, F. a. Ponce, M. G. Craford, and D. a. Steigerwald, "High dislocation densities in high efficiency GaN-based light-emitting diodes," *Appl. Phys. Lett.*, vol. 66, no. 10, pp. 1249–1251, 1995.
- [26] T.-J. Yang, R. Shivaraman, J. S. Speck, and Y.-R. Wu, "The influence of random indium alloy fluctuations in indium gallium nitride quantum wells on the device behavior," *J. Appl. Phys.*, vol. 116, no. 11, p. 113104, 2014.
- [27] K. J. Vampola, M. Iza, S. Keller, S. P. DenBaars, and S. Nakamura, "Measurement of electron overflow in 450 nm InGaN light-emitting diode structures," *Appl. Phys. Lett.*, vol. 94, no. 6, pp. 2007–2010, 2009.
- [28] S.-H. Han, D.-Y. Lee, S.-J. Lee, C.-Y. Cho, M.-K. Kwon, S. P. Lee, D. Y. Noh, D.-J. Kim, Y. C. Kim, and S.-J. Park, "Effect of electron blocking layer on efficiency droop in InGaN/GaN multiple quantum well light-emitting diodes," *Appl. Phys. Lett.*, vol. 94, no. 23, p. 231123, 2009.
- [29] D. N. Nath, Z. C. Yang, C. Y. Lee, P. S. Park, Y. R. Wu, and S. Rajan, "Unipolar vertical transport in GaN/AlGaIn/GaN heterostructures," *Appl. Phys. Lett.*, vol. 103, no. 2, 2013.
- [30] C.-K. Wu, C.-K. Li, and Y.-R. Wu, "Percolation transport study in nitride based LED by considering the random alloy fluctuation," *J. Comput. Electron.*, pp. 416–424, 2015.
- [31] A. David and M. J. Grundmann, "Influence of polarization fields on carrier lifetime and recombination rates in InGaIn-based light-emitting diodes," *Appl. Phys. Lett.*, vol. 97, no. 3, p. 033501, 2010.
- [32] E. Kioupakis, P. Rinke, A. Schleife, F. Bechstedt, and C. G. Van de Walle, "Free-carrier absorption in nitrides from first principles," *Phys. Rev. B*, vol. 81, no. 24, pp. 2–5, Jun. 2010.
- [33] H.-Y. Ryu, D.-S. Shin, and J.-I. Shim, "Analysis of efficiency droop in nitride light-emitting diodes by the reduced effective volume of InGaIn active material," *Appl. Phys. Lett.*, vol. 100, no. 13, p. 131109, 2012.
- [34] A. David, M. J. Grundmann, J. F. Kaeding, N. F. Gardner, T. G. Mihopoulos, and M. R. Krames, "Carrier distribution in (0001)InGaIn/GaN multiple quantum well light-emitting diodes," *Appl. Phys. Lett.*, vol. 92, no. 5, p. 053502, 2008.
- [35] A. David and M. J. Grundmann, "Droop in InGaIn light-emitting diodes : A differential carrier lifetime analysis," no. February, p. 103504, 2010.

## Chapter 1: Introduction

- [36] M. Binder, a. Nirschl, R. Zeisel, T. Hager, H.-J. Lugauer, M. Sabathil, D. Bougeard, J. Wagner, and B. Galler, “Identification of nnp and npp Auger recombination as significant contributor to the efficiency droop in (GaIn)N quantum wells by visualization of hot carriers in photoluminescence,” *Appl. Phys. Lett.*, vol. 103, no. 7, p. 071108, 2013.
- [37] H. Zhang, E. J. Miller, E. T. Yu, C. Poblenz, and J. S. Speck, “Measurement of polarization charge and conduction-band offset at In<sub>x</sub>Ga<sub>1-x</sub>N/GaN heterojunction interfaces,” *Appl. Phys. Lett.*, vol. 84, no. 23, p. 4644, 2004.
- [38] H. Hertz, “Ueber einen Einfluss des ultravioletten Lichtes auf die electrisch Entladung,” *Ann. Phys.*, 1887.
- [39] A. Einstein, “Über einen die Erzeugung und Verwandlung des Lichtes betreffenden heuristischen Gesichtspunkt,” *Ann. Phys.*, vol. 322, no. 6, pp. 132–148, 1905.
- [40] R. A. Millikan, “A Direct Determination of ‘h,’” *Phys. Rev.*, vol. 4, no. 1, pp. 73–75, 1914.
- [41] R. A. Millikan, “A Direct Photoelectric Determination of Plank’s ‘h,’” *Phys. Rev.*, vol. 7, no. 3, pp. 355–388, 1916.
- [42] D. Wong, P. Lee, G. Shenghan, W. Xuezhou, H. Y. Qi, and F. S. Kit, “The photoelectric effect: experimental confirmation concerning a widespread misconception in the theory,” *Eur. J. Phys.*, vol. 32, no. 4, pp. 1059–1064, 2011.
- [43] L. R. Koller, “Photoelectric emission from thin films of caesium,” *Phys. Rev.*, vol. 36, no. 11, pp. 1639–1647, 1930.
- [44] A. H. Sommer, “New Photoemissive Cathodes of High Sensitivity,” *Rev. Sci. Instrum.*, vol. 26, no. 7, p. 725, 1955.
- [45] W. E. Spicer, “Photoemissive, photoconductive, and optical absorption studies of alkali-antimony compounds,” *Phys. Rev.*, vol. 112, no. 1, pp. 114–122, 1958.
- [46] W. E. Spicer and A. Herrera-gómez, “Modern Theory and Applications of Photocathodes,” *SPIE*, 1993.
- [47] W. E. Spicer, G. Vergara, and M. Carlo, “Calculated electron energy distribution of negative electron affinity cathodes,” vol. 436, pp. 83–90, 1999.
- [48] J. J. Scheer and J. Van Laar, “GaAs-Cs: A New Type of Photoemitter,” *Solid State Commun.*, vol. 3, pp. 189–193, 1965.
- [49] R. L. Bell, *Negative Electron Affinity Devices*. London: Oxford University Press, 1973.

## Chapter 1: Introduction

- [50] W.E.Spicer, “Negative Affinity 3-5 Photocathodes: Their Physics and Technology,” *Appl. Phys.*, vol. 12, pp. 115–130, 1977.
- [51] F. J. Machuca, “A thin film p-type GaN photocathode: prospect for a high performance electron emitter,” Stanford University, 2003.
- [52] A. H. Sommer, “Cesium-Oxygen Activation of Three-Five Compound Photoemitters,” *J. Appl. Phys.*, vol. 42, no. 5, p. 2158, 1971.
- [53] P. E. Gregory and W. E. Spicer, “Photoemission studies of the GaAs-Cs interface,” *Phys. Rev. B*, vol. 12, no. 6, pp. 2370–2381, 1975.
- [54] A. A. Pakhnevich, V. V Bakin, A. V Yaz’kov, G. É. Shaibler, S. V Shevelev, O. E. Tereshchenko, A. S. Yaroshevich, and A. S. Terekhov, “Energy Distributions of Photoelectrons Emitted from p -GaN ( Cs , O ) with Effective Negative Electron Affinity,” *JETP Lett.*, vol. 79, no. 10, pp. 479–483, 2004.
- [55] M. Myckeler, W. Monch, T. U. Kampen, R. Dimitrov, O. Ambacher, and M. Stutzmann, “Negative electron affinity of cesiated p-GaN (0001)... surfaces,” *J. Vac. Sci. Technol. B*, vol. 16, no. 4, pp. 2224–2228, 1998.
- [56] M. D. Pashley, K. W. Haberern, R. M. Feenstra, and P. D. Kirchner, “Different Fermi-level pinning behavior on n- and p-type GaAs(001),” *Phys. Rev. B*, vol. 48, no. 7, pp. 4612–4615, 1993.
- [57] Hamamatsu, “Photocathode technology,” 2014. [Online]. Available: <https://www.hamamatsu.com/us/en/technology/innovation/photocathode/index.html>. [Accessed: 01-Jan-2014].
- [58] R. C. Eden, J. L. Moll, and W. E. Spicer, “Experimental Evidence For Optical Population of the X Minima in GaAs,” *Phys. Rev. Lett.*, vol. 18, no. 15, pp. 597–599, 1967.
- [59] J. Peretti, H.-J. Drouhin, D. Paget, and A. Mircea, “Band structure on indium phosphide from near-band-gap photoemission,” *Phys. Rev. B*, vol. 44, no. 15, 1991.
- [60] C. J. Stanton and D. W. Bailey, “Rate equations for the study of femtosecond intervalley scattering in compound semiconductors,” *Phys. Rev. B*, vol. 45, no. 15, pp. 8369–8377, 1992.
- [61] S. Wu, P. Geiser, J. Jun, J. Karpinski, D. Wang, and R. Sobolewski, “Time-resolved intervalley transitions in GaN single crystals,” *J. Appl. Phys.*, vol. 101, no. 4, p. 043701, 2007.
- [62] L. W. James and J. L. Moll, “Transport Properties of GaAs Obtained from Photoemission Measurements,” *Phys. Rev.*, vol. 183, no. 3, pp. 740–753, 1969.

## Chapter 1: Introduction

- [63] L. W. James, R. C. Eden, J. L. Moll, and W. E. Spicer, "Location of the L1 and X3 minima in GaAs as determined by photoemission studies," *Phys. Rev.*, vol. 174, no. 3, pp. 909–910, 1968.
- [64] L. W. James, J. P. Van Dyke, F. Herman, and D. M. Chang, "Band structure and high-field transport properties of InP," *Phys. Rev. B*, vol. 1, no. 10, pp. 3998–4004, 1970.
- [65] M. Piccardo, L. Martinelli, J. Iveland, N. Young, S. P. DenBaars, S. Nakamura, J. S. Speck, C. Weisbuch, and J. Peretti, "Determination of the first satellite valley energy in the conduction band of wurtzite GaN by near-band-gap photoemission spectroscopy," *Phys. Rev. B*, vol. 89, no. 23, p. 235124, Jun. 2014.
- [66] C. A. Mead, "Operation of tunnel-emission devices," *J. Appl. Phys.*, vol. 32, no. 4, pp. 646–652, 1961.
- [67] B. F. Williams, R. E. Simon, D. Sarnoff, and O. Gaas, "Electron Emission From A 'cold-cathode' GaAs p-n Junction," *Appl. Phys. Lett.*, vol. 14, no. 7, pp. 3–5, 1969.
- [68] E. S. Kohn, "The silicon cold cathode," *IEEE Trans. Electron Devices*, vol. 20, no. 3, pp. 321–329, Mar. 1973.
- [69] J. L. Shaw, R. E. Treece, D. Patel, C. S. Menoni, J. R. Smith, and J. I. Pankove, "Electron emission from GaN n–p junctions," *Appl. Phys. Lett.*, vol. 81, no. 16, p. 3076, 2002.

## Chapter 2: Electroemission from InGaN LEDs

### 2.1 Introduction and Background

In this section we discuss the direct measurement of Auger electrons generated by electron-hole recombination. Experiments were performed on commercial InGaN/GaN light emitting diodes (LEDs). An energy distribution of vacuum emitted electrons from a forward biased LED is measured. The occurrence of a high energy peak, observed in the energy distribution, correlates with the onset of droop and provides a direct signature of Auger electrons. The high energy peak is attributed to electron accumulation in a conduction band side-valley, labeled “L”. A mid-energy peak is observed and attributed to accumulation in the  $\Gamma$  conduction band. A third low energy peak is observed and attributed to electrons photoexcited by LED light at the surface.

## 2.2 LED Samples & Device Structure

In this current study the sample measured was an InGaN/GaN based commercial LED structure from Walsin Lihwa (Taiwan). The sample was grown by metalorganic chemical vapor deposition (MOCVD) on a flat (0001) sapphire substrate. It consisted of a several micron thick undoped buffer layer, followed by a Si-doped n-type buffer, an 8 period  $\text{In}_{0.18}\text{Ga}_{0.82}\text{N}/\text{GaN}$  multiple quantum well (QW) stack. QW thickness was approximately 3 nm with 10 nm thick GaN barriers. The sample also contained a 40 nm thick  $\text{Al}_{0.15}\text{Ga}_{0.85}\text{N}$  electron blocking layer (EBL). After the EBL a 200 nm thick p-type layer was grown with approximate doping of:  $[\text{Mg}] = 1.8 \times 10^{20} \text{ cm}^{-3}$ . More details on the epitaxial structure can be found elsewhere. [Appendix B]

Devices were fabricated in a mesa style LED structure, dry etching down to contact the n-GaN. A large n-side contact consisted of a Ti/Pt electrode. The p-type contact, that defined the injection area, was a  $500 \mu\text{m} \times 500 \mu\text{m}$  square contact. The p-type electrode was Pt. Inside the p-contact an array of  $27 \times 27$   $10 \mu\text{m}$  holes exposed the p-GaN surface. A large contact pad, isolated from the GaN with  $\text{SiO}_2$  was used to contact the p-contact. The isolated p-contact pad was Ti/Pt. More details of the device structure and fabrication can be found elsewhere. [Appendix B]

## 2.3 Sample Preparation for NEA

After fabrication, the processed LEDs were prepared for negative electron affinity (NEA). The samples were first cleaned with organic solvents, acetone and isopropanol, then rinsed

## Chapter 2: Electroemission from InGaN LEDs

with deionized water. The samples were then introduced into a nitrogen purged glove box. Inside the glove box samples were cleaned in an HCL-isopropanol solution described in more detail elsewhere. [1], Appendix B After cleaning, samples were introduced into a vacuum load lock and pumped down. Samples were then transferred into the ultra-high vacuum (UHV) analyzer chamber. After transfer the samples were annealed at 260 °C for approximately 30 minutes.

After the sample cools down, cesiation was performed to achieve NEA. Cesium was deposited using a SAES Getters dispenser placed approximately 6 cm from the sample surface. Optimization of the NEA surface was performed by monitoring the total electron emission current over time. The electron current was measured on a highly positive biased grid placed approximately 6 cm from the sample surface. Appendix A

### 2.4 Analyzer and Measurement

Electron energy distribution curves (EDCs) were measured using a cylindrical electron energy analyzer described elsewhere.[2] Note: this analyzer differs slightly from that described in appendix A; however, the basic operation and energy selection is identical. The analyzer was operated in fixed pass energy mode keeping the analyzer pass energy ( $\phi_{\text{Analyzer}}$ ) constant throughout the measurement. At fixed pass energy, a slice of the electron distribution is able to pass through the analyzer. To obtain an energy distribution, a potential known as the cathode potential ( $V_{\text{cathode}}$ ) is varied with respect to ground to either accelerate or de-accelerate electron to fall within the analyzer pass energy ( $\phi_{\text{Analyzer}}$ ). The cathode potential is set on the

## Chapter 2: Electroemission from InGaN LEDs

p-contact so all electron energies are therefore referenced to the bulk p-GaN Fermi Level. [Appendix A] The LED bias ( $V_{\text{Bias}}$ ) potential was then referenced to the cathode potential ( $V_{\text{cathode}}$ ). Analyzer and LED bias are shown in **Fig. 2.2**.

The electrons that passed through the analyzer at a selected energy were measured as current on a gold faraday cup. The analyzer was operated at an energy resolution of approximately 50 meV. The energy calibration of the analyzer pass energy ( $\phi_{\text{Analyzer}}$ ) was performed by looking at the position of the Fermi step in photoemission using a clean cesiated gold surface as a reference sample.[3] Appendix A The calibrated analyzer pass energy ( $\phi_{\text{Analyzer}}$ ) was measured to be around 4.8 eV. The energy of emitted electrons measured from the Fermi level of the p-type material is established by taking the calibrated analyzer pass energy ( $\phi_{\text{Analyzer}}$ ) and adding to the applied cathode potential ( $V_{\text{Cathode}}$ ).

$$E - E_F = \phi_{\text{Analyzer}} + qV_{\text{Cathode}}$$

The sample surface work function ( $\phi_{\text{Surface}}$ ) can be defined as the separation between the Fermi level to vacuum. **Figure 2.1** shows the cathode potential set to allow electrons that are just at the vacuum level to pass through the analyzer. After cesiation, the sample work function ( $\phi_{\text{Surface}}$ ) was measured to be approximately 2.3 eV. The initial cesiation conditions remained stable for several days throughout the measurement.

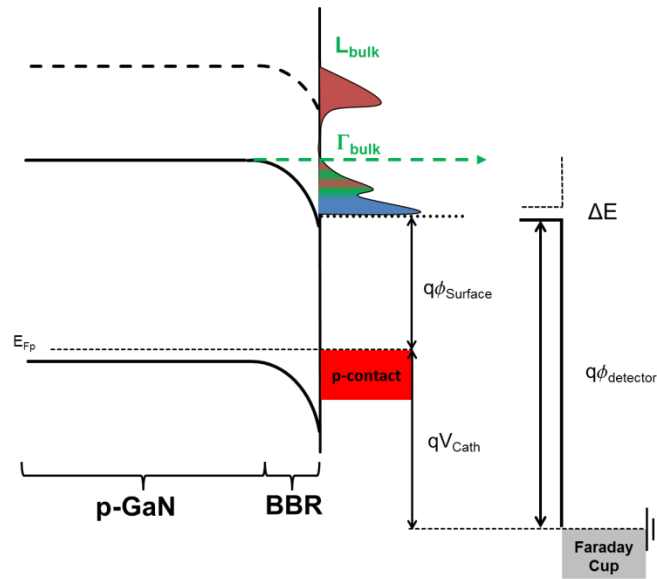


*Fig. 2.1* Figure showing the cathode potential set to just allow electrons at the vacuum to pass through the analyzer.

Energy distribution curves (EDCs) were measured at several diode current values. For high diode current, devices were pulsed at low duty cycle to prevent self-heating. The total electron collection current was confirmed to be proportional to pulse duty cycle. At each diode current, total electron current (cathode current) was also recorded. Electroluminescence (EL) from the diode was taken during the measurement, via optical access through a hole in the analyzer rotator shown in **Fig. 2.2**.

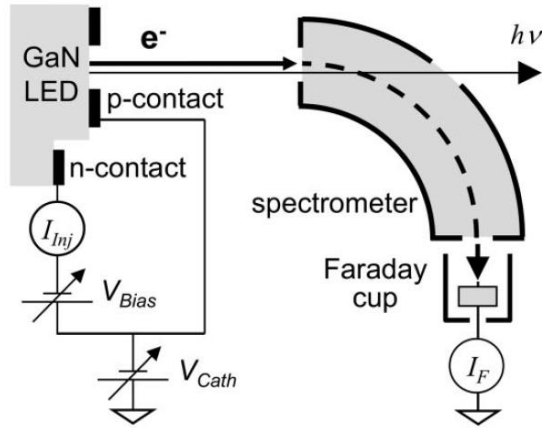


**Fig. 2.2** Showing the spectrometer, faraday cup, sample bias and cathode bias. The sample bias ( $V_{Bias}$ ) is set relative to the cathode bias ( $V_{Cath}$ ). Analyzer potentials are fixed.

## 2.5 Energy Position and Scale

In the section above we described how all our measured electron energies are referenced to the p-GaN Fermi level. To obtain an electron energy distribution that is referenced to the vacuum kinetic energy we simple need to shift the spectra by the distance from the Fermi level to the vacuum level, the surface work function ( $\phi_{Surface}$ ). At the vacuum level electrons escape with zero kinetic energy, below the vacuum level electrons cannot escape. Spectra shown in **Fig. 2.3** are plotted as a function of their vacuum kinetic energy.

## 2.6 Measured Energy Distribution Curves

Measured EDCs are shown in **Fig. 2.3**, electron current is plotted as a function of electron kinetic energy in eV referenced to the vacuum level. Electroemission spectra are measured at

## Chapter 2: Electroemission from InGaN LEDs

room temperature for different applied LED currents. At high diode current above 16mA the LED is pulsed to prevent self-heating. Emitted electron current for pulsed high diode current measurements is corrected for the duty cycle. Measurements made at high diode current result in a decreased signal to noise ratio is observed the reason for this decrease is discussed below.

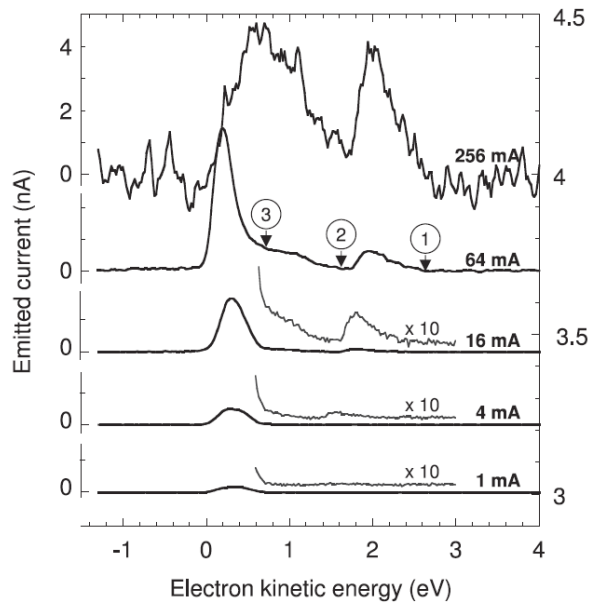


**Fig. 2.3** Measured EDCs from forward biased LED. Electron kinetic energy (in eV) is plotted as a function of emitted electron current (nA). Inset grey curves shows curves with 10X multiplication of electron current. EDCs are plotted for 1 mA, 4 mA, 16 mA, 64 mA and 256 mA diode current.

### 2.7 Modification of Peaks by Band Bending Region

The shape of a peak measured in the EDC is modified by the surface band bending region (BBR). The BBR at the p-GaN surface is shown in **Fig. 2.4**. As electrons transit the p-GaN

they must encounter this BBR before exiting. When transiting BBR an electron can scatter and lose energy (referenced to the energy in the bulk). [4], [5]. In addition, electrons can reflect and scatter at the p-GaN/vacuum interface.

If a narrow distribution of electrons exist in the bulk will be broadened by energy relaxation in the BBR. There is, however, a fraction of the electron population that is able to transit the BBR and escape into vacuum quasi-ballistically. This quasi-ballistic population corresponds to electrons that are at the high energy threshold of a peak in the EDCs. For example, if a thermalized population of electrons at the bottom of the  $\Gamma$ -valley transits the BBR, the high energy threshold of the corresponding EDC peak will mark the position of the bottom of the bulk  $\Gamma$ -valley conduction band, as shown schematically in **Fig. 2.4**.

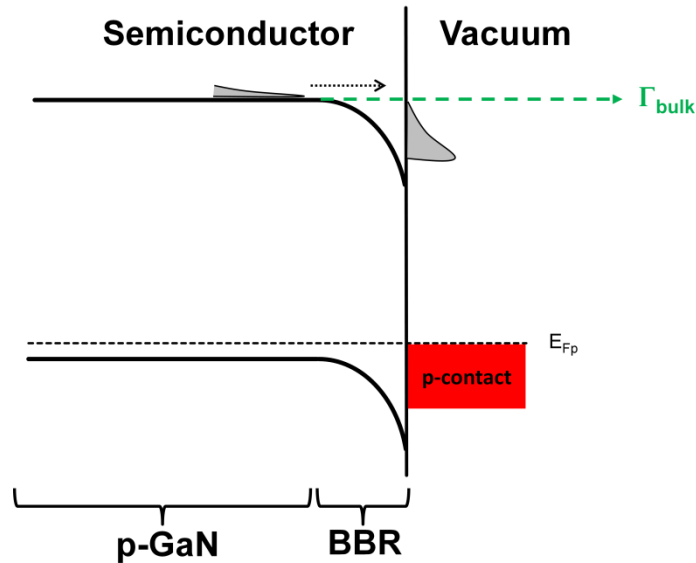


*Fig. 2.4 Schematic showing a thermal distribution of electron in the bulk at the bottom of the  $\Gamma$ -valley. Electrons are then broadened in the BBR by scattering before reaching the surface.*

## 2.8 Field Distortion Correction

The electron energy peaks observed at high diode current have a decreased signal to noise ratio. The cause of this decreased signal at high diode current has two sources: First, at high diode current the LED is pulsed at 5% duty cycle to prevent self-heating. Pulsing the LED at 5% duty cycle reduces the time average emitted electron current by 95%. The electron current that is measured at the Faraday cup is the time average current, not peak current. Second, blurring of the emitted electron beam from the LED apertures occurs due to a stray electric field that exists between the n and p-contacts. In the parallel contact geometry the n-contact is only 50 microns from the p-contact. Appendix A Electrons leaving the p-contact therefore “see” both the electric field setup by the analyzer entrance slit and the n-contact. The analyzer entrance slit potential is always positive relative to the p-contact, attracting all emitted electrons. The n-contact, however, is always negative relative to the p-contact distorting the electrons path from the p-contact to the entrance slit. At low diode currents (corresponding to low diode bias) the analyzer potential relative to the n-contact potential is large and little field distortion occurs. However, as diode bias is increased, the analyzer potential relative the n-contact potential is reduced and electron path can be altered. This stray electric field also greatly reduces the electron analyzer transmission efficiency at high diode bias and is corrected for.

The intensities of energy distribution curves needed corrected for the transmission efficiency of the analyzer which is not constant at all applied diode voltages. As diode current and diode voltage is increased the stray electric field that is present between the n-contact and

## Chapter 2: Electroemission from InGaN LEDs

p-contact increases as described above. As the electron beam is distorted at higher diode bias, the percentage of total electron current relative to the current passing through the analyzer is diminished. To account for this loss of transmission efficiency, the total emitted electron current ( $I_{\text{Total}}$ ) is measured on the entrance slit for each measurement. To obtain the transmitted electron current ( $I_{\text{Trans}}$ ), the spectra is integrated over all energies collected by the gold Faraday cup after passing through the analyzer. The transmission efficiency is then defined as the ratio of transmission current to total electron current  $T_{\text{Efficiency}}=(I_{\text{Trans}}/I_{\text{Total}})$ . All EDCs were corrected for this transmission efficiency loss by multiplying by the measured transmission efficiency ( $T_{\text{Efficiency}}$ ). In the absence of field distortion, the overall transmission efficiency of the analyzer is approximately  $10^{-3}$

### 2.9 Peak Shift with Applied Diode Voltage

The energy position of the measured peaks is shifted to higher energy with increasing applied voltage and diode current. This shift is a result of a voltage drop between the set cathode voltage ( $V_{\text{Cath}}$ ) and what is actually being applied to the p-contact and the underlying p-GaN. If the applied cathode potential is reduced, a greater set cathode potential is needed to pass the same energy electron in the absence of a voltage drop, shifting the energies to higher values.

There are two sources of resistance that result in a voltage drop (shown in **Fig.2.5** and **Fig.2.6**): First, an ohmic resistance exists between the clip (which is at the set cathode potential) contacting the sample and the p-metal contact on the sample ( $R_C$ ). This resistance

is responsible for a shift of all peaks to higher energy. The presence of the contact resistance ( $R_C$ ) results in a shift of all the spectra is because all emitted electron, those from the metal, p-GaN surface, and bulk p-GaN are referenced directly to the cathode potential. There is also a voltage drop that exists between the p-metal and the p-surface. This voltage drop is the result of a metal contact/p-GaN resistance ( $R_{C-S}$ ) shown in **Fig.2.6**.  $R_{C-S}$  is responsible for shifting only those electrons that originate in the bulk, L and  $\Gamma$ , and not the low energy peak as it originates primarily from surface generated electrons and is only subject to the ohmic voltage shift resulting from  $R_C$ . Both voltage drops increase at higher diode current as more current is passing over these two resistive points ( $R_{C-S}$  and  $R_C$ ) increasing the voltage drop.

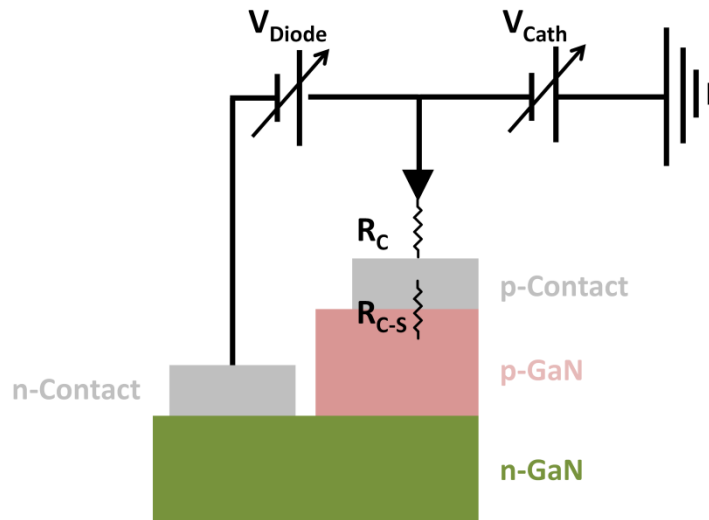


*Fig. 2.5 Showing both contact related resistances that result in voltage drops.  $R_C$  is the ohmic resistance between the set cathode voltage the contact.  $R_{C-S}$  is the resistance between the p-contact and the p-GaN surface.*

The shift in the energy position due to the ohmic voltage drop can be easily corrected for as it shifts all the peaks equally. This peak shift is performed by subtracting the ohmic voltage drop for each measurement. At low diode current (<1 mA) this voltage drop is minimal and can be assumed to be negligible. Correcting for the ohmic voltage drop and plotting the peak positions as a function of diode bias we can see that the high energy peak positions still change due to the voltage drop ( $R_{C-S}$ ), but that the energy separation remains unchanged. The peak shift shown in **Fig. 2.7**. Another important note is that only voltage drops on the p-side effect spectral shift as all electron energies are referenced to the cathode potential on the p-side. The effect of the contact voltage drop ( $R_{C-S}$ ) on the band diagram and resulting spectra is shown schematically in **Fig. 2.6**.

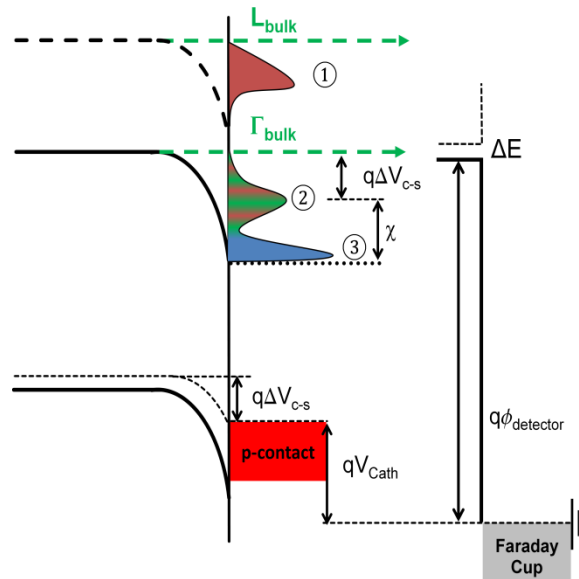


**Fig. 2.6** Figure showing the effective voltage drop between the p-contact and p-GaN ( $\Delta V_{C-S}$ ). The two high energy peak are shifted to higher energy, as a large cathode potential

is needed to overcome  $\Delta V_{C-S}$ . Note: peak positions relative to bulk Fermi level remain unchanged.

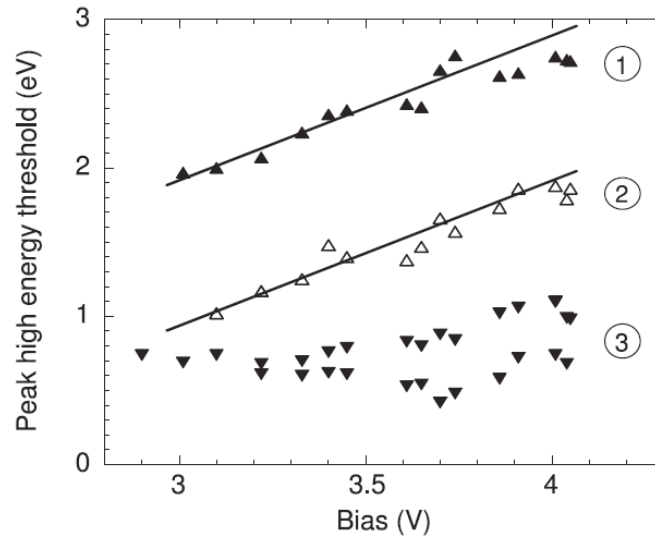


**Fig. 2.7** Figure showing the shift in all three peaks as a function of diode bias as a result of the ( $R_{C-S}$ ) voltage drop in the p-contact. Peak 3 does not shift as all peak positions have been corrected for the ( $R_C$ ) voltage drop. The distance between peaks 1 and 2 remain unchanged.

## 2.10 Assignment of Peaks

Three peaks were observed in the energy distribution of emitted electrons. The generation of these three peaks is shown schematically in **Fig. 2.8**.

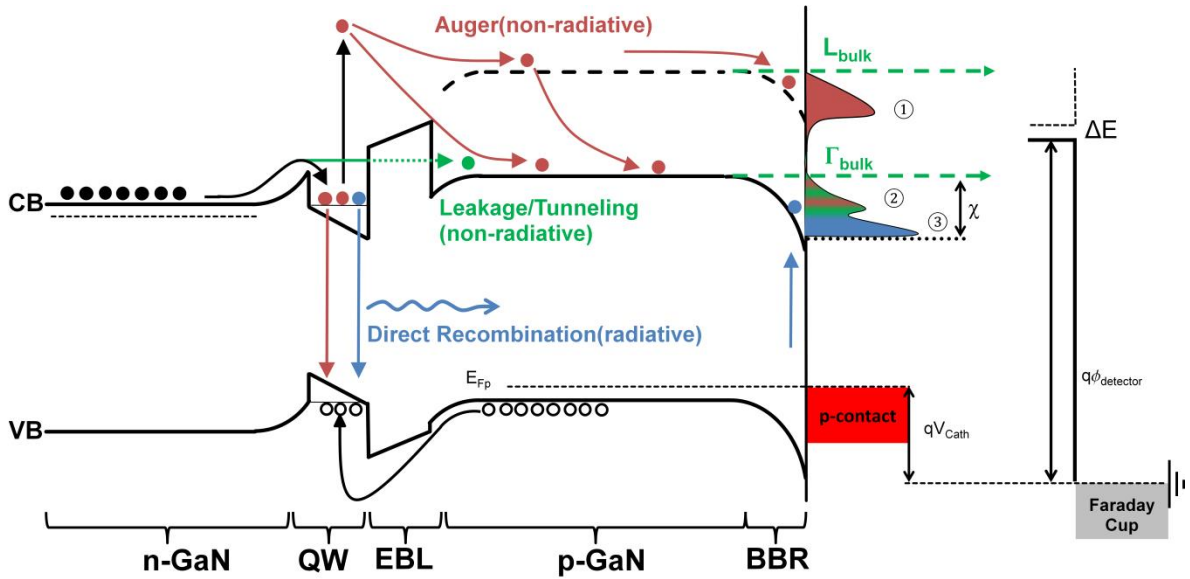


**Fig. 2.8** Showing the process that generates the three peaks observed in LED electroemission.

Peak ① is generated by accumulation of hot electrons in the side L-valley. The L-valley is populated solely by Auger electrons (red). Peak ② generated by electron accumulation in the  $\Gamma$ -valley. Auger electrons can back scatter from  $L \rightarrow \Gamma$  or can relax directly at the bottom of  $\Gamma$  (red). In addition, electrons can leak or tunnel through the EBL into the  $\Gamma$ -valley (green). Peak ③ is generated by electrons excited by sub-gap diode light, from the BBR, surface or metal p-contact (blue).

The low energy peak ③ is a result of photoemitted electrons from diode-generated light. In forward bias, the LED is emitting blue 450 nm (2.75 eV) light. This sub-gap light can excite electrons from the surface of p-GaN. [6] Electrons can be excited from defect states that are occupied within the BBR region. Electrons can also be excited directly in BBR by Franz-Keldysh effect, due to the high electric fields present. Lastly, electrons can be excited from the exposed p-contact metal. The sample sits close to the entrance slit of the analyzer. Light, generated inside the apertures can escape and reflect back onto the p-metal, or shine directly

## Chapter 2: Electroemission from InGaN LEDs

on it at the edges of the 10 micron apertures. The high energy threshold of this peak sits roughly 2.7 eV above the Fermi level, which is consistent with the excitation energy of the blue 2.75 eV diode light.

The mid-energy peak ② is attributed to electrons that have accumulated at the bottom of the  $\Gamma$ -valley conduction band. Such electrons can have two sources. First, electrons injected from the n-GaN that fail to recombine in the active region. These leakage electrons then pass over the active region and either pass over, tunnel through or find a percolation pathway through the AlGaIn electron blocking layer into the p-GaN. These electrons that have leaked can then diffuse to the surface. Second, an eeh Auger process can generate a hot electron in the active region or in the p-GaN. This hot electron can then thermalize to the bottom of the conduction band and again, diffuse to the surface. The Auger electron can have an intermediate state in a side-valley and back scatter into the  $\Gamma$ -valley, or it can originally be created in the  $\Gamma$ -valley and relax from there. At low forward bias, where the non-ohmic voltage drop is small, the high energy threshold of the mid-energy peak corresponds roughly to 3.3 eV above the Fermi level. Assuming the Fermi level is around 80 meV above the valence band maximum, this puts the electron energy close to the room temperature 3.4 eV band gap of Wurtzite GaN. [7]

The third high energy peak ① is generated by an eeh Auger process. In the forward biased LED, an electron and hole recombine, generating a hot electron which is scattered to a satellite valley “L” and quickly thermalizes. In this side-valley thermalized electrons are long lived and can diffuse to the surface to be measured. At low diode bias, where the voltage drop in

the contact is small, the high energy threshold of this L-valley peak is roughly 4.2 eV above the Fermi level in the bulk p-GaN ( $E_{Fp}$ ). This puts the  $\Gamma$ -L separation at 0.9 eV. This separation remains constant under varying diode current, as shown in **Fig. 2.7**.

### 2.11 $\Gamma$ -L Transfer

In the electroemission studies described in this thesis there is no measureable remnant of a hot Auger electron that has survived transit to the surface with its original energy. Auger electrons, however, could efficiently transfer to a side-valley. In GaN the satellite L-valley has a higher density of states and has six-fold degeneracy. The L-valley can act as an accumulation point for hot Auger electrons where they will be long lived and will survive transit to the surface. Side-valley accumulation of hot electrons has been observed by photoemission in many semiconductor systems including: GaAs [8], InP [9], Si [10] and AlN [11].

After electron scatter into conduction band side-valleys they are long lived as the  $\Gamma \rightarrow$  side-valley transfer rate is much faster than the side-valley  $\rightarrow \Gamma$  valley back rate. [12], [13] IR pump/probe measurements performed on GaN established a  $\Gamma \rightarrow$ L transfer rate of 170 fs and the return scattering rate from L  $\rightarrow \Gamma$  of 1 ps.[13] The rate that is most important to sustain an L-valley population of electrons is not the scattering rate but rather the time required to depopulate the L-valley. In GaN, depopulation of the L valley is measured to be as long as 20 ps.[13] It is believed that depopulation time of the L-valley is large as electrons in the L-valley require many attempts before finally scattering and remaining in the  $\Gamma$ -valley.[12]

## Chapter 2: Electroemission from InGaN LEDs

Auger recombination in a blue quantum well generates a hot electron with an initial energy around 2.4 eV above the conduction band minimum in  $\Gamma$ . The L- $\Gamma$  separation has been measured directly by near gap photoemission and in our electroemission measurements to be approximately 0.92 eV. [14] If a hot auger electron scatters directly to L it would be approximately 1.5 eV above the bottom of L. If we assume a scattering time of 20 fs, the mean free path between scattering events is, approximately 30 nm for such energetic high velocity electrons. The Auger electron will stay hot in L for many scattering events, in fact hot (ballistic) electrons are observed in in GaN photoemission studies when excited above the band gap.[14] The distance from the last quantum well to the surface (the p-GaN thickness) is approximately 200 nm. This means  $\approx 40$  collisions are required for an electron to reach the surface by a random walk, as the distance traveled goes as the square root of the number of collisions multiplied by the mean free path ( $R \sim l\sqrt{N}$ ). For these  $\approx 40$  collisions the time required to reach the surface is approximately 0.8 ps. Even if electrons relaxed quicker this time is quite smaller than the measured 20 ps depopulation time of the L-valley.[13] This means that electrons having scattered into L will remain in L and survive transit to the surface. Note that the measured LO scattering time is around 200 fs ( much longer than the 9 fs calculated time. [15], [16]), meaning that electrons will remain at energies such that there velocity remains high during their transit to the surface. Furthermore, a hot electron may be even longer lived if there is a further increased LO scattering time due to hot phonon effects.[16] Taking a more conservative number for the scattering time of 14 fs, would

translate into  $\approx 85$  collisions and a transit time of 1.2 ps, still allowing for a significant population of L valley electrons to reach the surface.[17]

## 2.12 Connecting Electron Current and Diode Light Intensity

Diode light intensity was monitored as a function of diode current and diode voltage for each measured EDC. The light intensity as a function of injected diode current is plotted in **Fig. 2.9**. In addition, we measure the integrated peak current for each of the three peaks as a function of diode current.

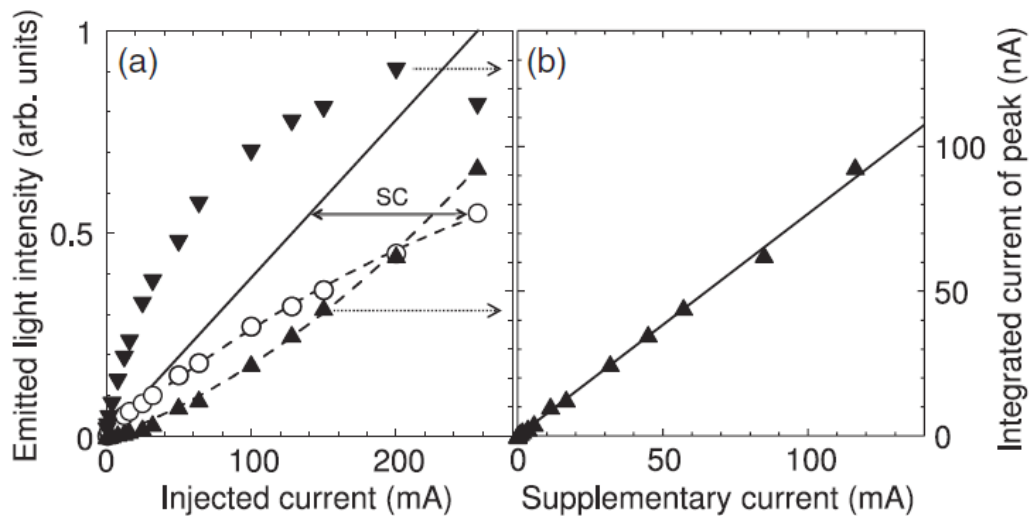


**Fig. 2.9** (a) Emitted diode light plotted as a function of diode current (○), Integrated current of high energy peak plotted as a function of diode current (▲), Integrated current of low energy peak plotted as a function of diode current (▼). The straight line is the expected optical power in the absence of droop. (b) Integrated current of high energy peak plotted as a function of supplementary current (▲).

## Chapter 2: Electroemission from InGaN LEDs

As diode current increases, the low energy peak increases sub-linearly. This is expected as the low energy peak is created by diode light and the light intensity from the diode also increases sub-linearly because of droop. The high L and  $\Gamma$ -valley (not shown) peaks have a super-linear increase with diode current.

To understand the relationship between efficiency droop and the onset of the high energy peaks, a supplementary current (SC) can be defined. The SC current is defined as the current necessary to obtain a given light output power when compared to the expected linear extrapolation of light output power that would be present in the absence of droop. When this SC current is plotted as a function of the high energy L peak a linear relationship is observed (this is the same for the  $\Gamma$ -valley peak which is proportional to the high energy L peak). Auger recombination is the only droop mechanism that scales as the cube of the carrier density. This means that the droop component of the emitted electrons and the efficiency droop observed in the LED have the same dependence on current density, thus on diode current, indicating a common origin.

The magnitude of the measured electron current when compared to the SC current is roughly 80 nA and 100 mA respectively, meaning a ratio of  $10^{-6}$ . We can make an estimate to account for the  $10^{-6}$  loss in electron current. First, most of the injected diode current under the metal p-contact with only a fraction injected in the exposed and cesiated p-GaN area. Based on simulations, at 50 mA diode current about 15% of the total current is injected into the exposed p-GaN area of the 10  $\mu\text{m}$  arrays.[18], [19] Second, after an Auger electron is generated in the InGaN QW region, half go toward the p-GaN and half toward the n-GaN.

## Chapter 2: Electroemission from InGaN LEDs

The electrons that go toward the p-region can escape to be measured, those that end up in the n-region as majority carriers do not contribute to the emitted electron current. After thermalizing into L and  $\Gamma$  a large fraction of the thermalized electrons will recombine before reaching the p-GaN surface to be emitted. If we assume a diffusion length of around 100 nm, we have approximately 10% of the electrons that are able to reach the surface. Likely, this is an overestimate of diffusion length as we have a highly doped p-region at the surface. The final obstacle for electrons to escape is their interaction with the surface. The escape probability at the surface is governed by scattering in the BBR and at the vacuum/surface interface and the uniformity of the cesiation. This escape probability is unknown, but is likely much less than 50% as this is the escape probability of highly developed photocathodes.[20]

### 2.13 Other Sources of Hot Electrons

Are there other possible mechanisms to generate  $>1$  eV hot electrons in the forward biased LED structure? Electrons can be excited to higher energy in an electric field, however, the only such field that exist in our structures is in the BBR and electron cannot be excited to an energy than their bulk value (energy must be conserved). [21] Second, electrons can be thermionically injected over a barrier, however, the only barrier that exists is the AlGaIn EBL, that this is too low (only  $\sim 200$  meV above the CBM) to generated the observed  $\sim 1$  eV electrons. Lastly, electrons can tunnel through a barrier into a high KE state, but again, the only barrier (EBL) that exists in the structure is not high enough. It is therefore believed that

Auger recombination in the active region is the only viable mechanism for generating high energy L-valley electrons.

## 2.14 Conclusions

In summary we have observed electrons emitted into vacuum from an InGaN LED brought into NEA by cesiation. Three peaks were observed in the energy distribution curves measured by an electrostatic energy analyzer. A low energy peak was attributed to photoexcitation from the surface by diode light. A mid-energy peak was generated by an accumulation of electrons in the  $\Gamma$ -valley by electron leakage or by Auger recombination. The third high energy peak was attributed to electron accumulation in the satellite L-valley, populated by Auger electrons. Lastly, the population of the high energy L-valley electrons scaled linearly with the droop observed in electroluminescence. The observed linearity indicates that droop observed in the LED and the L-valley population from Auger recombination is of the same origin.

## References

- [1] O. E. Tereshchenko, G. E. Shaibler, A. S. Yaroshevich, S. V Shevelev, A. S. Terekhov, V. V. Lundin, E. E. Zavarin, and A. I. Besyul'kin, "Low-Temperature Method of Cleaning p -GaN ( 0001 ) Surfaces for Photoemitters with Effective Negative Electron Affinity," *Phys. Solid State*, vol. 46, no. 10, pp. 1949–1953, 2004.
- [2] H.-J. Drouhin and M. Eminyan, "Simple concepts in the measurement of the energy distribution and spin polarization of an electron beam," *Rev. Sci. Instrum.*, vol. 57, no. 6, pp. 1052–1060, 1986.

## Chapter 2: Electroemission from InGaN LEDs

- [3] M. Piccardo, J. Iveland, L. Martinelli, S. Nakamura, J. W. Choi, J. S. Speck, C. Weisbuch, and J. Peretti, “Low-energy electro- and photo-emission spectroscopy of GaN materials and devices,” *J. Appl. Phys.*, vol. 117, no. 11, p. 112814, 2015.
- [4] W. E. Spicer, G. Vergara, and M. Carlo, “Calculated electron energy distribution of negative electron affinity cathodes,” vol. 436, pp. 83–90, 1999.
- [5] Z. Liu, F. Machuca, P. Pianetta, W. E. Spicer, and R. F. W. Pease, “Electron scattering study within the depletion region of the GaN 0001 and the GaAs (100) surface,” *Appl. Phys. Lett.*, vol. 85, no. 9, pp. 1541–1543, 2004.
- [6] A. A. Pakhnevich, V. V. Bakin, G. É. Shaïbler, and A. S. Terekhov, “Emission of ballistic photoelectrons from p-GaN(Cs,O) with the effective negative electron affinity,” *Phys. Solid State*, vol. 49, no. 11, pp. 2070–2075, Nov. 2007.
- [7] B. Monemar, “Fundamental energy gap of GaN from photoluminescence excitation spectra,” *Phys. Rev. B*, vol. 10, no. 2, pp. 676–681, 1974.
- [8] R. C. Eden, J. L. Moll, and W. E. Spicer, “Experimental Evidence For Optical Population of the X Minima in GaAs,” *Phys. Rev. Lett.*, vol. 18, no. 15, pp. 597–599, 1967.
- [9] J. Peretti, H.-J. Drouhin, D. Paget, and A. Mircea, “Band structure on indium phosphide from near-band-gap photoemission,” *Phys. Rev. B*, vol. 44, no. 15, 1991.
- [10] Y. Lassailly, P. Chiaradia, C. Hermann, and G. Lampel, “Experimental Photoemission Results on the low-energy Conduction Bands of Silicon,” *Phys. Rev. B*, vol. 41, no. 2, pp. 1266–1269, 1990.
- [11] R. Collazo, R. Schlessler, a. Roskowski, P. Miraglia, R. F. Davis, and Z. Sitar, “Electron energy distribution during high-field transport in AlN,” *J. Appl. Phys.*, vol. 93, no. 5, p. 2765, 2003.
- [12] C. J. Stanton and D. W. Bailey, “Rate equations for the study of femtosecond intervalley scattering in compound semiconductors,” *Phys. Rev. B*, vol. 45, no. 15, pp. 8369–8377, 1992.
- [13] S. Wu, P. Geiser, J. Jun, J. Karpinski, D. Wang, and R. Sobolewski, “Time-resolved intervalley transitions in GaN single crystals,” *J. Appl. Phys.*, vol. 101, no. 4, p. 043701, 2007.

## Chapter 2: Electroemission from InGaN LEDs

- [14] M. Piccardo, L. Martinelli, J. Iveland, N. Young, S. P. DenBaars, S. Nakamura, J. S. Speck, C. Weisbuch, and J. Peretti, "Determination of the first satellite valley energy in the conduction band of wurtzite GaN by near-band-gap photoemission spectroscopy," *Phys. Rev. B*, vol. 89, no. 23, p. 235124, Jun. 2014.
- [15] H. Ye, G. W. Wicks, and P. M. Fauchet, "Hot electron relaxation time in GaN," *Appl. Phys. Lett.*, vol. 74, no. 5, p. 711, 1999.
- [16] K. Wang, J. Simon, N. Goel, and D. Jena, "Optical study of hot electron transport in GaN: Signatures of the hot-phonon effect," *Appl. Phys. Lett.*, vol. 88, no. 2, p. 022103, 2006.
- [17] D. J. Suntrup III, G. Gupta, H. Li, S. Keller, and U. K. Mishra, "Measurement of the hot electron mean free path and the momentum relaxation rate in GaN," *Appl. Phys. Lett.*, vol. 105, no. July 2015, p. 263506, 2014.
- [18] M. Piccardo, "Electron Transport in GaN Light-Emitting Diodes," Ecole Polytechnique, 2013.
- [19] W. B. Joyce, "Steady-State Junction-Current Distributions in Thin Resistive Films on Semiconductor Junctions (Solutions of  $\nabla^2 v = \pm ev$ )," *J. Appl. Phys.*, vol. 41, no. 9, p. 3818, 1970.
- [20] W. E. Spicer and A. Herrera-gómez, "Modern Theory and Applications of Photocathodes," *SPIE*, 1993.
- [21] S. Luryi, "Hot electrons in semiconductor devices," in *Hot electrons in Semiconductors Physics and Devices*, N. Balkan, Ed. 1998, pp. 384 – 427.

## Chapter 3: Electroemission Control Experiments

*In this section I discuss a set of control experiments. First, selective detection of photoemission is measured from an LED under modulated light, demonstrating the low energy peak is photo-generated. Next, a simple GaN pn junction is measured, generating only a single  $\Gamma$ -valley peak. Complementary photoemission measurements are discussed, showing the presence of a low lying satellite conduction band valley at  $\sim 1$  eV, consistent with LED electroemission experiments.*

### 3.1 Introduction and Background

In the study described in the previous chapter [1] we performed electron energy analysis of electrons emitted into vacuum from a forward biased InGaN Light Emitting Diode (LED) that had been brought into negative electron affinity by cesiation of the p-surface. Three peaks were observed in the energy spectrum of vacuum emitted electrons. In this chapter, the identification of the origin of these three peaks is strengthened with a set of control experiments. The two higher energy peaks correspond to accumulation of electrons transported to the surface in the bulk  $\Gamma$  and side L conduction band valleys. These L-valley electrons provide a direct signature of hot Auger electrons. The third low energy peak results from surface photoemission induced from the internal LED light that is emitted from the InGaN quantum wells.

## Chapter 3: Electroemission Control Experiments

In this study two control experiments were performed. In the first control experiment, we measure a simple GaN *pn* homojunction containing no quantum wells or electron blocking layers. This *pn* junction generated a single peak in electroemission, with energy corresponding to electron accumulation in the  $\Gamma$ -valley. In the second control study, selective detection of the photoemission from an LED under modulated light excitation and DC electrical injection was performed. Under selective detection, only a single low energy peak was observed, the energy of this low energy peak corresponded to the energy of exciting light.

### 3.2 LED Sample & Device Structure

Two sets of samples were used for the control study an InGaN/GaN LED and a GaN *pn* junction. The LED sample in this control study was grown by Seoul VioSys using metal organic chemical vapor deposition (MOCVD). The sample was grown on single side polished on (0001) sapphire. The LED sample consisted of a  $p^{++}$  GaN cap/p-GaN (100nm,  $[Mg]=2 \times 10^{20} \text{ cm}^{-3}$ ) /  $\text{In}_{0.18}\text{Ga}_{0.82}\text{N}/\text{GaN}$  (5X QW/barrier region, approximately 25 nm total thickness)/InGaN region (150 nm)/Si doped n-type region ( $[Si]=1 \times 10^{19} \text{ cm}^{-3}$ ). Secondary ion mass spectroscopy (SIMS) measurements were performed on the LED sample to establish doping concentrations and the thickness of the doped regions. [Appendix B]

The simple GaN *pn* homo-junction structure was grown at UC Santa Barbara by MOCVD. The *pn* junction sample consisted of a  $p^{++}$  GaN cap/ $p^-$  GaN(200 nm,  $[Mg]=2 \times 10^{19} \text{ cm}^{-3}$ ) / unintentionally doped (UID) GaN (120 nm,  $1 \times 10^{16} \text{ cm}^{-3}$  [donors]) / n-GaN (200 nm,  $[Si]=5 \times 10^{17} \text{ cm}^{-3}$ )/ n-GaN (2  $\mu\text{m}$ ,  $[Si]=5 \times 10^{18} \text{ cm}^{-3}$ ) / GaN buffer.

## Chapter 3: Electroemission Control Experiments

Measurements performed on the *pn* junction and LED utilized a “concentric” contact design that differed from the “lateral” contact design described in the previous chapter. [1] More details on contact design, geometry and fabrication are found in Appendix B. The devices were fabricated using a mesa structure design that involved etching through the active region to the n-GaN region. The dry mesa etch was performed using an inductively coupled plasma (ICP) etching tool described in Appendix B. The n-contact consisted of a Ti/Al/Ni/Au metal stack in the shape of an annulus with inner and outer radii of 3 and 4.5 mm, respectively. The p-contact consisted of two parts: an isolated contact, and an injection area. The injection area was defined by a 500  $\mu\text{m}$  diameter circular Pd/Au contact with an evenly spaced array of 632 10  $\mu\text{m}$  holes that exposed the p-GaN surface. Both the n-contact and p-contact were deposited using electron beam evaporation described in Appendix B.

### **3.3 Sample Preparation for NEA**

After fabrication the devices were cleaned with acetone, isopropanol and deionized (DI) water. The samples were then cleaned using a solution of Piranha (3:1  $\text{H}_2\text{SO}_4:\text{H}_2\text{O}_2$ ) and rinsed with DI water. The samples were then introduced into a nitrogen purged glove box and cleaned with a solution of HCL:ISO described in more detail elsewhere.[Appendix B],[2]

### 3.4 Experimental Setup for Lock-in Detection

Lock-in measurements were performed to better understand the role of diode light in the electroemission process. In the lock-in experiment, a 458 nm Krypton/Argon laser was modulated with a chopper wheel at 50% duty cycle at 50 Hz. The laser was focused onto the aperture emission area of the p-contact during the measurement. By shining the laser onto the exposed p-GaN emission area, we can simulate the light conditions present under forward diode bias. The lock-in amplifier measured the Faraday current that passed through the analyzer in phase with the laser pulse. By measuring in phase with the laser pulse, we can isolate the light generated electrons in the electron energy distribution. The electrons generated by electroemission under forward diode bias are not modulated. These electrons are absent in the output of the lock-in, leaving just the light generated electrons signal. Energy distribution curves were measured at zero bias and forward bias under laser excitation.

The laser wavelength was selected to be close to the electroluminescence emission wavelength of the LED. The diode light power density under forward bias was similar to the incident laser power density. In forward bias, the diode generated light power density was estimated around  $100 \text{ W/cm}^2$ . This estimate is at 128 mA diode current and with a current density of  $90 \text{ A/cm}^2$ , assuming 50% EQE with a forward bias of 3V. The peak optical power of the laser was estimated to be  $\sim 100 \text{ W/cm}^2$  with a measured spot size of  $0.016 \text{ mm}^2$  and laser power of 18.1 mW. A diagram of the experiment is shown in **Fig. 3.1**.

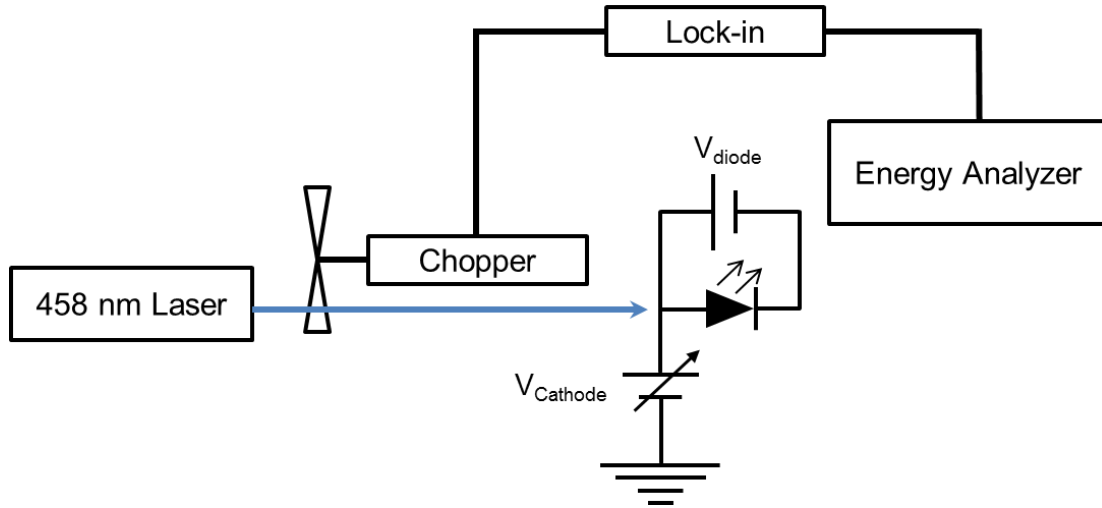


*Fig. 3.1 Schematic showing the configuration of in-phase detection of laser pulse. A 458 nm laser is sent through a chopper wheel. The lock-in amplifier selects the Faraday current that corresponds to the on pulse of the laser.*

### 3.5 Measured EDCs

Forward biased electroemission (EE) measurements were carried out on the *pn* junction and LED sample, EDCs are shown in **Fig. 3.2** and **Fig. 3.3** respectively. In the LED structure, three peaks were observed, consistent with what was measured in the previous studies.[1] A low energy peak below  $\Gamma$  in the bulk, a mid-energy peak corresponding to  $\Gamma$  and a high energy peak corresponding to accumulation in the L-valley. In the *pn* junction sample, only a single peak was observed, corresponding to accumulation in  $\Gamma$ .

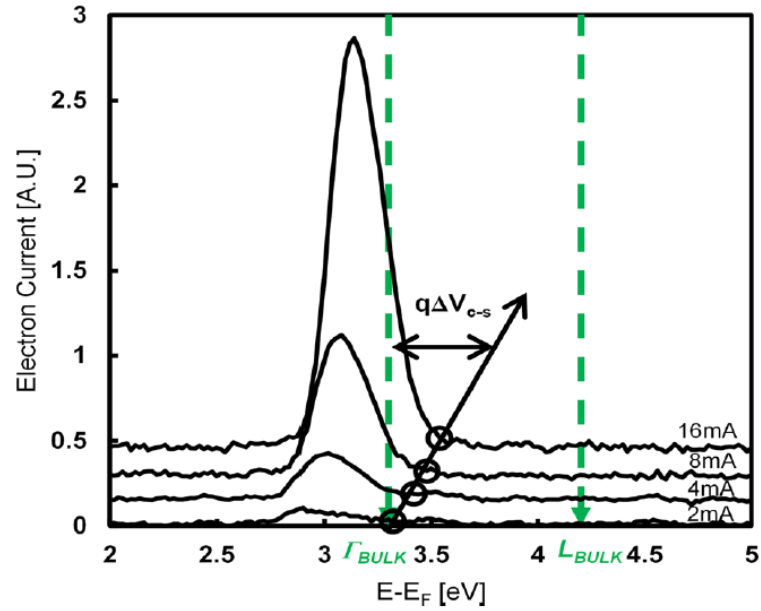


**Fig. 3.2** Electroemission spectra from the GaN pn junction sample. Electron current, measured at the Faraday cup, is plotted as a function of electron kinetic energy referenced to the bulk p-GaN ( $E_{Fp}$ ). Curves shifted up in electron current for visual aid. Electroemission measured under forward diode bias at 2 mA, 4 mA, 8 mA, and 16 mA diode current with circles indicating the high energy threshold. Green dashed arrows indicate L and  $\Gamma$ -valley bulk p-GaN positions. At low forward diode bias, voltage drop in the contact ( $\Delta V_{c-s}$ ) is small and the high energy threshold of the EDC corresponds to the bottom of the conduction band in the bulk 3.3 eV above  $E_{Fp}$ .

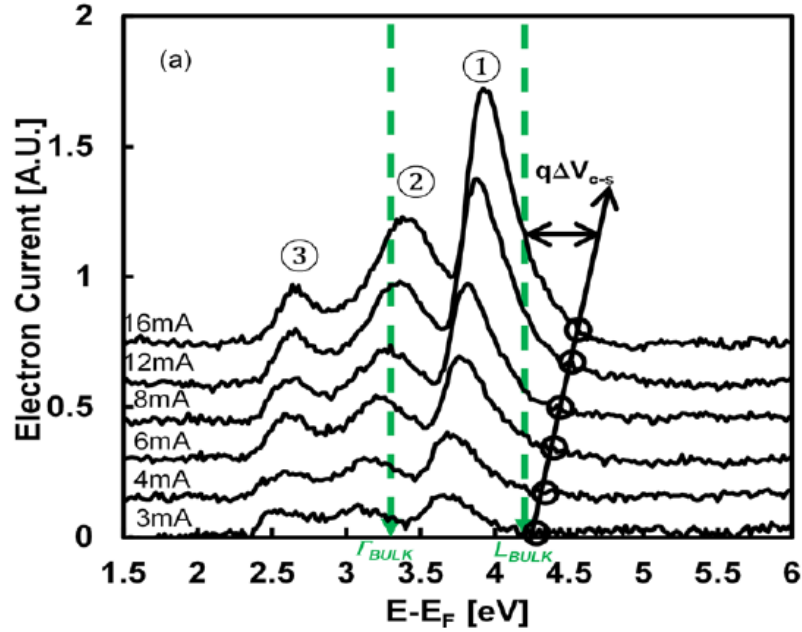


*Fig. 3.3 Electroemission spectrum from the LED sample. Electron current plotted as a function of electron energy referenced to the bulk p-GaN  $E_{Fp}$ . EE measured under forward bias at 3 mA, 4 mA, 6 mA, 8 mA, 12 mA, and 16mA diode current. Curves shifted up in electron current for visual aid. Green dashed arrows indicate L and  $\Gamma$ -valley bulk positions. Circles indicate the high energy threshold. At low forward diode bias, drop in the contact ( $\Delta V_{c-s}$ ) is small and the high energy threshold of the high energy peak (①) corresponds to the bottom of the L-valley in the bulk 4.2 eV above  $E_{Fp}$ . The high energy threshold of the mid-energy peak (②) corresponds to the bottom of the bulk C valley (around 3.3 eV).*

The LED and *pn* junction sample showed a spectral shift with increasing diode bias. In the LED, only the two high energy peaks showed a shift. The spectral shift was due to a voltage

drop between the p-contact and the p-GaN surface. This effect was described in more detail in the previous chapter.

Forward biased concurrent Electroemission and photoemission (EE+PE) and un-biased photoemission (PE) lock-in measurements were performed on the LED sample. At energies corresponding the the L and  $\Gamma$ -valley bulk positions, there was no signal observed above the noise floor EDC spectra from lock-in measurements are shown in **Fig. 3.4**.

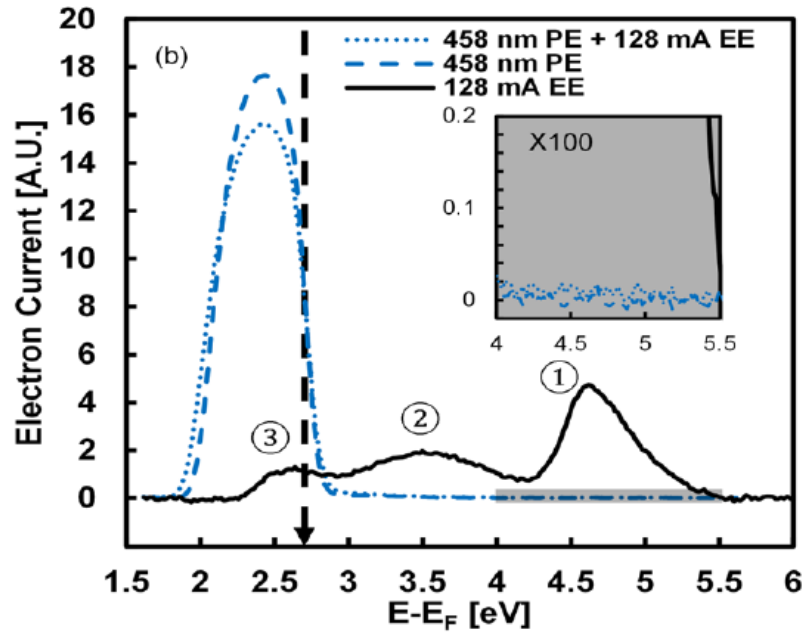


**Fig. 3.4** PE and EE spectra of the LED. Electron current plotted as a function of electron energy referenced to the bulk p-GaN  $E_{Fp}$ . PE is measured with lock-in in phase with the modulated 458nm PE exciting beam, with forward bias electrical injection (“458 nm PE 128mA EE” blue dotted curve) or without electrical injection (“458nm PE” blue dashed curve). Black dashed arrow indicating 2.71 eV corresponds to the 458 nm PE excitation energy. Inset of the noise floor

## Chapter 3: Electroemission Control Experiments

*highlighted in grey for the “458 nm PE + 128mA EE” and “458 nm PE” curves in the high energy regime, no observed signal generated by the 458 nm excitation source.*

### 3.6 Measured Lock-in EDCs

Selective lock-in measurements were performed on the LED sample to further understand the origin of the low energy peak ③. In lock-in measurements performed under bias (PE+EE) and under zero bias (PE) only a single peak was observed as shown in **Fig. 3.4**. The low energy peak ③ observed in all spectra has a high energy threshold that corresponds to the excitation energy of light as when optically exciting directly from the Fermi level, the highest energy an electron can have is given by the energy of the light. This is the same trend observed in metals when exciting from the Fermi level.

The observed low energy electrons likely originate from the exposed p-contact. In the LED sample, a SiO<sub>2</sub> layer covered most of the exposed p-contact metal. This SiO<sub>2</sub> coverage is likely responsible for the reduction of the relative intensity of peak ③ to what was measured of earlier samples which the p-GaN metal was not covered with a dielectric. Samples measured without a contact dielectric coating had larger low energy peak relative to the two higher energy peaks. [1] There is some fraction of low energy electrons, however, that can originate from the p-GaN. These electrons can come from gap states within the BBR where the Fermi level is closer to mid-gap. Electrons can also originate from occupied surface states on the p-GaN/cesium surface. Lastly, in the BBR region there is a large electric field, there electrons can directly excited by the reduced gap from the Franz-Keldysh.

### 3.7 Measurement of the *pn* Junction

In the *pn* junction sample only a single peak was observed. In a *pn* junction most of the injected current is leakage from n-GaN to p-GaN. The *pn* junction has no regions to confine carriers to achieve the high carrier concentrations necessary to generate Auger electrons and the L-valley peak. Furthermore, the *pn* junction had insufficient internal blue electroluminescence to necessary to photo-excite electrons and generate a low energy peak ③. The high energy threshold of the mid-energy peak is at roughly 3.3 eV, or about 3.4 eV from the valence band maximum. The separation of the bulk Fermi level to the valence band maximum is estimated at ~100 meV. The observed room temperature band gap of GaN is consistent with what is reported by photoluminescence measurements.[3]

### 3.8 Independent Measurements of the L-valley

Electronic structure calculations place the nearest side conduction band “L”-valley at energies around 2 to 2.25 eV above  $\Gamma$ . [4]–[6] Experimental values extend over a large range from ~300 meV [7], [8] to 1.34 eV [9]. More recently, reflective IR pump/probe measurements performed by Wu *et al.* observed an L-valley onset corresponding to photoexcitation energy of 4.51 eV. [10] An onset at 4.51 eV corresponds to a  $\Gamma$ -L spacing of

### Chapter 3: Electroemission Control Experiments

$\sim 0.85$  eV if calculated using a parabolic approximation. The  $\Gamma$ -L spacing observed by Wu *et al.* is close to what was measured in this current and previous electroemission study, around 0.95eV.[1], [11]

The  $\Gamma$ -L spacing has recently been measured directly using photoemission spectroscopy by Piccardo *et al.* [12] These measurements were carried out on the same energy analyzer as the previously described electroemission studies.[1], [11] In this photoemission study a p-type GaN sample was brought into NEA by cesiation. Electrons were excited from the valence band into the conduction band and the observed vacuum emitted electron energy was measured as a function of excitation wavelength. **Fig. 3.5** shows an example of photo-excitation.

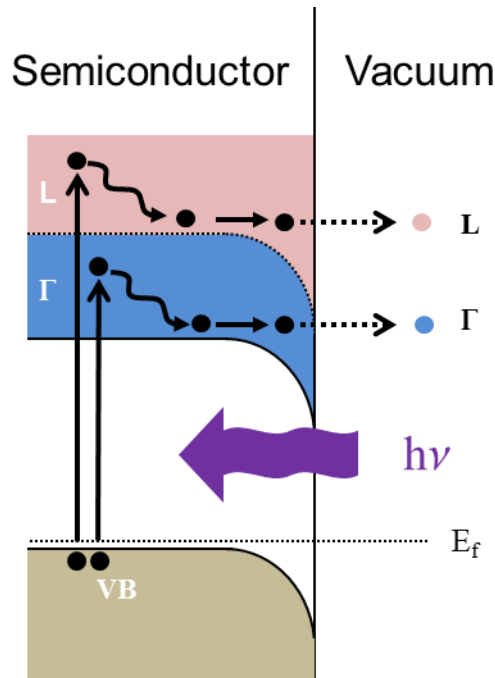


**Fig. 3.5** Principle of photoemission measurement: photo-excited electrons from the valence band are excited into the L and  $\Gamma$  conduction bands. After excitation, electrons thermalize to the bottom of

### Chapter 3: Electroemission Control Experiments

*the band and escape. The thermalize electron population is independent of excitation energy, and are fixed in the energy distribution.*

In the photoemission study, the  $\Gamma$ -L spacing was determined by two different methods. The first method determined  $\Gamma$ -L spacing by looking at features of the EDC that are invariant with excitation energy. These invariant features in the EDC correspond to positions the L and  $\Gamma$  conduction bands. The position of the bands is constant so the  $\Gamma$ -L separation can be determined by measuring the energy separation of these invariant structures. Using this method a  $\Gamma$ -L separation of  $0.90 \pm 0.08$  eV was obtained.

A second method was used to determine the  $\Gamma$ -L spacing by observing the onset of L-valley electrons in the measured spectra. This method does not rely on the energy scale of the analyzer. The analyzer is used only to determine when the onset of the L-valley occurs. The onset determination is only dependent only on knowledge of the excitation energy at which the L-valley is first present in the measured spectra. The onset of the L-valley was observed corresponding to an excitation energy of  $h\nu=4.63$  eV. Knowing the excitation onset the  $\Gamma$ -L separation is calculated as  $0.88 \pm 0.13$  eV was obtained. The calculation takes into account the dispersion of the valence band and conduction band for the direct transitions, an in addition, the energy of the phonon needed to scatter from  $\Gamma$  to L.

The photoemission study by Piccardo *et al.* provides strong confirmation of the measured  $\Gamma$ -L separation observed in the LED electroemission studies mentioned previously by us.[1], [11] This confirmation is highlighted by important differences between the photoemission and LED electroemission experiments. First, the photoemission study was performed without any

### Chapter 3: Electroemission Control Experiments

diode bias, so no spurious electric field was present. The LED electroemission study does have a bias between the n-contact and p-contact. Second, the method of electron promotion into the conduction band of the p-GaN region is different. In photoemission electrons are promoted from the valence band directly into the conduction band by light. In the electroemission study electrical bias provides the energy needed for conduction band electrons in the n-region to reach the p-region, either by leakage or Auger. Lastly, the methods used in the photoemission study are well established. Photoemission studies performed on cesiated photocathodes provide an accurate determination of valley energy separation in many other material systems including, Si[13], InP [14] and GaAs [15].

## References

- [1] J. Iveland, L. Martinelli, J. Peretti, J. S. Speck, and C. Weisbuch, “Direct measurement of Auger electrons emitted from a semiconductor light-emitting diode under electrical injection: identification of the dominant mechanism for efficiency droop,” *Phys. Rev. Lett.*, vol. 110, no. 17, p. 177406, Apr. 2013.
- [2] O. E. Tereshchenko, G. E. Shaibler, A. S. Yaroshevich, S. V. Shevelev, A. S. Terekhov, V. V. Lundin, E. E. Zavarin, and A. I. Besyul’kin, “Low-Temperature Method of Cleaning p -GaN ( 0001 ) Surfaces for Photoemitters with Effective Negative Electron Affinity,” *Phys. Solid State*, vol. 46, no. 10, pp. 1949–1953, 2004.
- [3] B. Monemar, “Fundamental energy gap of GaN from photoluminescence excitation spectra,” *Phys. Rev. B*, vol. 10, no. 2, pp. 676–681, 1974.
- [4] M. Goano, E. Bellotti, E. Ghillino, G. Ghione, and K. F. Brennan, “Band structure nonlocal pseudopotential calculation of the III-nitride wurtzite phase materials system. Part I. Binary compounds GaN, AlN, and InN,” *J. Appl. Phys.*, vol. 88, no. 11, p. 6467, 2000.
- [5] L. C. de Carvalho, A. Schleife, and F. Bechstedt, “Influence of exchange and correlation on structural and electronic properties of AlN, GaN, and InN polytypes,” *Phys. Rev. B*, vol. 84, no. 19, pp. 1–13, 2011.
- [6] K. T. Delaney, P. Rinke, and C. G. Van De Walle, “Auger recombination rates in nitrides from first principles,” *Appl. Phys. Lett.*, vol. 94, no. 19, 2009.
- [7] E. G. Brazel, M. A. Chin, V. Narayanamurti, D. Kapolnek, E. J. Tarsa, and S. P. DenBaars, “Ballistic electron emission microscopy study of transport in GaN thin films,” *Appl. Phys. Lett.*, vol. 70, no. 3, p. 330, 1997.
- [8] N. Nepal, K. B. Nam, J. Li, M. L. Nakarmi, J. Y. Lin, and H. X. Jiang, “Higher lying conduction band in GaN and AlN probed by photoluminescence spectroscopy,” *Appl. Phys. Lett.*, vol. 88, no. 26, pp. 0–3, 2006.
- [9] C.-K. Sun, Y.-L. Huang, S. Keller, U. Mishra, and S. DenBaars, “Ultrafast electron dynamics study of GaN,” *Phys. Rev. B*, vol. 59, no. 21, pp. 13535–13538, Jun. 1999.
- [10] S. Wu, P. Geiser, J. Jun, J. Karpinski, D. Wang, and R. Sobolewski, “Time-resolved intervalley transitions in GaN single crystals,” *J. Appl. Phys.*, vol. 101, no. 4, p. 043701, 2007.

### Chapter 3: Electroemission Control Experiments

- [11] J. Iveland, M. Piccardo, L. Martinelli, J. Peretti, J. W. Choi, N. Young, S. Nakamura, J. S. Speck, and C. Weisbuch, “Origin of electrons emitted into vacuum from InGaN light emitting diodes,” *Appl. Phys. Lett.*, vol. 105, no. 5, p. 052103, Aug. 2014.
- [12] M. Piccardo, L. Martinelli, J. Iveland, N. Young, S. P. DenBaars, S. Nakamura, J. S. Speck, C. Weisbuch, and J. Peretti, “Determination of the first satellite valley energy in the conduction band of wurtzite GaN by near-band-gap photoemission spectroscopy,” *Phys. Rev. B*, vol. 89, no. 23, p. 235124, Jun. 2014.
- [13] Y. Lassailly, P. Chiaradia, C. Hermann, and G. Lampel, “Experimental Photoemission Results on the low-energy Conduction Bands of Silicon,” *Phys. Rev. B*, vol. 41, no. 2, pp. 1266–1269, 1990.
- [14] J. Peretti, H.-J. Drouhin, D. Paget, and A. Mircea, “Band structure on indium phosphide from near-band-gap photoemission,” *Phys. Rev. B*, vol. 44, no. 15, 1991.
- [15] H.-J. Drouhin, C. Hermann, and G. Lampel, “Photoemission from activated gallium arsenide. I. Very-high-resolution energy distribution curves,” *Phys. Rev. B*, vol. 31, no. 6, pp. 3859–3871, 1985.

## Chapter 4 Current and Future Work

*In this section we present an energy distribution curve measured on a new vacuum electron analyzer at UC Santa Barbara. In addition, improvements to electroemission device design are discussed. A set of experiments are proposed to get a better quantitative understanding of the transport of electrons measured in the LED electroemission experiments.*

### 4.1 Electroemission with UCSB Spherical Sector Analyzer

Energy distribution curves were measured independently on a spherical sector analyzer at UCSB, described further in appendix A. These measurements confirm the repeatability of the experiment and rule out any possibility that the three peaks observed in electroemission from an LED originate from analyzer effects.

A commercial LED sample with the same epitaxial structure and contact design as a previously described study [1] was measured. The sample was cleaned for NEA, introduced into vacuum and cesiated. The energy distribution curve is plotted in **Fig. 4.1**. Three peaks were observed in the energy distribution corresponding to an L,  $\Gamma$  and photoemission peak. The energy positions of the three peaks is consistent with what was measured in the previous electroemission studies.[1], [2]

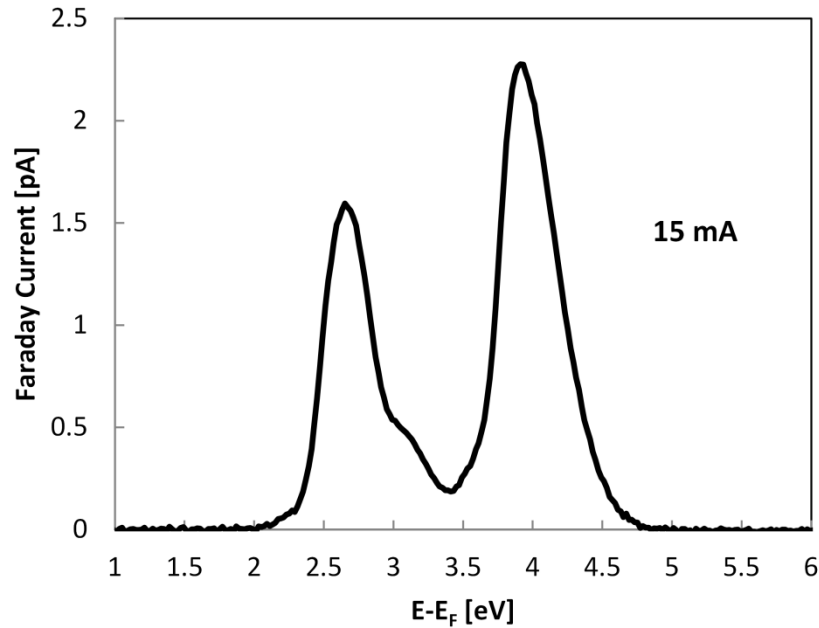


*Fig. 4.1 Faraday current plotted as a function of energy from the Fermi level. Diode operated at 15 mA in forward bias.*

The ratio of the three observed peaks in the energy distribution curved measured at UCSB is different from what was previously reported in chapter 3. [1] This change in peak ratio has many possible origins. First, the sample measured did not have a dielectric coating on the p-metal contact. Without a dielectric coating there will be an increased electron contribution from photoemission from the metal surface. Second, the amount of diode light hitting the exposed metal is different between the UCSB and PMC analyzers. The amount of diode light hitting the sample is dependent on how the light reflects off the sample holder and the analyzer entrance slit. The UCSB sample holder and analyzer entrance slit is different than that of PMC. The vacuum level of both the p-GaN surface and metal contact will change the intensity

## Chapter 4: Current and Future Work

of the low energy and mid-energy peaks. This vacuum level changes with cesiation conditions, which can vary between measurements. The UCSB and PMC analyzers have been independently calibrated for energy. The UCSB analyzer has not been calibrated for electron transmission as a function of energy. The transmission calibration can change the relative peak intensity and should be calibrated before quantitative measurements can be made.

### **4.2 Improvements to Electroemission Sample Design**

A high temperature anneal was performed to achieve a higher quantum efficiency cathode.[3] The n and p-contacts used in the current device design suffer from an increase in contact resistance after the cleaning anneal. The increased contact resistance is responsible for an increased diode voltage. As discussed in chapter 2, the voltage dropped in the p-contact is responsible for a shift in the measured electroemission spectra. It may be possible to improve the n-contact by using a pre-annealed Ti/Al/Ni/Au contact. The p-contact may be improved using a refractory metal with a high work function such as Pd.

A structure with smaller apertures and a higher fill fraction of exposed p-GaN to contact area can improve electron emission efficiency. Based on simulations, at 50 mA diode current only 15% of the total injected current is injected into the 10 $\mu$ m aperture array.[4] The injection efficiency can be greatly improved by reducing the aperture size, which improves the lateral current spreading. The exposed p-GaN fill fraction to p-contact metal is currently ~22%. The fill factor can be greatly increased by spacing the apertures closer together ideally using a

## Chapter 4: Current and Future Work

hexagonal aperture array. The improved fill fraction will not only increase signal, but it will also reduce the area of exposed metal resulting in a reduction of metal photoemission.

Photoemission from the exposed metal contacts is largely responsible for the spurious low energy peak observed in the energy distribution curves from LED electroemission. Light from the diode can excite electrons from the surface of the metal, either directly or by reflecting off the analyzer entrance slit. Metal contact photoemission is shown in **Fig. 4.2**. Further reduction of the low energy peak can be realized by covering the exposed metal with a dielectric, which does not photo-emit electrons by visible light. To facilitate the dielectric sticking to the metal contact surface a Ti layer (30 nm) can be used. Deposition of 100 nm of SiO<sub>2</sub> on the metal contact surface can eliminate the metal photoemission. Partial coverage of the p-GaN surface can also help determine what contribution p-GaN photoemission has to the low energy peak.

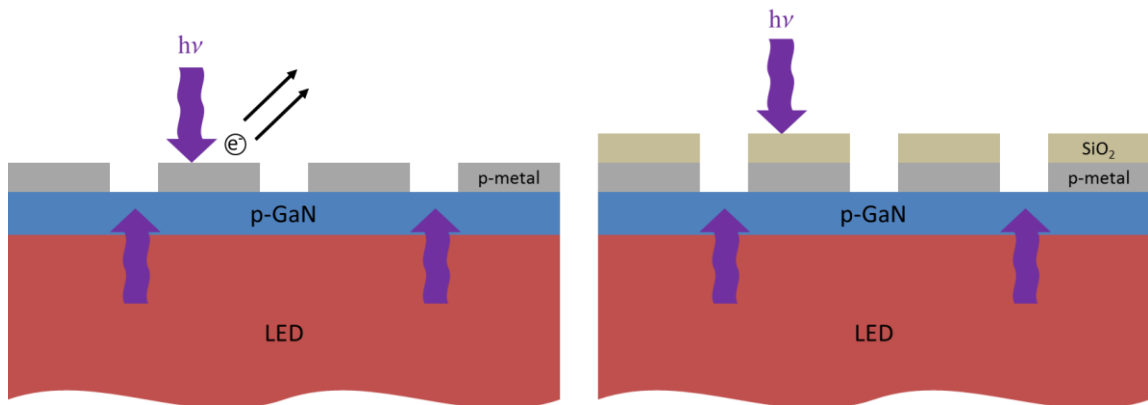


*Fig. 4.2 An electron excited by photoemission from diode light (left). To reduce photo-excited electrons, a SiO<sub>2</sub> layer can be used. (right)*

### 4.3 Proposed Future Experiments

The results described in previous studies [2], [1] are relative measurements relating diode light, electron current and diode current. To better understand the transport processes within an LED a more quantitative understanding of carrier dynamics must be obtained.

#### **Diffusion length and escape probability**

A *pn* homojunction series can be grown to better understand minority carrier diffusion length in p-type GaN as well as the electron escape probability. The minority carrier diffusion length varies in the literature, but is around 100 nm for p-type GaN with  $[Mg] \sim 10^{19} \text{ cm}^{-3}$ . [5] Diffusion length is dependent on a number of extrinsic factors such as doping and defect density. [6] After electrons diffuse to the surface as minority carriers in the p-GaN, they must then escape into vacuum. The probability they will escape when they reach the surface is given by their escape probability  $P(V_{\text{diode}})$ . Even if their energy is greater than the vacuum level electrons can undergo scattering in the band bending region, as well as reflection at the semiconductor/vacuum interface. The escape probability may be a function of diode current. With varying diode current the voltage drop between the p-contact and p-GaN will change, which can change the width and height of the band bending region.

A p-GaN thickness series should be measured to determine the diffusion length and escape probability. It is assumed that the diffusion length and escape probability is constant between

## Chapter 4: Current and Future Work

samples. Emitted electron current would be measured as a function of forward bias. For thicker p-GaN samples, a reduction in total cathode current should be observed, as shown schematically in **Fig. 4.3**. The uniformity of the cesiation between samples also needs to be held constant. Cesiumation uniformity can be measured by looking at the position and slope of energy distribution curves.

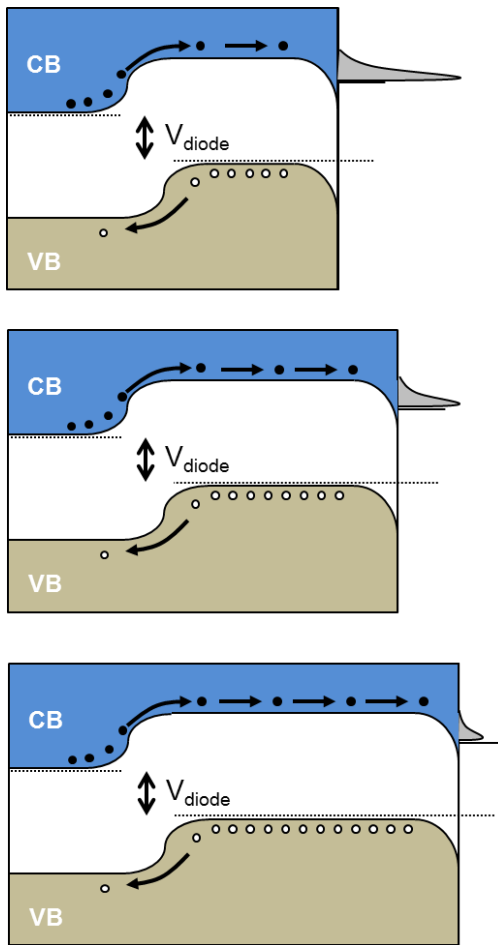


**Fig. 4.3** Figure showing a reduced electron emission current with increasing p-GaN length.

## Chapter 4: Current and Future Work

A *pn* junction series with varying surface doping should be measured to better understand the escape probability of electrons. The ratio of bulk p-GaN thickness to surface p-GaN thickness should be as large as possible to reduce any possible change in the diffusion length by varying surface p-doping. As surface doping is increased, the BBR width decreases, which is shown in **Fig. 4.4**. The width of the BBR is given by:

$$W_{BBR} = \sqrt{\frac{2\epsilon\phi_s}{qN_A}}$$

Where  $\phi_s$  is the height of the conduction band bending at the surface,  $N_A$  is the acceptor density,  $\epsilon$  is the dielectric constant, and  $q$  is electron charge. The band bending height,  $\phi_s$ , is governed by surface preparation and termination. Some see a change in barrier height upon cesiation and others do not.[7], [8] Furthermore, some report a change in Fermi pinning level and barrier height. This can happen by varying doping and depends on the type of doping: Si (n-type) or Mg (p-type).[9]

The change in BBR scattering should be observable by the width of the energy distribution where increasing barrier width should increase scattering. Models show that a spectral narrowing should be observed for higher doping levels.[10] In addition, increased BBR scattering should contribute to a decrease in total emitted electron current. Optimal doping is always a balance between diffusion length and BBR scattering effects.

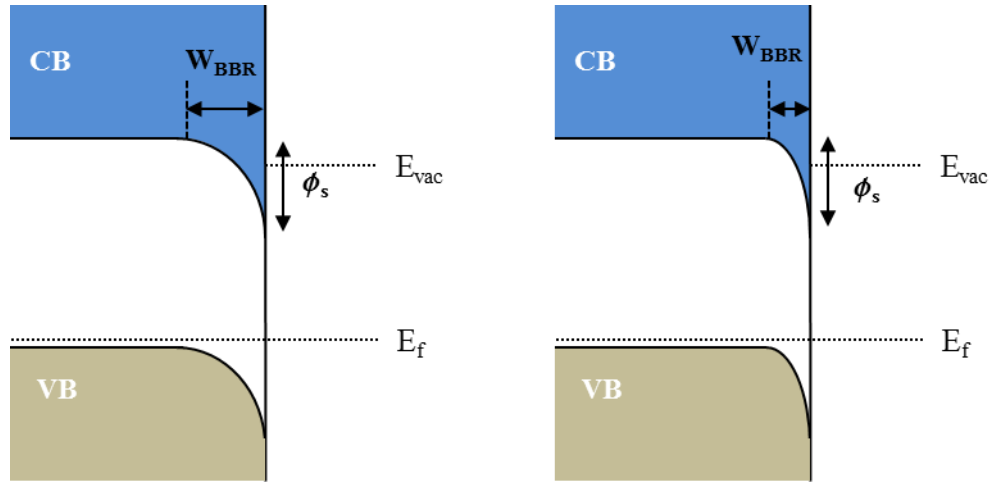


*Fig. 4.4* Figure showing the a large (left) and narrow (right) BBR width with low and high doping respectively.

### Electron Blocking Layer

Many commercial InGaN/GaN LEDs utilize an AlGaIn electron blocking layer (EBL). This prevents electrons from overshooting the active region and recombining in the p-GaN.[11] The design and effectiveness of the EBL needs to be investigated further as the exact physical role an EBL plays in LED is poorly understood. Some reports suggest that an EBL may hinder hole transport to the active region. [12] Other studies show an increase in EQE at high current densities in structures without an EBL. [13]

A *pn* junction can be used to investigate the AlGaIn EBL. Structures can be grown with and without the EBL, and total emitted electron current can be measured (shown in **Fig. 4.5**). A *pn* junction with an EBL is expected to have a lower total electron current than a *pn* junction without an EBL. The difference in electron current between structures can provide

## Chapter 4: Current and Future Work

information on the effectiveness of the EBL. Parameters such as EBL doping and aluminum composition should be varied. The effects of polarization can be investigated by measuring EBLs in semi-polar and non-polar growth directions. In addition, these measurements can be carried out at an elevated temperature to try and understand the leakage mechanism through or over the EBL.

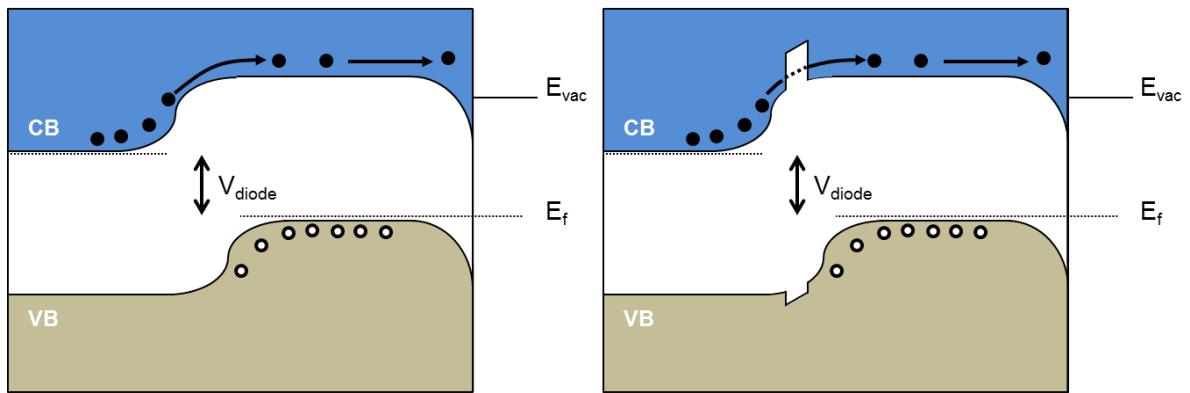


*Fig. 4.5* Figure showing a pn junction sample with (right) and without (left) an AlGaN EBL.

### **Roughness and Extraction**

In addition to the p-doping study described above, crystalline plane and the effects of surface roughness should be explored. As electrons leave the semiconductor, the component of their crystal momentum parallel to the plane of the surface is conserved.[14], [15] Total energy must also be conserved while the effective mass between the semiconductor and vacuum have changed. The emission angle can become imaginary and forbidden for electrons with large crystal momentum, which are those emitted from high  $\mathbf{k}$  side-valleys.

## Chapter 4: Current and Future Work

The escape of electrons emitted from a high  $\mathbf{k}$  side-valley can vary between planes as the direction of the side-valley relative to the surface normal changes. A change in escape probability has been observed with changing crystal orientation in GaAs. [16] The exact nature of how side-valley electrons are emitted, however, is still under debate. It is suggested that surface roughness can also change the normal vector to the surface and effect extraction. Roughness can give a smaller effective  $\mathbf{k}_{\parallel}$  vector than in the bulk. [17] To assess roughness effects, a sample series of varying roughness while keeping doping constant can be measured. For highly rough samples the observation of higher electron extraction may be observed resulting in an increase in electron current. In addition, the ratio of the L-valley peak, which originates at high  $\mathbf{k}$ , may increase relative to the  $\Gamma$ -valley.

### **LED Thickness Series**

To understand the back scattering rate between the L and  $\Gamma$ -valleys, an LED p-GaN thickness series can be grown. Electrons diffusing to the surface will have more time to back scatter to  $\Gamma$  with thicker p-GaN. An LED with a shorter p-GaN region should have a larger population of L-valley electrons relative to the  $\Gamma$ -valley electrons.

### **Droop and Transport: QW Width, Number, Composition, and Growth Direction**

A study should be performed that varies the number of *active* quantum wells (QWs). By changing the number of *active* quantum wells, the carrier concentration in each well can be reduced. The reduction of carrier concentration will increase the current density where the

## Chapter 4: Current and Future Work

peak EQE is reached. The electron energy distribution at different peak EQE values can be measured. Furthermore, it has been shown that in certain structures, preferential injection occurs in the p-side QWs.[18] A study can be done to try and assess uniform injection. By changing the number of quantum well carrier overflow can be assessed by looking at the overshoot electrons that end up in  $\Gamma$  (assuming transport is hole limited, not electron limited), whose population has different dependence on carrier concentration than Auger, which uniquely populates L. In addition, marker wells (of a different wavelength) in the p-GaN can be used to understand overshoot. By observing luminescence in marker wells, an assessment of diffusion length can also be obtained. To gain a quantitative understanding of electron transport, the efficiency of each marker well needs to be calibrated to quantify the population of electrons reaching the well.

The effects of QW indium composition on droop and transport can also be assessed. Is the cause of droop the same for violet and green LEDs? To answer this question and assess the effects of indium composition on droop, a series of LEDs with varying indium compositions can be measured. By looking at the population of L and  $\Gamma$  electrons, we can assess how many recombine as Auger electrons and how many contribute to leakage. The energy of the hot Auger electron is varied relative to the bulk  $\Gamma$  CBM by changing the quantum well band gap. Changing the QW band gap is done by varying the indium composition. By tuning the quantum well band gap, conduction band structures can be more precisely probed bringing side-valleys in and out of resonance with the hot Auger electrons.

## Chapter 4: Current and Future Work

Wurtzite GaN suffers from piezoelectric and spontaneous polarization, when grown in the c-plane direction. From polarization, bands are bent in the quantum wells separating the electron and hole wave functions and reducing the radiative efficiency.[19] Droop has been shown to be reduced when grown on semi-polar and non-polar planes by reducing or eliminating the effects of polarization. [20] The effects of polarization on droop and transport can be assessed by measuring LEDs grown on semipolar and non-polar planes. Electron energy distributions can be measured in “low droop planes” to determine what the dominate droop mechanism is without the effects of polarization.

## References

- [1] J. Iveland, M. Piccardo, L. Martinelli, J. Peretti, J. W. Choi, N. Young, S. Nakamura, J. S. Speck, and C. Weisbuch, “Origin of electrons emitted into vacuum from InGaN light emitting diodes,” *Appl. Phys. Lett.*, vol. 105, no. 5, p. 052103, Aug. 2014.
- [2] J. Iveland, L. Martinelli, J. Peretti, J. S. Speck, and C. Weisbuch, “Direct measurement of Auger electrons emitted from a semiconductor light-emitting diode under electrical injection: identification of the dominant mechanism for efficiency droop.,” *Phys. Rev. Lett.*, vol. 110, no. 17, p. 177406, Apr. 2013.
- [3] O. E. Tereshchenko, G. E. Shaibler, A. S. Yaroshevich, S. V. Shevelev, A. S. Terekhov, V. V. Lundin, E. E. Zavarin, and A. I. Besyul’kin, “Low-Temperature Method of Cleaning p -GaN ( 0001 ) Surfaces for Photoemitters with Effective Negative Electron Affinity,” *Phys. Solid State*, vol. 46, no. 10, pp. 1949–1953, 2004.

## Chapter 4: Current and Future Work

- [4] M. Piccardo, "Electron Transport in GaN Light-Emitting Diodes," Ecole Polytechnique, 2013.
- [5] S. Hafiz, S. Metzner, F. Zhang, M. Monavarian, V. Avrutin, H. Morkoç, C. Karbaum, F. Bertram, J. Christen, B. Gil, and Ü. Özgür, "Determination of carrier diffusion length in p- and n-type GaN," *SPIE Proc.*, vol. 8986, p. 89862C, Mar. 2014.
- [6] K. Kumakura, T. Makimoto, N. Kobayashi, T. Hashizume, T. Fukui, and H. Hasegawa, "Minority carrier diffusion length in GaN: Dislocation density and doping concentration dependence," *Appl. Phys. Lett.*, vol. 86, no. 5, pp. 1–3, 2005.
- [7] C. I. Wu and A. Kahn, "Electronic states and effective negative electron affinity at cesiated p-GaN surfaces," *J. Appl. Phys.*, vol. 86, no. 6, pp. 3209–3212, 1999.
- [8] A. A. Pakhnevich, V. V. Bakin, A. V. Yaz'kov, G. É. Shaibler, S. V. Shevelev, O. E. Tereshchenko, A. S. Yaroshevich, and A. S. Terekhov, "Energy Distributions of Photoelectrons Emitted from p-GaN (Cs, O) with Effective Negative Electron Affinity," *JETP Lett.*, vol. 79, no. 10, pp. 479–483, 2004.
- [9] M. Myckeler, W. Monch, T. U. Kampen, R. Dimitrov, O. Ambacher, and M. Stutzmann, "Negative electron affinity of cesiated p-GaN (0001)... surfaces," *J. Vac. Sci. Technol. B*, vol. 16, no. 4, pp. 2224–2228, 1998.
- [10] W. E. Spicer, G. Vergara, and M. Carlo, "Calculated electron energy distribution of negative electron affinity cathodes," vol. 436, pp. 83–90, 1999.
- [11] Y.-Y. Zhang and G.-R. Yao, "Performance enhancement of blue light-emitting diodes with AlGaInN barriers and a special designed electron-blocking layer," *J. Appl. Phys.*, vol. 110, no. 9, p. 093104, 2011.
- [12] I. V. Rozhansky and D. a. Zakheim, "Analysis of the causes of the decrease in the electroluminescence efficiency of AlGaInN light-emitting-diode heterostructures at high pumping density," *Semiconductors*, vol. 40, no. 7, pp. 839–845, Jul. 2006.
- [13] S.-H. Han, D.-Y. Lee, S.-J. Lee, C.-Y. Cho, M.-K. Kwon, S. P. Lee, D. Y. Noh, D.-J. Kim, Y. C. Kim, and S.-J. Park, "Effect of electron blocking layer on efficiency droop in InGaInN/GaN multiple quantum well light-emitting diodes," *Appl. Phys. Lett.*, vol. 94, no. 23, p. 231123, 2009.
- [14] R. L. Bell, *Negative Electron Affinity Devices*. London: Oxford University Press, 1973.
- [15] Z. Liu, Y. Sun, P. Pianetta, and R. F. W. Pease, "Narrow cone emission from negative electron affinity photocathodes," *J. Vac. Sci. Technol. B Microelectron. Nanom. Struct.*, vol. 23, no. 6, p. 2758, 2005.

## Chapter 4: Current and Future Work

- [16] L. W. James, G. a. Antypas, J. Edgecumbe, R. L. Moon, and R. L. Bell, “Dependence on crystalline face of the band bending in Cs<sub>2</sub> O-activated gaas,” *J. Appl. Phys.*, vol. 42, no. 12, pp. 4976–4980, 1971.
- [17] S. Karkare and I. Bazarov, “Effect of nanoscale surface roughness on transverse energy spread from GaAs photocathodes,” *Appl. Phys. Lett.*, vol. 98, no. 9, pp. 2009–2012, 2011.
- [18] A. David, M. J. Grundmann, J. F. Kaeding, N. F. Gardner, T. G. Mihopoulos, and M. R. Krames, “Carrier distribution in (0001)InGaN/GaN multiple quantum well light-emitting diodes,” *Appl. Phys. Lett.*, vol. 92, no. 5, p. 053502, 2008.
- [19] V. Fiorentini, F. Bernardini, F. Della Sala, a. Di Carlo, and P. Lugli, “Effects of macroscopic polarization in III-V nitride multi-quantum-wells,” vol. 60, no. 12, p. 11, 1999.
- [20] C.-C. Pan, S. Tanaka, F. Wu, Y. Zhao, J. S. Speck, S. Nakamura, S. P. DenBaars, and D. Feezell, “High-Power, Low-Efficiency-Droop Semipolar (20-2-1) Single-Quantum-Well Blue Light-Emitting Diodes,” *Appl. Phys. Express*, vol. 5, no. 6, p. 062103, Jun. 2012.

## **Appendix A: UCSB Electron Energy Analyzer**

*The design and operation of the spherical sector electron energy analyzer is discussed. The calibration procedure for energy and resolution is reviewed. Fabrication and operation challenges in measuring low energy electrons are presented as well.*

### **A1 Design and Operation Principles**

Energy distribution curves described in chapter 4 of this document were taken using a Comstock AC-901 electrostatic spherical sector energy analyzer. [1] Electron energies in the two previous studies [2], [3] were taken using a cylindrical analyzer described elsewhere.[4] Calibration procedure and operation of both the cylindrical and spherical sector analyzers are identical, varying only in the calibrated work function values. The spherical sector analyzer consists of two concentric spherical sectors, entrance and exit slits, top and bottom plate, an Einzel lens and a Faraday cup. Each of the five potentials set under operation are shown in **Fig. A1**.

## Appendix A: UCSB Electron Energy Analyzer

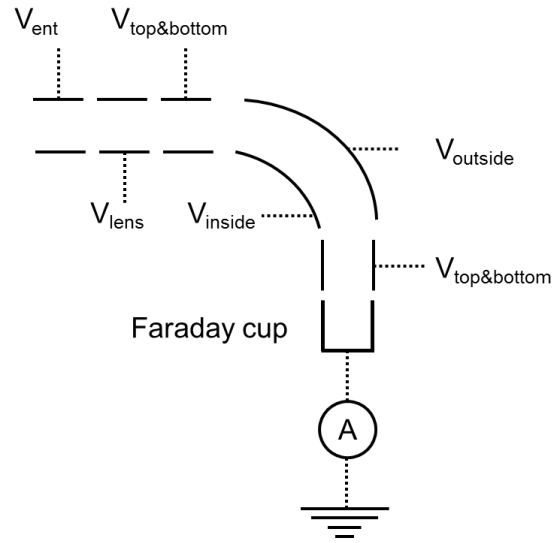


**Fig. A1** Figure showing the potentials that are set on the analyzer plates. No potential is set on the Faraday cup. A current amplifier is placed in series with the Faraday cup and ground.

All five of the analyzer plate potentials are set using a Kepco current/voltage supply. Each voltage is set using a potentiometer acting as a voltage divider; all voltages are set in parallel. In addition, each voltage is referenced positive with respect to earth ground, therefore the earth ground acts as a common Fermi level. Each potential can be broken in series to allow an ammeter measurement of the electron current at each analyzer plate. Each set potential is delivered to the analyzer through a multi pin UHV feedthrough, all atmospheric wiring is coaxial. Faraday cup current is measured using a Femto DLPCA-200 variable gain current amplifier. The wiring diagram of the analyzer is shown in **Fig. A2**.

## Appendix A: UCSB Electron Energy Analyzer

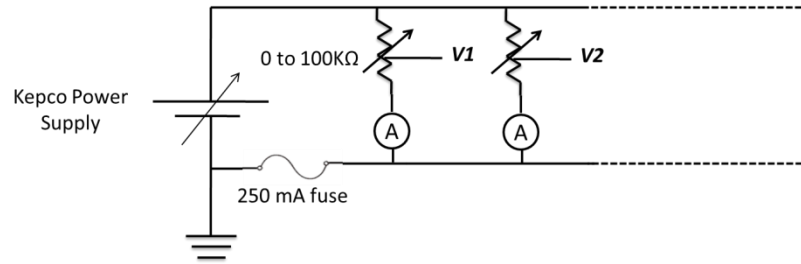


**Fig. A2** Wiring diagram for the voltage box controlling the analyzer plate potentials.

The analyzer is operated at a pass energy that is defined by geometry of the selector plates and the difference in potential set on the selector plates. The transmission energy given as a function of selector plate radii  $r_1$  and  $r_2$  plate radius and potential difference  $\Delta V$  is given by[5]:

$$TE = \frac{\Delta V}{\frac{r_2}{r_1} - \frac{r_1}{r_2}}$$

For the model AC-901,  $r_1 = 32.5$  mm and  $r_2 = 40.5$  mm giving:

$$TE = 2.27\Delta V$$

The energy resolution of the analyzer is given as a fraction of the distribution full width half max to the transmission energy.

$$\frac{\Delta E}{TE}$$

For a spherical sector this resolution is estimated by[3]:

## Appendix A: UCSB Electron Energy Analyzer

$$\frac{\Delta E}{TE} = \frac{W}{R(1 - \cos[\phi]) + L\sin[\phi]}$$

Here  $W$  is the entrance and exit slit diameter,  $\phi$  is the angle subtended by the spherical sector at a point in the center of the analyzer, for the AC-901 this angle is  $160^\circ$ . The value  $R$  is the mean radius between sectors to the center of the assembly. Lastly,  $L$  is the distance from exit sector to the center of the slit assembly. Above values are shown schematically in references.[1], [5] For the installed 1 mm diameter entrance and exit slit, this resolution is around 0.8%.

### **A2 Fixed Transmission Energy Mode Operation**

For all experiments mentioned in this document, the analyzer is operated in “Fixed Transmission Energy” mode. In this configuration, the analyzer transmission energy is held constant throughout the energy scan. Keeping the transmission energy constant also results in a fixed analyzer energy resolution. To achieve this, all analyzer potentials are set at a fixed value and the sample potential ( $V_{\text{cathode}}$ ) relative to ground is increased and decreased. This configuration accelerates and de-accelerates electrons into the analyzer to fall within the pass energy (described below). The fixed transmission configuration is shown schematically in **Fig. A3**.

## Appendix A: UCSB Electron Energy Analyzer

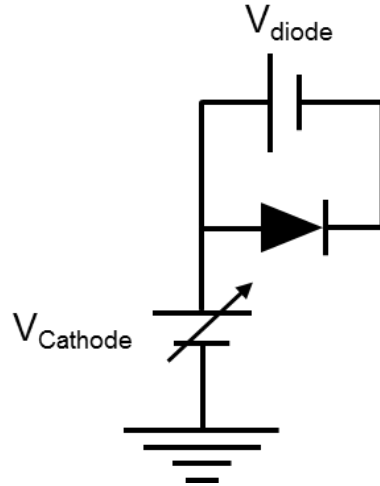


*Fig. A3 Figure showing how the diode potential and cathode potential are applied when operating in constant transmission mode.*

### **A3 Fixed Field Mode Operation**

Another configuration the analyzer could be operated in is “Fixed Field Mode”. In a fixed field mode configuration, all potentials are held constant aside from the inside and outside selector plates. The potential between these plates are varied, keeping the average constant, to vary the pass energy. In this configuration, all electric fields remain constant; however the resolution changes during the scan, as the transmission energy is changing. The selector voltage is varied symmetrically between a fixed value set by the top and bottom potential. Two resistors are used as a voltage divider. The resistor values should be appropriate for the given pass energy to avoid too much current passing through the two resistors. The resistors should be high accuracy (<1%) to assure that the potential is being set symmetrically. As shown in **Fig. A4**, the selector potential must be applied using a floating power supply, to

## Appendix A: UCSB Electron Energy Analyzer

assure that the voltage is referenced to the rest of the analyzer potentials and not ground. A Keithley 2400 can be used to set this  $V_{\text{Selector}}$  voltage.

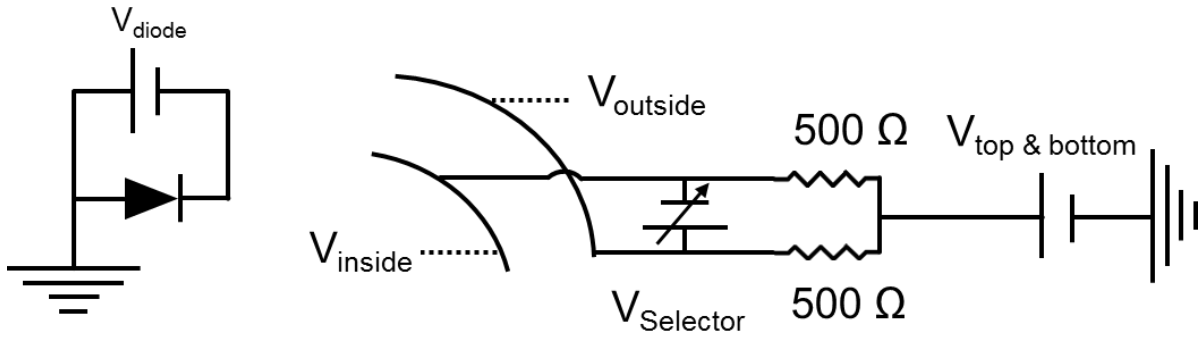


*Fig. A4 Figure showing the wiring diagram for Fixed Field Mode operation. All potentials remain constant except for the selector potential.*

### A4 Electrostatic Einzel Lens

The analyzer contains a three element cylindrical Einzel lens. An Einzel can increase the transmission of the analyzer with the expense of angular resolution. Typical improvements of around 10X improved transmission are seen using such a lens. With an increase in angular acceptance from 0.002 steradians to 0.008 steradians using the 1 mm entrance slit. The three element Einzel lens is operated without changing electron energy. This is achieved by fixing the inside and outside potentials and varying the center potential to focus the lens. The inside and outside potentials ( $V_{\text{ent}}$  and  $V_{\text{top\&bottom}}$ ) are fixed at potential  $V_0$ , where the inside potential lens potential is  $V_i$  ( $V_{\text{lens}}$ ). Numerical calculations for focal length verses lens potential ratio ( $V_i/V_0$ ) are shown in **Fig. A5**.<sup>[6]</sup> In this calculation the focal length is given in inches, and the outside surface of the exit slit sits at a focal length of 0.73 in. Focal length is measured from

Appendix A: UCSB Electron Energy Analyzer

the center of the inside lens. During measurement the surface of the sample is at a focal length approximately 0.75 in to 0.80 in.

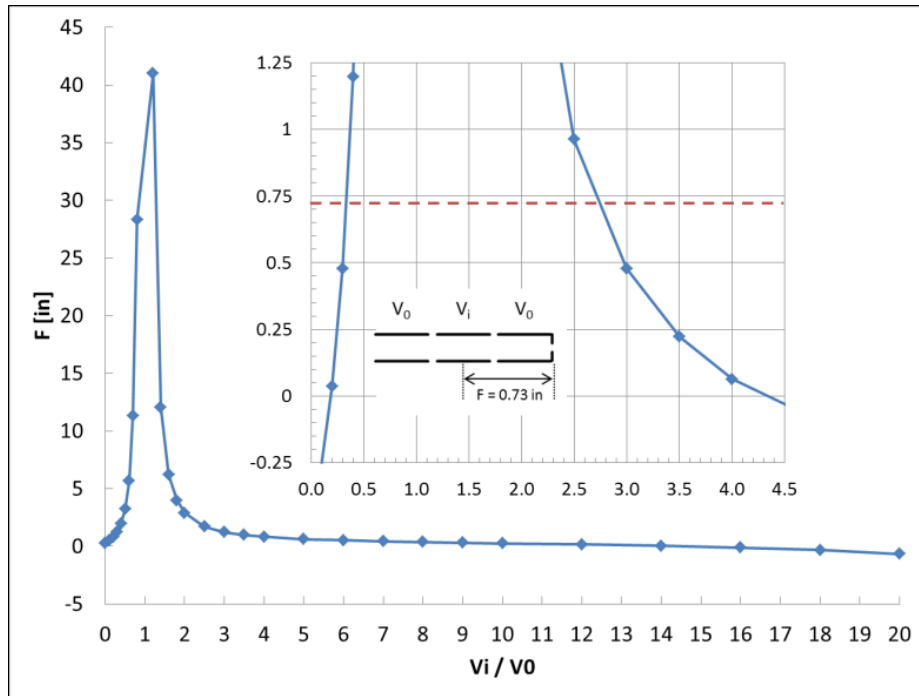


**Fig. A5** Showing the calculated focal length as a function of inside and outside lens potentials ( $V_i$  and  $V_0$  respectively).

The measured value of the optimal lens ratio ( $V_i/V_0$ ) was found to change with transmission energy. Here, We are fixing the transmission energy equal to the outside lens potential  $TE = V_0$ . In practice, the lens potential is found by maximizing the faraday current at a given sample distance and transmission energy.

## Appendix A: UCSB Electron Energy Analyzer

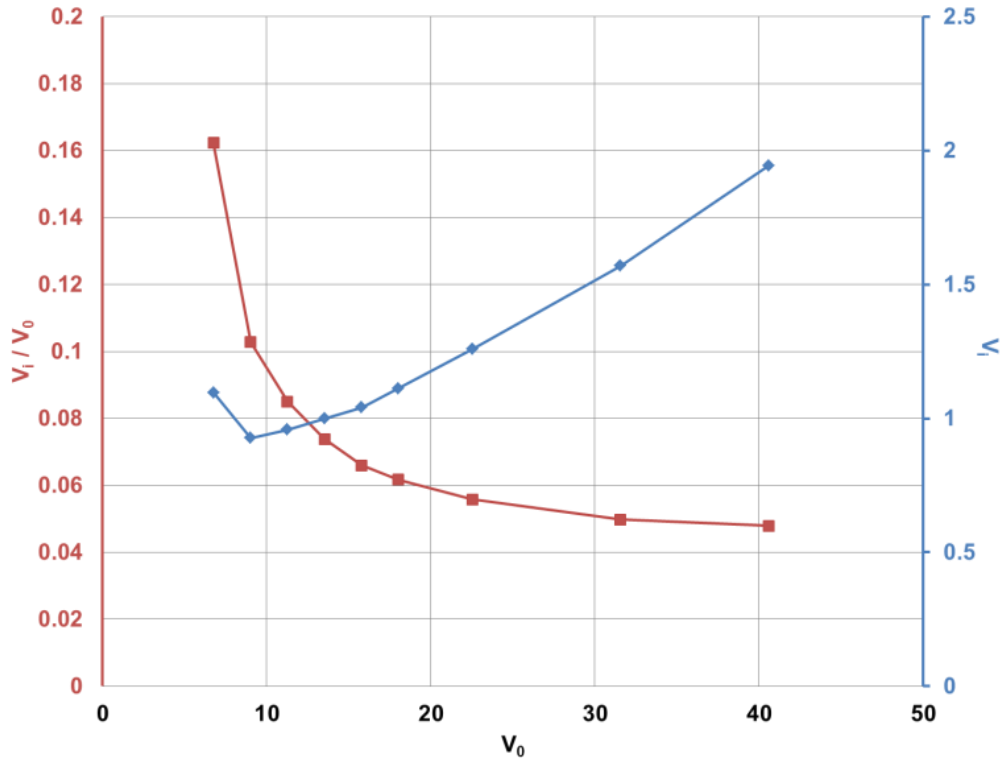


**Fig. A6** Figure showing the measured ratio ( $V_i/V_0$ ) of the inside ( $V_i$ ) and outside ( $V_0$ ) lens potentials as a function of outside lens potential at different analyzer pass energies (red). Outside lens potential ( $V_0$ ) is fixed at the set analyzer transmission energy ( $TE=V_0$ ) and the inside lens potential is set to maximize Faraday current at each transmission energy. The maximized inside lens potential ( $V_i$ ) is plotted as a function of outside lens potential ( $V_0$ ) (blue).

### A5 Energy Calibration

An energy calibration was performed to establish the analyzer work function as well as resolution. When vacuum emitted electrons leave the sample surface, their kinetic energy is reference to the vacuum level of that sample. However, when entering a closed system with a different work function  $\phi_{\text{Analyzer}}$  a contact potential is setup and the kinetic energy of the

Appendix A: UCSB Electron Energy Analyzer

electron must then be referenced to the analyzer and is not dependent of sample work function, this relation is found in **Fig. A7**. [7]

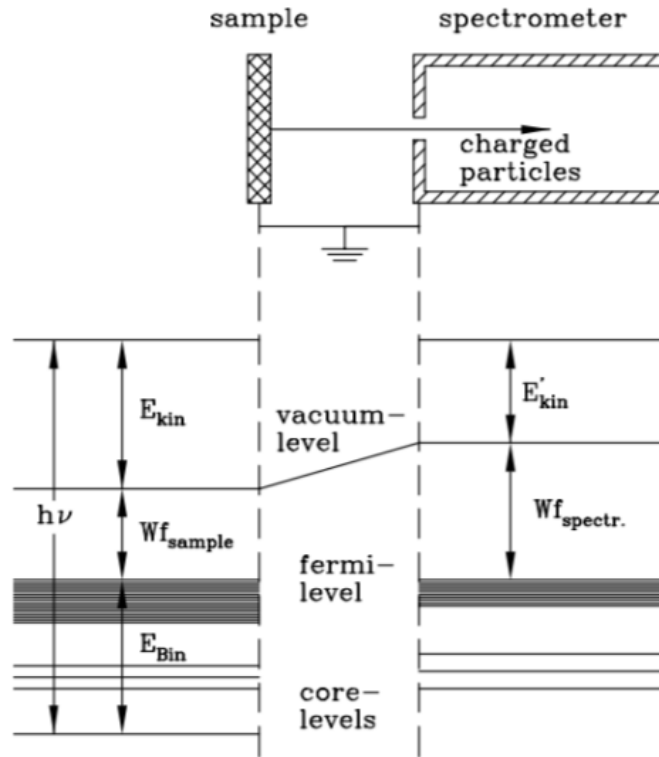


*Fig. A7 Figure showing the contact potential setup when the sample and analyzer are brought into equilibrium.*

When operating the analyzer, the potentials between in inside and outside plate are set such that their average is equal to the analyzer transmission (or pass) energy (TE):

$$qV_{average} = q \frac{V_{inside} + V_{outside}}{2} = TE$$

## Appendix A: UCSB Electron Energy Analyzer

From the analyzer geometry and electrostatics, we know that this pass energy is also given by:

$$TE = q * 2.27 * (V_{inside} - V_{outside}) = q * 2.27 * \Delta V$$

An example of setting the voltages:

If we want  $\Delta V=3$ , then  $TE=6.76$  eV and  $V_{inside}=8.262$  and  $V_{outside}=5.262$

If the voltage is set symmetrically on the inside and outside analyzer plates, then an electron entering the analyzer and exiting the analyzer will be given the same acceleration or deceleration, therefore analyzer transmission energy (TE) is not part of the analyzer calibration.

To calibrate for analyzer work function it is common for a metal sample to be used. [8] In this calibration Ti/Au (30/300 nm) was deposited by electron beam deposition on to clean polished sapphire. The metal was then cesiated and electron current was maximized using a 405 nm laser. When exiting with a known energy, the highest energy electrons are excited from the Fermi level of the metal gaining energy  $h\nu$ . To pass through the analyzer an acceleration (or deceleration) of  $V_{cathode}$  is applied to the sample. The relations of these energies are shown schematically in **Fig. A8**. To find analyzer work function we simply add the electron energy ( $E= h\nu$ ) to the cathode potential ( $V_{cathode}$ ).

$$h\nu + qV_{cathode} = \phi_{Analyzer}$$

Appendix A: UCSB Electron Energy Analyzer

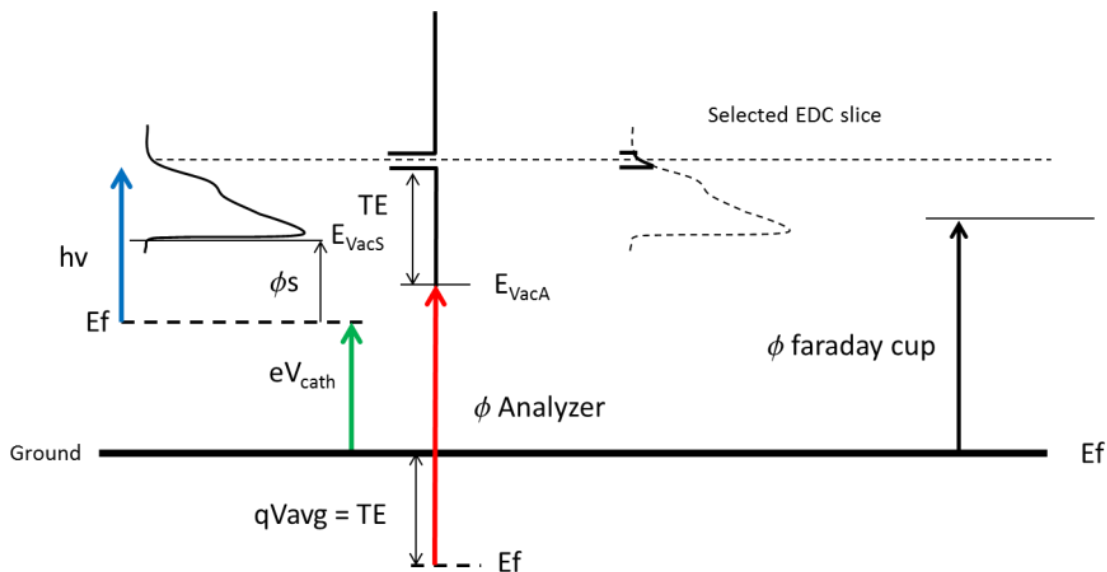


**Fig. A8** Schematic diagram showing how electrons pass through the analyzer. Calibration is performed to measure  $\phi_{\text{Analyzer}}$ .

Energy distribution curves were taken for several pass energies; the electron path is modified by the analyzer and a different work function needs to be calibrated at each pass energy. The measured analyzer work functions as well as a linear fit as a function of pass energy are given in **Fig. A9** and **Fig. A10**.

Appendix A: UCSB Electron Energy Analyzer

<u><math>\Delta V</math></u>	<u>Vent</u>	<u>Vtop&amp;bottom</u>	<u>Vinside</u>	<u>Voutside</u>	<u>Work Function</u>	<u>Pass energy</u>
3	6.762	6.762	8.262	5.262	4.722	6.762
4	9.016	9.016	11.016	7.016	4.808	9.016
5	11.270	11.27	13.77	8.77	4.895	11.27
6	13.524	13.524	16.524	10.524	4.982	13.524
7	15.778	15.778	19.278	12.278	5.069	15.778
8	18.032	18.032	22.032	14.032	5.155	18.032
10	22.540	22.54	27.54	17.54	5.329	22.54
14	31.556	31.556	38.556	24.556	5.676	31.556
18	40.572	40.572	49.572	31.572	6.023	40.572

**Fig.A9** Table showing the potential setting for the analyzer at different pass energies. This table includes the calibrated analyzer work function.

## Appendix A: UCSB Electron Energy Analyzer

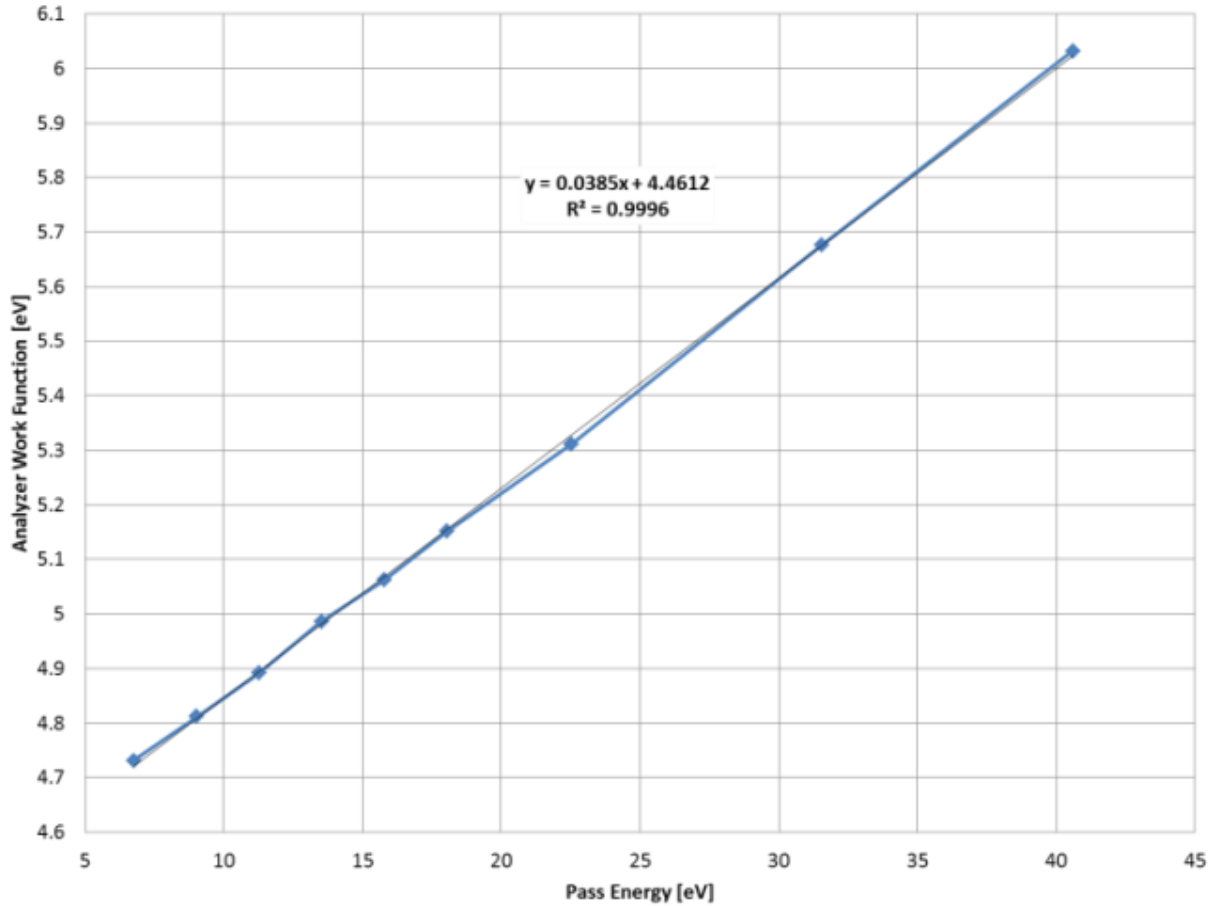


*Fig. A10* Figure showing the measured analyzer work function at different pass energies. A linear fit can be used to extrapolate between measured points.

The measured electron energy distribution of the high energy Fermi step is broadened by the thermal distribution of the electrons, as well as the analyzer. The high energy ballistic electrons (those at  $E = h\nu$ ), therefore, correspond to the inflection point of the high energy Fermi step ( $V_{\min}$ ). This value of the cathode potential ( $V_{\text{cathode}}$ ) set at this inflection point corresponds to electrons whose energy equals the exciting photon energy ( $E = h\nu$ ). This inflection point in the energy distribution curve (EDC) is found by taking the derivative of the

## Appendix A: UCSB Electron Energy Analyzer

EDC, dEDC and finding its minimum. Additional measurements were made at varying exciting energies to assure there was no additional broadening at the Fermi step due to scattering. The EDC and dEDC of the gold reference sample, exciting at 405 nm with pass energy of 11.27 eV is shown in **Fig. A11**.

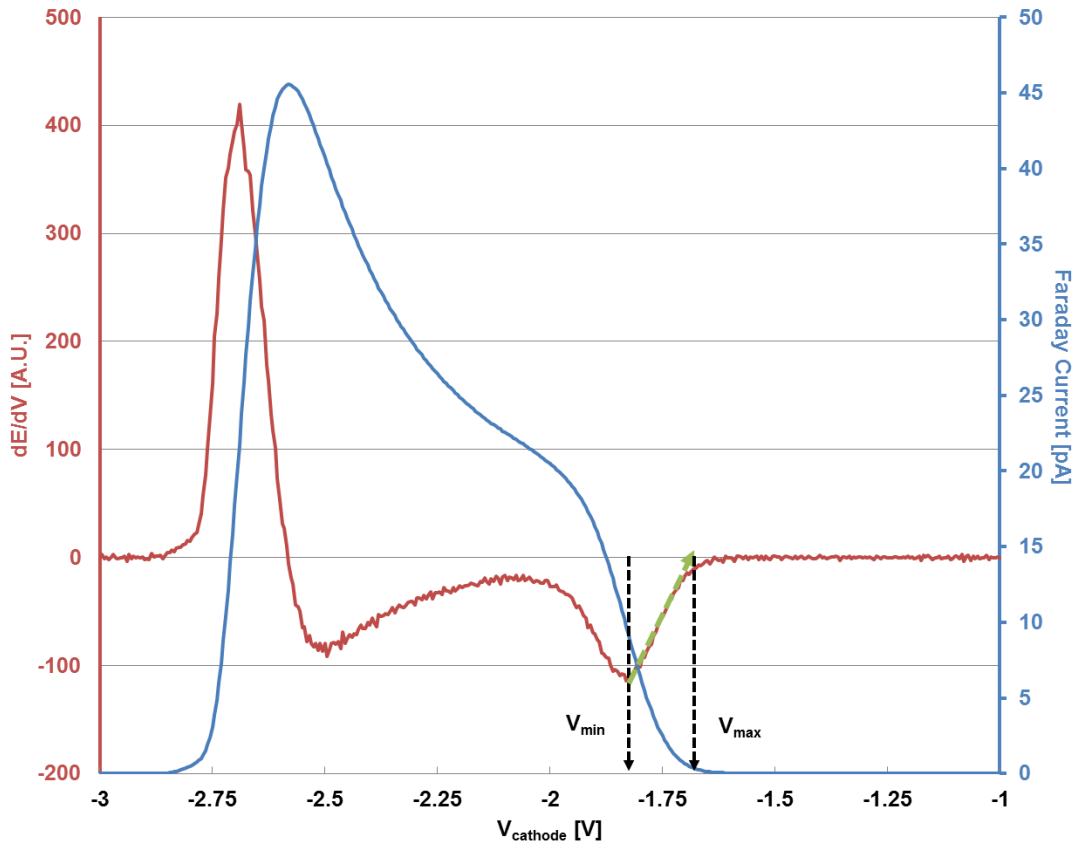


**Fig. A11** Figure showing an energy distribution curve (blue) as well as its derivative (red). High energy minimum ( $V_{min}$ ) and extrapolated maximum ( $V_{max}$ ) are used to identify peak energy as well as energy resolution.

## Appendix A: UCSB Electron Energy Analyzer

To find the analyzer resolution at a given pass energy, the high energy threshold if the dEDC is determined ( $V_{max}$ ). The measured resolution is therefore given by:

$$\Delta E = |V_{max} - V_{min}| - 2kT$$

The measured value for energy resolution as well as the line of 0.8% is plotted as a function of analyzer pass energy in **Fig. A12**.

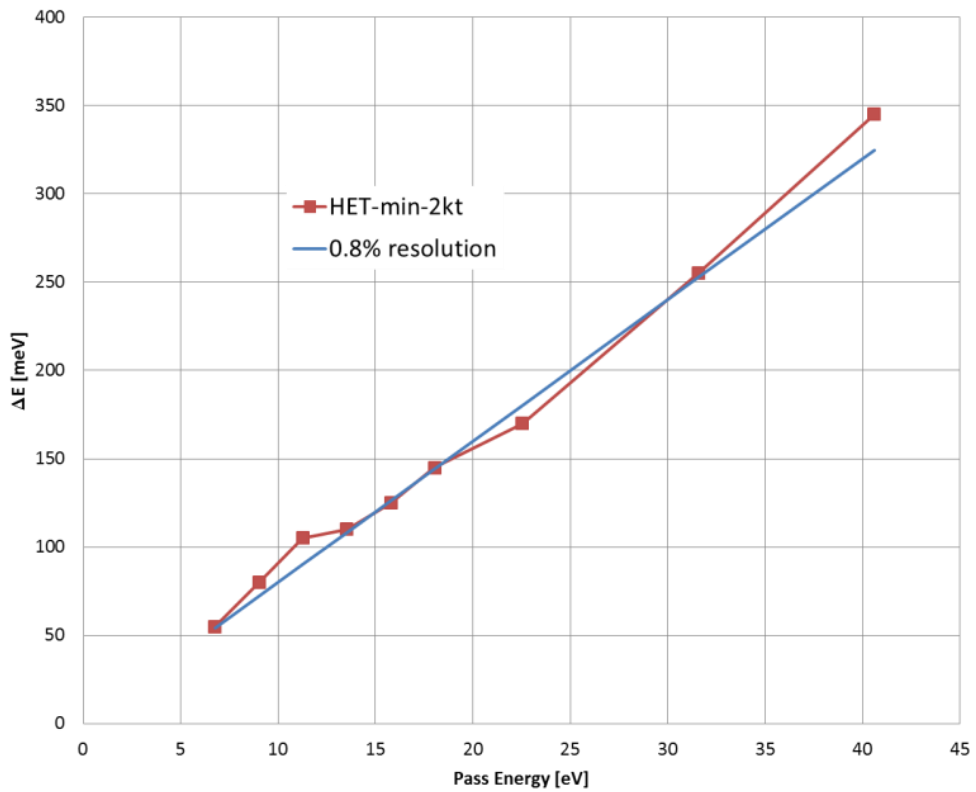


**Fig. A12** Measured resolution at different analyzer pass energies using 1 mm entrance and exit slits. Measured values fit well to the quoted value of 0.8%.

## Appendix A: UCSB Electron Energy Analyzer

The transmission of electrons through the analyzer is dependent on the analyzer pass energy. EDCs were taken at different pass energies. At each pass energy entrance slit current was monitored and assumed to be approximately equal to the total cathode current. The analyzer transmission efficiency is given by the ratio of the integrated faraday current of the EDC spectra to the total cathode current. Analyzer efficiency and total integrated Faraday current is plotted in **Fig. A13**.

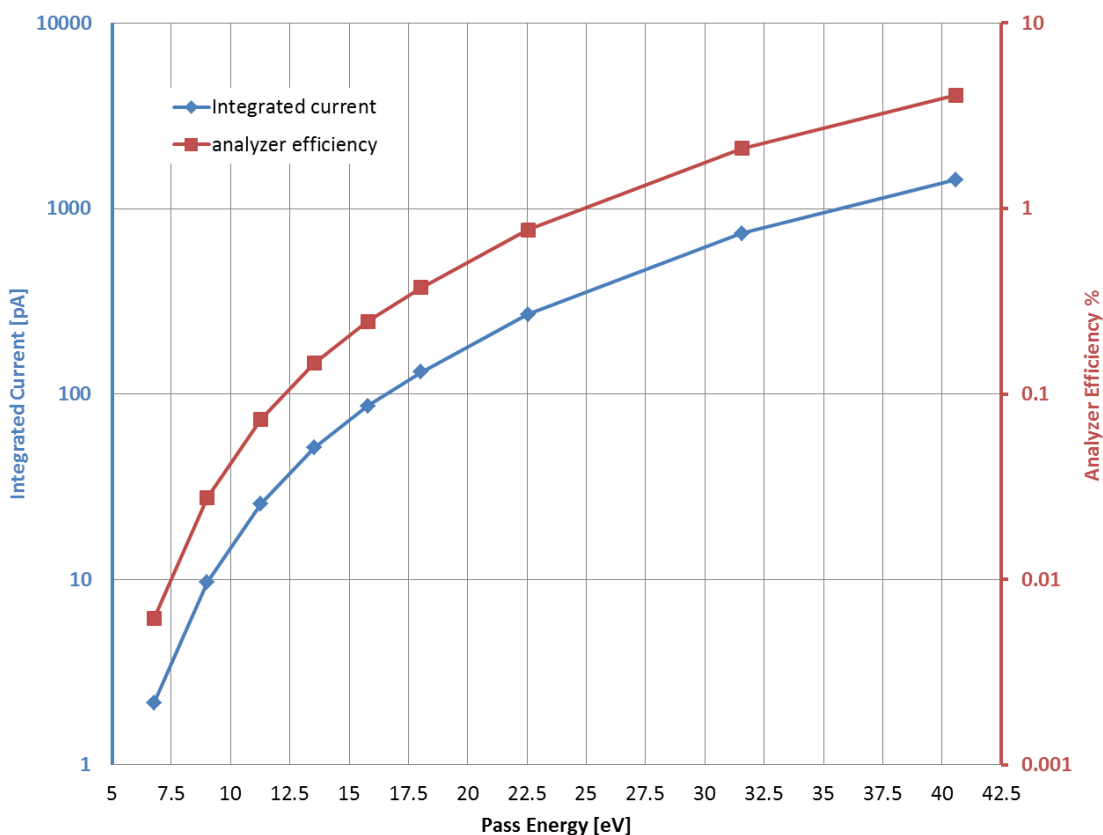


*Fig. A13* Figure showing analyzer efficiency (red) and integrated faraday current (blue) plotted as a function of analyzer pass energy.

## Appendix A: UCSB Electron Energy Analyzer

### A6 Analyzer System Operation

When introducing a sample into the vacuum chamber for measurement the following procedure should be followed to avoid accidental venting of chamber, damage of pumps or gauges **Fig. A14**.

	Step	Location	Comment
1	Disconnect electrical	cesium wire, control tower rack, load-lock ion gauge controller	Assure battery is disconnected, assure Kepco supply is off, turn load lock ion gauge off
2	turn on turbo	turbo pump control box	press power button on turbo control box, pump down until $<e-4$ torr is achieved
3	open turbo gate valve	control tower rack	open gate turbo pump gate valve
4	turn off turbo	turbo pump control box	press power button on turbo control box, allow load lock to vent to atmosphere
5	load sample	load lock	load sample onto sample holder, close door when finished
6	turn on turbo	turbo pump control box, load-lock ion gauge controller	press power button on turbo control box, allow turbo to pump until $<e-4$ torr is achieved, turn on load-lock ion gauge
7	turn on heater lamp	heater lamp power supply	turn on heater lamp to manufactures recommended current and voltage setting, assure load lock temperature does not exceed 200C
8	open ion pump valve	load lock ion pump	after load-lock ion gauge reaches $5e-7$ torr, open ion pump gate valve
9	close turbo gate valve	control tower rack	close gate turbo pump gate valve
10	turn off heater lamp	heater lamp power supply	turn off quartz heater lamp
11	open chamber gate valve	control tower rack	after load-lock ion gauge reaches $5e-7$ torr, open main chamber gate valve
12	transfer sample	transfer arm	transfer sample onto sample mount
13	close chamber gate valve	control tower rack	after retracting transfer arm, close main chamber gate valve

## Appendix A: UCSB Electron Energy Analyzer

*Fig. A14 Figure showing standard operating procedure for loading of a sample into the analyzer chamber.*

The bake out lamp used in the load-lock is a 100 W 12V quartz halogen lamp. The lamp is operated using a variable transformer with the current monitored using an inductive current probe. It is advised to not exceed 8 amps lamp current during bake out. Typical bake out is complete when pressure has stabilized is around  $2 \times 10^{-7}$  torr, typically 1 hour.

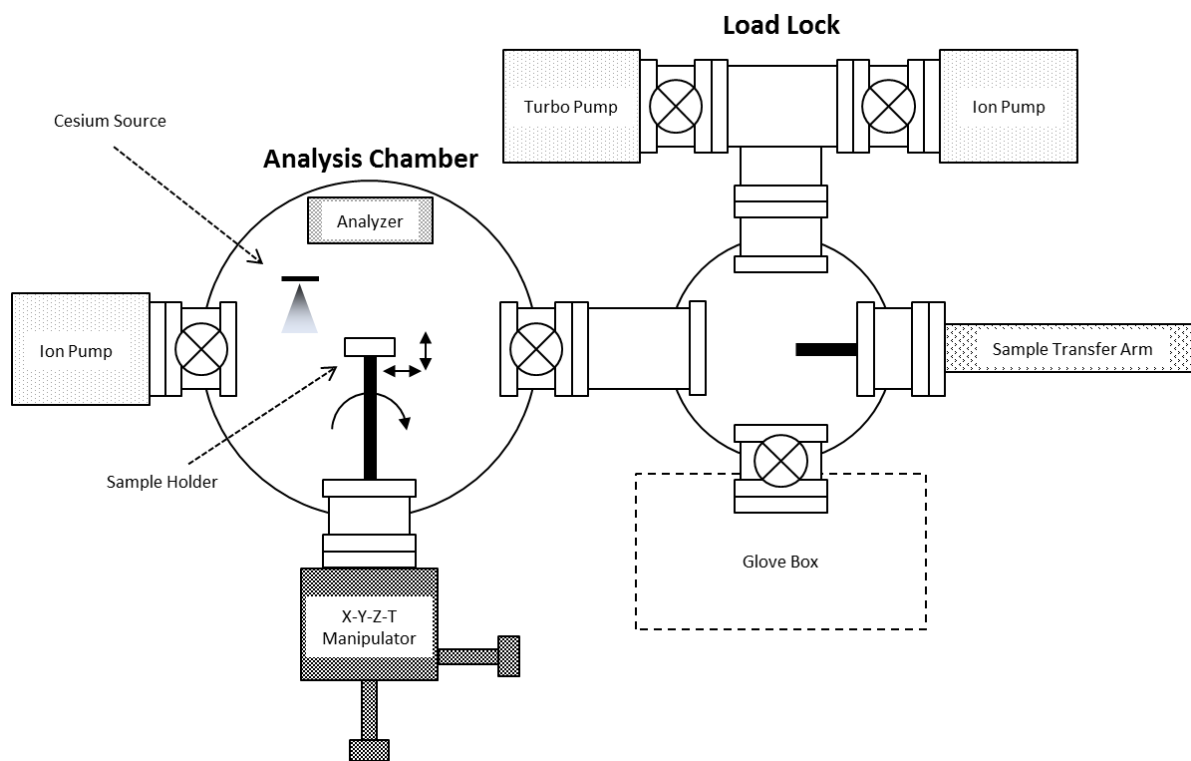


*Fig. A15 Diagram showing the components of the vacuum load lock and analysis chamber.*

### **A7 Cesium Procedure**

Cesium to achieve NEA is performed using a SAES Getters Alkali Metal Dispenser, model #CS/NF/8/25 FT 10 + 10. The cesium dispenser consists of an alkali metal salt mixed with a reducing agent. In general the alkali metal are in the form of a chromate ( $\text{Cs}_2\text{CrO}_4$ ).<sup>[9]</sup> To dispense cesium, a bias is applied across the dispenser and the generated current (from a resistive element) heats the dispenser. This heating initiates the reduction reaction to generate elemental cesium.

Inside the chamber the cesium source is mounted facing the manipulator. The manipulator is set to 1.5'' position on the translation stage and rotated counter-clockwise to sit in line with the cesium source. A window on the flange containing the cesium source allows access to properly align the sample with the source. Above the cesium source there is a wire which is biased positively with respect to the sample to collect all electrons and monitor cathode current during cesiation. A battery is used to bias the wire and the sample is grounded, this is shown in **Fig. A16**.

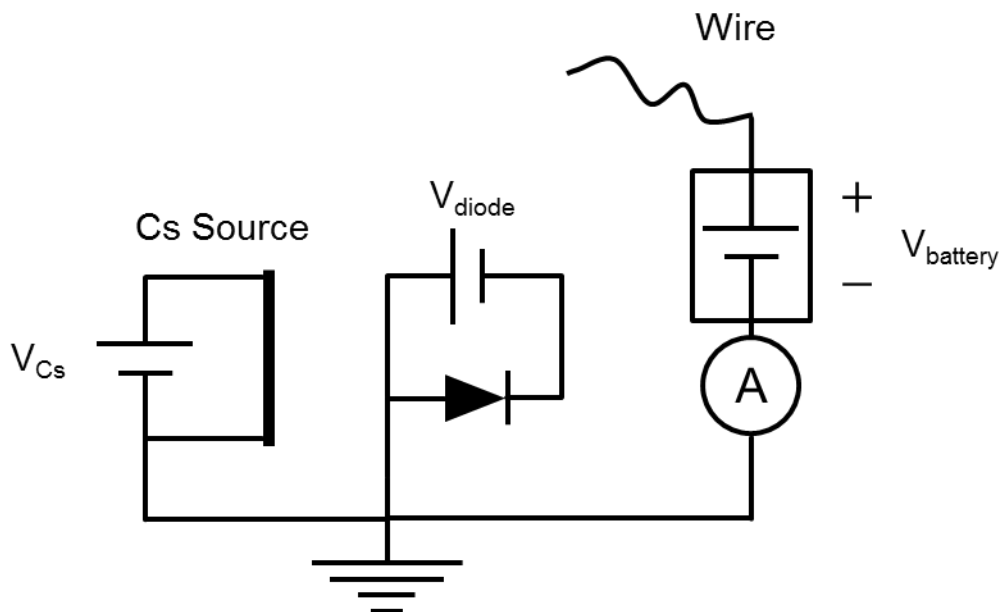


*Fig. A16* Wiring diagram used for cesiation of electroemission sample.

During cesiation the battery used is a 96 V battery consisting of a series of 9 V batteries. The cesium source is powered by a DC supply with the bias referenced to ground. For electroemission samples, electron current can be monitored using a small bias (1 mA) to avoid heating. Optical access is gained through a UV quartz window. For photoemission samples, a 405 nm laser ( $\sim 5\text{mW}$ ) can be used to monitor electron current, with the cathode referenced to ground.

Cesiation is performed at 4.5 A cesiation current ( $V_{Cs}$ ). Before moving the sample into position, cesium should be operated at 4.5 A for approximately 4 minutes to reduce outgassing during cesiation. After outgassing, chamber pressure should be  $\sim 2 \times 10^{-10}$  torr during cesiation. Total cesiation time should be less than 1 hour. Optimization of cesiation is performed by monitoring the cesiation current over time, allowing it to reach a maximum, and

## Appendix A: UCSB Electron Energy Analyzer

then reduce by 20% of the maximum value. After cesiation, the sample is returned to the measurement position. The cesium dispenser should remain at 2A current at all times when under vacuum to reducing outgassing.

### **A8 Potential Analyzer Problems**

#### **Analyzer Plate Surface**

For optimal analyzer performance all surfaces that “see” electrons should have a uniform potential, in addition an electron that collides with such surface should not be reflected. The Comstock analyzer is composed of polished copper. To reduce field distortion and reflection effects, all surfaces were coated with a thin layer of Aerodag-G colloidal graphite. After spraying with aerosol colloidal graphite, all parts were placed under heat lamp for 1 hour before re-assembly.

#### **Avoiding Space Charge**

If the cathode current becomes too high, electrons can interact during transit to the analyzer. These space charge effects can cause a blooming of the electrons beam. Maximum electron current that can pass through a given volume is proportional to the three halves power of the electron energy. To prevent operating in a space charge limited current regime, the maximum electron current is given by [5], [10]:

$$I_{max} \approx 38.5 \left(\frac{D}{S}\right)^2 E^{\frac{3}{2}} [\mu A]$$

## Appendix A: UCSB Electron Energy Analyzer

Here  $D$  is the aperture diameter,  $s = 8$  mm is distance between apertures in the entrance slit lens assembly and  $V$  is the electron energy/ $q$ . For a 1eV electron using 1mm aperture diameter, the electron current should not exceed 600 nA.

### **Reducing magnetic Field Effects**

When measuring low energy electrons, special care must be taken to reduce all stray magnetic fields. This includes earth's magnetic field, which ranges from 250 to 650 milliGauss. A 10 eV electron, traveling perpendicular to earth's magnetic field has a bend radius of approximately 16 cm. A 1 eV electron has a bend radius of around 5cm. These dimensions are on the order of the total path length of the electron from the sample, through the analyzer, to the Faraday cup. The analyzer is enclosed in a 0.062" thick mu-metal box to reduce the effects of earth's magnetic field. Stainless steel parts can also become magnetized through cold working in machining processes. To reduce the magnetic field in a magnetized steel part annealing can be performed. Parts can be heated to 1075 C and quenched. This effect of annealing and subsequent quenching removes the magnetic Martensite (BCT) domains and results in a non-magnetic Austenite (FCC) stainless. After thermal treatment a surface oxide can be removed using 2% HF by volume in a 20% Nitric water solution ( $\text{HNO}_3\text{:H}_2\text{O}$ ). This solution should be heated to 60°C.

### **Cleaning Contacts**

## Appendix A: UCSB Electron Energy Analyzer

Cleaning coaxial contacts is of particular importance when measuring small electron currents. It is possible for a coaxial connector to become contaminated and its contact resistance between the inner contact and outer (ground) shield be reduced. This increase in resistance is particularly important when a large bias is applied to extract electrons. For instance: a 100 V bias with a 1 M $\Omega$  resistance will result in 100 microamps of parasitic current, this can be  $10^5$  times larger than the nA electron current measured. In addition, poorly shielded cables can add noise by vibration and movement by introducing charges by electrostatic (or triboelectric) effects. Faraday cup and cesiation currents are monitored using EOC CAB-LN1 low noise cables, whose insulation resistance is measured to be  $>10^{14}$   $\Omega$ . All coaxial connectors should be cleaned with ultra-pure isopropanol and dried completely.

## References

- [1] “Comstock Electrostatic Energy Analyzer Manual.” .
- [2] J. Iveland, M. Piccardo, L. Martinelli, J. Peretti, J. W. Choi, N. Young, S. Nakamura, J. S. Speck, and C. Weisbuch, “Origin of electrons emitted into vacuum from InGaN light emitting diodes,” *Appl. Phys. Lett.*, vol. 105, no. 5, p. 052103, Aug. 2014.
- [3] J. Iveland, L. Martinelli, J. Peretti, J. S. Speck, and C. Weisbuch, “Direct measurement of Auger electrons emitted from a semiconductor light-emitting diode under electrical injection: identification of the dominant mechanism for efficiency droop,” *Phys. Rev. Lett.*, vol. 110, no. 17, p. 177406, Apr. 2013.
- [4] H.-J. Drouhin and M. Eminyan, “Simple concepts in the measurement of the energy distribution and spin polarization of an electron beam,” *Rev. Sci. Instrum.*, vol. 57, no. 6, pp. 1052–1060, 1986.
- [5] “Electrostatic Energy Analyzers Technical Brochure.” .
- [6] A. Adams and F. H. Read, “Electrostatic cylinder lenses II: Three element einzel lenses,” *J. Phys. E.*, vol. 5, pp. 150–155, 1972.
- [7] GmbH SPECS, “PHOIBOS hemispherical Energy Analyzer User Manual.” SPECS.
- [8] R. Schlaf, “Calibration of Photoemission Spectra and Work Function Determination.” pp. 1–4.
- [9] P. Della Porta, C. Emil, and S. Hellier, “Alkali metal generation and gas evolution from alkali metal dispensers,” 1968.
- [10] C. E. Kuyatt and J. A. Simpson, “Electron Monochromator Design,” *Rev. Sci. Instrum.*, vol. 38, no. 1, pp. 103–111, 1967.

## Appendix B: Electroemission Device Design

*The fabrication process and device design of LED electroemission samples is discussed. Cleaning procedures necessary to obtain negative electron affinity are covered as well.*

### **B1 LED Epitaxial Structure**

LED samples under study were grown by metal organic chemical vapor deposition (MOCVD) on flat (0001) sapphire substrates. The initial studies were performed on commercial LEDs obtained from Walsin Lihwa (Taiwan). LEDs measured in the control experiments, described in chapter two, were obtained from Seoul VioSys.

Secondary ion mass spectroscopy (SIMS) measurements were performed by Evans Analytical Group on the Walsin LED sample. These measurements indicated that the Walsin sample had approximately 200 nm thick p-GaN, 8 InGaN/GaN quantum wells and included an AlGaN electron blocking layer (EBL).

SIMS measurements were also used to indicate the optimal etch depth when defining the mesa etch for the n-contact. SIMS profiles are shown in **Fig. B1**.

## Appendix B: Electroemission Device Design

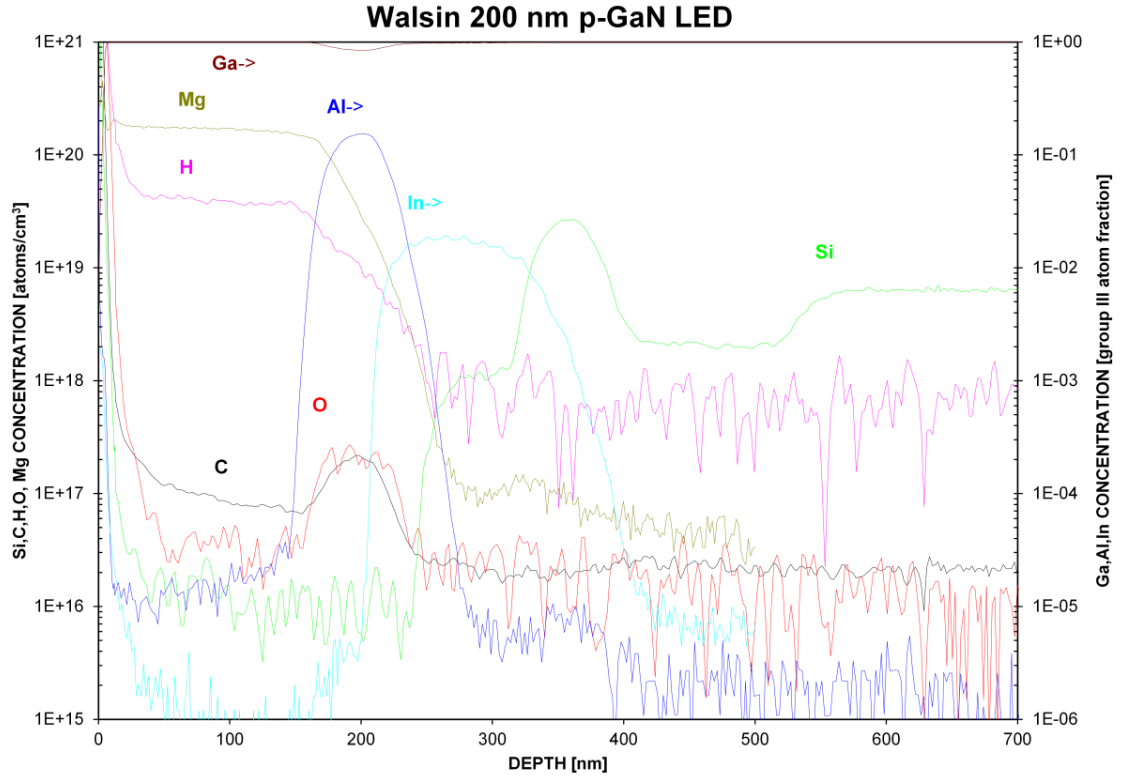


*Fig. B1 SIMS profile for the Walsin commercial LED sample measured in electroemission.*

### **B2 LED Device Design**

There are two generations of devices design used in the electroemission (EE) measurement. In the first study [1] there were three devices on a single (approximately 1 cm<sup>2</sup>) sample that were parallel to the n-contact. In the “parallel” geometry, the p-contact was 500 μm on a side, large isolate p-contacts were 2.5 mm on a side and had a 100 μm by 1000 μm finger that made contact to the 500 μm p-contact. The samples were etched to make the 8 mm by 1.5 mm n-contact. The 500 μm p-contact contained an array of 27X27 10 μm apertures to expose the p-GaN surface. The “parallel” device geometry is shown in **Fig. B4**.

## Appendix B: Electroemission Device Design

In all further studies on LED EE, including the pn junction control study [2], “concentric” device geometry was used. The “concentric” device consisted of a 500  $\mu\text{m}$  diameter p-contact with 632 10  $\mu\text{m}$  apertures exposing the p-GaN surface. The p-contact was contacted with a large isolated half dumbbell shaped contact 4 mm in diameter with a 1.5 mm X 5 mm contacting pad. The n-contact was made after etching and a section of an annulus with an inner-diameter of 6 mm and outer-diameter of 9 mm. The “concentric” device design is shown in **Fig. B2 and B3**.

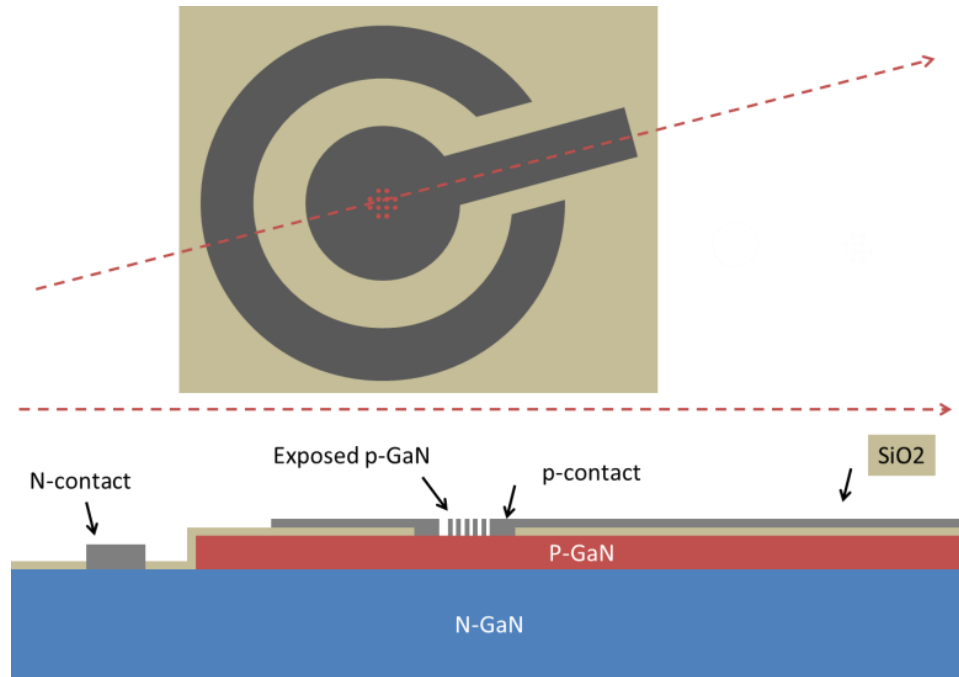


**Fig. B2** Figure showing the “concentric” contact design in cross section.

There are advantages to the “concentric” device design. First, this design was shown to reduce field distortion effects seen in the “parallel” contact design. The large isolated p-contact provides the analyzer with an image of a uniform potential (at  $V_{\text{cathode}}$ ). In the

## Appendix B: Electroemission Device Design

“parallel” contact design, electrons were likely distorted by large diode bias (seen at high diode current). A second advantage to the “concentric” device design is its use in photoemission experiments. With a large isolated p-contact, a light source can more easily excite the aperture region and avoid surround regions that are at a different potential. Photoemission experiments in the “parallel” contact design can result in a convolution of photoemitted electron referenced to the p-contact as well as to the nearby n-contact.

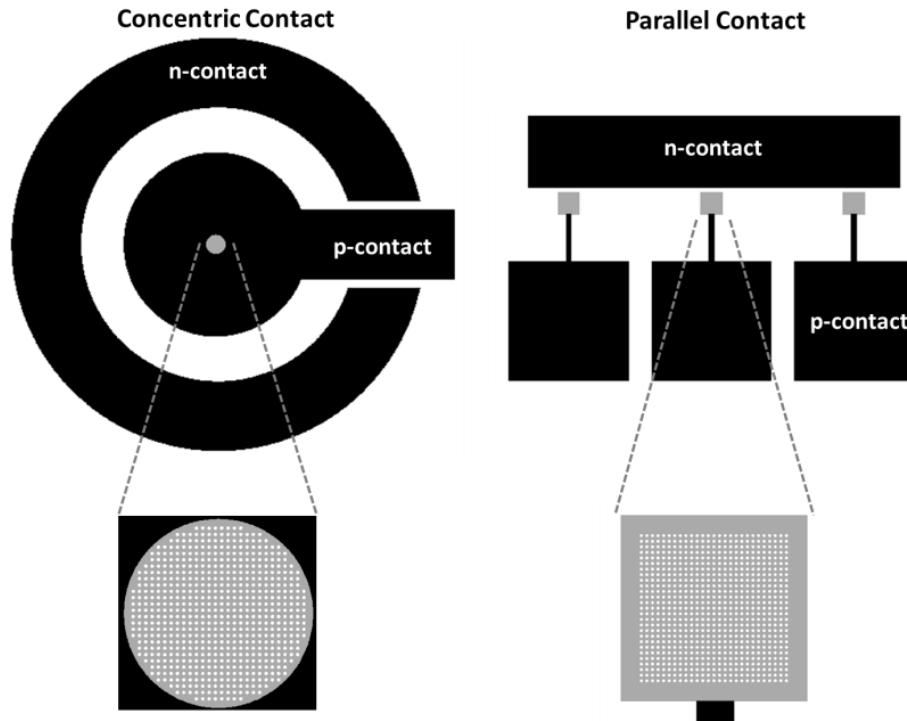


*Fig. B3 Showing the contact layout for the “parallel” and “concentric” contact design.*

### **B3 Sample Cleaning for NEA cathodes**

The cleaning of fabricated electroemission samples for NEA cathodes is performed in three steps:

## Appendix B: Electroemission Device Design

1. After sample processing, samples are cleaned with a series of organic solvent cleans. First, the final lithography photoresist is stripped with Microposit Remover 1165. Samples submerged in 1165 are heated in an 80 C° bath with sonication at low power. Samples are then rinsed and placed in a solvent bath and sonicated on low power at room temperature for 5 minutes. Solvent cleaning is done in acetone followed by isopropanol. After the ISO cleaning, samples are rinsed with DI water and blown dry with nitrogen.

2. To further remove any organic residue, a H<sub>2</sub>O<sub>2</sub>:H<sub>2</sub>SO<sub>4</sub> (Piranha) dip is performed. The solution is mixed in a ratio of 1:3 H<sub>2</sub>O<sub>2</sub>:H<sub>2</sub>SO<sub>4</sub>. It is advised that, when preparing the Piranha solution, the hydrogen peroxide be added to the sulfuric acid.[3] After the solution is prepared, samples are lowered in slowly. Acid safe tweezers may be used; however, they must be Teflon (PTFE). Piranha is an aggressive oxidizer and can react violently with many polymers. The Piranha clean is performed for 30 seconds, followed by a DI rinse for 3 minutes.

3. The last step before vacuum introduction is an HCL: ISO clean. This clean is performed in the nitrogen purged glove box. Samples should be introduced and the glove box should be purged at least 10 minutes prior to performing the HCL : ISO clean. After purging, the samples are dipped into the HCL: ISO solution (described below) for 20 seconds. Samples are then rinsed with ultra-high purity isopropanol, blown dry with nitrogen and placed onto the sample holder and introduced into vacuum.

## Appendix B: Electroemission Device Design

The HCL: ISO solution is prepared by dissolving hydrochloric acid vapor into isopropanol. The HCL solution should be high-purity with a concentration of 37 %. The isopropanol solution should also be ultra-high purity. Two beakers (one HCL and one ISO) are placed together in a sealed container and allowed to mix over a period of ~18 hours. The HCL concentration saturates at about 15% after 100 hours. [4] This method has proven useful with p-GaN for high quantum efficiency cathodes.[5], [6]

### **B4 Device Process**

A process flow for the electroemission samples is shown in **Fig. B9**.

#### **Sample Activation**

Prior to processing, MOCVD grown samples should be activated to remove hydrogen responsible for acceptor compensation. To do so, a 10 minuet anneal in atmosphere at 600 C should be performed using the Furnace located in the MOCVD lab. Alternatively, the rapid thermal processor (AET RX6) can be used.

#### **SiO<sub>2</sub> Deposition Steps**

Deposition of SiO<sub>2</sub> for passivation and p-GaN protection was performed using a Plasma-Therm model 790 plasma enhanced chemical vapor deposition (PECVD) tool. The SiO<sub>2</sub> is produced using SiH<sub>4</sub>/He 2%/90% with N<sub>2</sub>O gas. The anode is operated at 250C during deposition and pre-clean. Prior to each deposition step, the tool is vented and the inside is wiped out with water soaked cleanroom wipe to assure a clean chamber surface. A 10 minuet pre-clean is then performed prior to deposition. The 300 nm sample deposition is performed

## Appendix B: Electroemission Device Design

in two steps, with 150 nm deposited at each step. In between steps, a DI water dip is performed on the samples and the samples are blown dry with the nitrogen gun. A monitor wafer of Silicon should be included with the deposition to calibrate thickness and SiO<sub>2</sub> etch rate.

### Photolithography Steps

The standard “parallel” and “concentric” contact designs utilize a clear field mask with an all negative resist process. The photoresist process for nLOF-2020 is shown in **Fig. B5**.

AZ nLOF 2020 / SUSS MJB-3	
STEP	COMMENT
Spin	HMDS, 3000rpm, 20000 rpm/sec , 30 sec
Bake	95 C hot plate, 60 sec
Spin	AZ nLOF 2020, 3000rpm, 20000 rpm/sec , 30 sec
Remove Edge Bead	Remove edge bead, 0.5 to 1mm on each side, blow clean with N2 gun
Bake	110°C, 90sec
Expose	9.5 sec, 7.5mW/cm <sup>2</sup>
Post Exposure Bake	110°C, 60 sec
Develop	AZ300-MIF, 50 sec
Rinse	DI rinse, dump water three times

*Fig. B5 Showing the steps lithography steps for nLOF 2020*

Exposure is performed using a SUSS MJB-3 contact aligner. No i-line filter should be used. The contact aligner masks are chrome on 4” soda lime.

Prior to lithography it is important to clean samples with Acetone, Isopropyl Alcohol sonicating on low power for 3 minutes each. After, a solution of Liqui-Nox and DI water

## Appendix B: Electroemission Device Design

should be used to remove any small particles. Lastly, a rinse in DI water should be performed at least three times to assure all residual chemicals are removed.

During sample alignment, it is important to make light contact, lower the sample completely, and bring it directly back up into light contact. Following this procedure assures that the leveling mechanism is engaged on the aligner. In addition, it is important to inspect and clean the mask after each exposure, as there is only a single device on the mask any particles will prevent proper alignment and intimate contact with the mask. Furthermore, because this process is an all negative resist with a clear field mask, any particles on the mask will not be exposed and will be developed away. A clean mask is especially important during the p-contact step, as any developed portion will be metalized during subsequent deposition.

Liftoff of photoresist is performed using Microposit Remover 1165. The 1165 should be heated at 60 to 80C. If a fast liftoff is necessary, samples can be place in heated sonication on low intensity. Typical time for fast liftoff is 15 minutes.

### **De-scum Steps**

After each lithography step a de-scum step is necessary to clean the surface and prepare the surface for wet etching if applicable. For each processing step that has exposed n-GaN oxygen plasma can be used. In this case a Technics PEII is used. Pressure should be below 300 mTorr prior to turning on the RF plasma. Plasma cleaning should be performed at 100 W for 30 seconds. For each step that has exposed p-GaN (even those where no PR is covering the SiO<sub>2</sub>), an UV ozone is performed. The ozone cleaning is done using a PR-100 UVP reactor. The samples is inserted into the ozone chamber and cleaned for 20 minutes.

## Appendix B: Electroemission Device Design

### Mesa-Etch

The mesa-etch through the p-GaN and active region to the n-GaN is performed using inductively coupled plasma (ICP) etching. One of two Panasonic ICP tools can be used for the etch ICP#1 (Panasonic E626I) or ICP#2 (Panasonic E640). In both cases it is important to properly clean the silicon carrier wafer with Acetone and Isopropanol to assure that the chuck does not encounter a vacuum error. Samples are mounted on the Silicon carrier wafer using a very small amount of vacuum oil. In addition, the chamber with the clean carrier wafer (not containing the samples) should be seasoned with a CF<sub>4</sub>/O<sub>2</sub> clean for 5 minutes prior to etching. Etch rates are shown in Fig. X ICP #2 etch recipe contained an oxide pre-etch to either etch SiO<sub>2</sub> or to remove any native oxide on the GaN surface prior to etching.

Tool	GaN Etch Rate [nm/min]
ICP #1 Cl <sub>2</sub> /N <sub>2</sub>	270
ICP #2 Cl <sub>2</sub> /Ar	640

*Fig. B6 Approximate etch rates for ICP #1 and #2*

Etch parameters for ICP #1 and #2 are shown in **Figs. B7 and B8**.

Step height should be measured after etching to assure proper etch depth. Etch depth can be measured using the Dektak 6M step profilometer. Alternatively, the Olympus LEXT confocal microscope can be use.

### Metal Deposition

Deposition of metal contacts is performed using electron-beam evaporation. Prior to any metal deposition a de-scum step should be performed (see de-scum). After de-scum, a HCL

## Appendix B: Electroemission Device Design

dip should be performed for 30 seconds, followed by a DI water rinse. Samples should be placed inside deposition chamber promptly after HCL dip.

When depositing metal for the n-contact and large isolated p-contact e-beam #3 (Temescal VES-2550) can be used. Samples should be secured on the chuck using Copper clips or Kapton tape contacting only the edges. Metal deposition should not start until pressure is below  $3 \times 10^{-6}$  Torr. For the n-contact and isolated p-contact 30/300 nm of Ti/Au are used. Deposition rates for the Ti are 1A/sec for 10 nm, 30 second ramp to 2 A/sec for the remainder of the deposition. Au deposition rates are 1 A/Sec for 10 nm, 30 sec ramp, 2.5 A/Sec from 10 nm to 200 nm, 30 sec ramp, then 4.5 A/Sec for the remainder of the deposition.

During the Pd/Au p-contact deposition the flat chuck on e-beam #3 (Temescal VES-2550) should not be used. The Pd and Au sources are located on two different guns within the chamber, this gun position results in a shadowing effect that is observed in the small 10  $\mu$ m apertures. To avoid the shadowing effect, the angled chuck can be used. In this configuration the Pd is deposited with the chuck facing the rear of the chamber. After Pd deposition, the chuck is removed and rotated 180 degrees for Au deposition. To avoid interrupting the deposition to rotate the chuck, e-beam #4 (CHA Industries SEC-600-RAP) can be used. In e-beam #4 the sources are rotated between deposition and remain in the same position.

Appendix B: Electroemission Device Design

Process Recipe No	175	Wafer Pusing For Neut					DO					
Title	1wGaN	Start Step For Neut					8					
Comment	Cf4 Cl2 Ar	C-HE Start Flow Rate					30					
End Step	9	HE Vacuum Comp. Press.					30					
A: BCL3	30	Limit %	Unit	1	2	3	4	5	6	7	8	9
B: Cl2	35	sccm	0.0	0.0	0.0	0.0	0.0	0.0	0.0	0.0	0.0	0.0
C: CF4	20	sccm	40.0	40.0	40.0	40.0	0.0	0.0	0.0	0.0	0.0	0.0
D: O2	0	sccm	0.0	0.0	0.0	0.0	0.0	0.0	0.0	0.0	0.0	0.0
E: Ar	25	sccm	0.0	0.0	0.0	0.0	10.0	10.0	10.0	10.0	0.0	0.0
F: N2	20	sccm	0.0	0.0	0.0	10.0	0.0	0.0	0.0	0.0	100.0	100.0
Pressure		Pa	2.00	1.00	1.00	0.10	2.00	1.00	1.00	2.50	2.50	2.50
Pressure Limit		%	20	70	70	99	70	70	70	70	20	20
Step Time		M:S	00:15	00:05	00:30	<b>00:30</b>	00:15	00:05	<b>01:30</b>	00:10	00:10	00:05
Chamber Deat Time		M:S	00:05	00:05	00:05	00:10	00:05	00:05	00:05	00:05	00:05	00:05
RF (source) Wait Time		M:S	00:05	00:00	00:00	00:10	00:05	00:00	00:00	00:00	00:15	00:00
Vacuuming Time		M:S	00:00	00:00	00:00	00:00	00:00	00:00	00:30	00:00	00:00	00:10
RF (Source) FWD	20	W	500	500	500	0	500	500	500	500	100	50
RF (Source) Ref Limit		W	25	25	25	0	25	25	25	25	25	25
RF (Bias) FWD	20	W	0	0	50	0	0	0	0	200	0	0
RF (Bias) Ref Limit		W	0	0	30	0	0	0	0	30	0	0
C-He Flow Rate	70	sccm	15.0	15.0	15.0	15.0	15.0	15.0	15.0	15.0	0.0	0.0
C-He Pressure	70	Pa	700.0	700.0	700.0	700.0	700.0	700.0	700.0	700.0	0.0	0.0
Use of Esc			DO	DO	DO	DO	DO	DO	DO	DO	DO NOT	DO NOT
Esc Volt1	20	V	1200	1200	1200	1200	1200	1200	1200	1200	0	0
Esc Volt2	20	V	-1200	-1200	-1200	-1200	-1200	-1200	-1200	-1200	0	0
Esc Curr1		µA	200	200	200	200	200	200	200	200	0	0
Esc Curr2		µA	200	200	200	200	200	200	200	200	0	0
Use of EPW			NONE	NONE	NONE	NONE	NONE	NONE	NONE	NONE	NONE	NONE
Use of Over Etching			NONE	NONE	NONE	NONE	NONE	NONE	NONE	NONE	NONE	NONE

Fig. B7 Table of ICP#1 etch conditions

Appendix B: Electroemission Device Design

Process Recipe No	108	RF Soft Start	NO
Title	CL2/N2	Cycle TM	0:00
Comment		Cycle Etch	NO
End Step	5	Cycle Step	0 From 0

Gas F/R	Limit %	Unit	1	2	3	4	5	6
A: BCL3	20	sccm	0.0	0.0	0.0	0.0	0.0	0.0
B: Cl2	20	sccm	22.5	22.5	22.5	0.0	0.0	0.0
C: CF4	20	sccm	0.0	0.0	0.0	0.0	0.0	0.0
D: O2	20	sccm	0.0	0.0	0.0	0.0	0.0	0.0
E: Ar	20	sccm	0.0	0.0	0.0	0.0	0.0	0.0
F: N2	20	sccm	7.5	7.5	7.5	100	100	0
Pre.	20	Pa	2.00	0.20	0.20	2.50	2.50	0.00
VACUING TM		M:S	0:00	0:00	0:15	0:00	0:15	0
RF WAIT TM		M:S	0:15	0:00	0:00	0:15	0:15	0:00
SRC FWD	20 W		500	500	500	100	50	0
SRC REF			20 W					
BIAS FWD	20 W		0	0	100	0	0	0
BIAS REF			20 W					
DEAD TIME		M:S	0:10	0:20	0:20	0:10	0:10	0:00
EPM			NONE	NONE	NONE	NONE	NONE	NONE
STEP TIME		M:S	0:05	0:05	1:30	0:10	0:10	0:00
OVER ETCH		%	0	0	0	0	0	0
OVER ETCH		M:S	0:00	0:00	0:00	0:00	0:00	0:00
END DETECTED								

Fig. B8 Table of ICP#2 etch conditions

## Appendix B: Electroemission Device Design

LED Electroemission Process Flow			
Activation, Dice			
Activate	MOCVD Lab Oven	600°C, 15min, air	<b>DO NOT ACTIVATE WITH INDIVIDUAL SAMPLE</b> Take care not to scratch the EPI surface, replace slide and wipe after each dice
Dice	Back Cleanroom	Using diamond scribe, dice into ~12mm SQ	Alternative is using ADT dicing saw, note SiO2 should be deposited prior to dicing
Dice Alternative	Solvent Bench	Dice using Sapphire settings & blade	Use ultrasonic
Clean	Solvent Bench	Acetone 3min, Isopropanol 3min, DI+Liquinox 3min, DI rinse 3 times	Use ultrasonic
<b>Mesa</b>			
SiO2 deposition	PECVD #1	300 nm SiO2	10 min SiO2 clean, 300 nm
Mesa Lithography	Contact Aligner	HMDS	3000 RMP, 30 Sec, bake at 95C at least 1min
Mesa Lithography	Contact Aligner	PR: nLOF 2020	use 20000 RPM/Sec acceleration to reduce edge bead thickness
Descum	O2 plasma		100 W, 30 sec
Wet etch	HF bench	BHF	1 min, check for undercut & on monitor Si wafer
Mesa etch	ICP #2		See #175
Clean	Solvent Bench	Acetone 3min, Isopropanol 3min, DI+Liquinox 3min, DI rinse 3 times	Use ultrasonic
Remove SiO2	Lithography Wet Bench	BHF	2 minutes
SiO2 deposition	PECVD #1	300 nm SiO2	10 min SiO2 clean, 150 nm + H2O dip +150 nm
<b>n-contact</b>			
Mesa Lithography	Contact Aligner	HMDS	3000 RMP, 30 Sec, back at 95C at least 1min
Mesa Lithography	Contact Aligner	PR: nLOF 2020	100 W, 30 sec
Descum	O2 plasma		1 min, check for undercut & on monitor Si wafer
Wet etch	HF bench	BHF	
HCl Dip	Acid Bench	HCL:DI 1:1, 30 sec	
n-contact Deposition	E-Beam #3	Ti/Au, 30/300 nm	
Liftoff	Solvent Bench	1165, 80C, 10 minutes	Use heated ultrasonic on low intensity
Clean	Solvent Bench	Acetone 3min, Isopropanol 3min, DI+Liquinox 3min, DI rinse 3 times	Use ultrasonic
<b>p-contact</b>			
Mesa Lithography	Contact Aligner	HMDS	3000 RMP, 30 Sec, back at 95C at least 1min
Mesa Lithography	Contact Aligner	PR: nLOF 2020	use 20000 RPM/Sec acceleration to reduce edge bead thickness
UV/Ozone Descum	PR-100	20 min	
Wet etch	HF bench	BHF	1 min, check for undercut & on monitor Si wafer
HCl Dip	Acid Bench	HCL:DI 1:1, 30 sec	
p-contact Deposition	E-Beam #4	Pd/Au, 30/300 nm	E-beam 4 should be used to avoid shadowing of Pd/Au
Liftoff	Solvent Bench	1165, 80C, 10 minutes	Use heated ultrasonic on low intensity
Clean	Solvent Bench	Acetone 3min, Isopropanol 3min, DI+Liquinox 3min, DI rinse 3 times	Use ultrasonic
<b>Isolated p-contact</b>			
Mesa Lithography	Contact Aligner	HMDS	3000 RMP, 30 Sec, back at 95C at least 1min
Mesa Lithography	Contact Aligner	PR: nLOF 2020	use 20000 RPM/Sec acceleration to reduce edge bead thickness
Descum	O2 plasma		100 W, 30 sec
HCl Dip	Acid Bench	HCL:DI 1:1, 30 sec	
Isolated p-contact Deposition	E-Beam #3	Ti/Au, 30/300 nm	
Liftoff	Solvent Bench	1165, 80C, 10 minutes	Use heated ultrasonic on low intensity
Clean	Solvent Bench	Acetone 3min, Isopropanol 3min, DI+Liquinox 3min, DI rinse 3 times	Use ultrasonic
<b>SiO2 removal</b>			
Mesa Lithography	Contact Aligner	HMDS	3000 RMP, 30 Sec, back at 95C at least 1min
Mesa Lithography	Contact Aligner	PR: nLOF 2020	use 20000 RPM/Sec acceleration to reduce edge bead thickness
UV/Ozone Descum	PR-100	20 min	
Wet etch	HF bench	BHF	2 min assure all SiO2 is removed
Clean	Solvent Bench	Acetone 3min, Isopropanol 3min, DI+Liquinox 3min, DI rinse 3 times	Use ultrasonic

Fig. B9 Process flow for electroemission LEDs.

## References

- [1] J. Iveland, L. Martinelli, J. Peretti, J. S. Speck, and C. Weisbuch, "Direct measurement of Auger electrons emitted from a semiconductor light-emitting diode under electrical injection: identification of the dominant mechanism for efficiency droop.," *Phys. Rev. Lett.*, vol. 110, no. 17, p. 177406, Apr. 2013.
- [2] J. Iveland, M. Piccardo, L. Martinelli, J. Peretti, J. W. Choi, N. Young, S. Nakamura, J. S. Speck, and C. Weisbuch, "Origin of electrons emitted into vacuum from InGaN light emitting diodes," *Appl. Phys. Lett.*, vol. 105, no. 5, p. 052103, Aug. 2014.
- [3] "Piranha Solutions," *Princeton University*. [Online]. Available: <https://ehs.princeton.edu/laboratory-research/chemical-safety/chemical-specific-protocols/piranha-solutions>.
- [4] V. L. Alperovich, O. E. Tereshchenko, N. S. Rudaya, D. V. Sheglov, a. V. Latyshev, and a. S. Terekhov, "Surface passivation and morphology of GaAs(100) treated in HCl-isopropanol solution," *Appl. Surf. Sci.*, vol. 235, no. 3, pp. 249–259, Aug. 2004.
- [5] O. E. Tereshchenko, G. É. Sha, A. S. Yaroshevich, and S. V. Shevelev, "Low-Temperature Method of Cleaning p -GaN ( 0001 ) Surfaces for Photoemitters with Effective Negative Electron Affinity," *Phys. Solid State*, vol. 46, no. 10, pp. 1949–1953, 2004.
- [6] A. A. Pakhnevich, V. V. Bakin, A. V. Yaz'kov, G. É. Shaibler, S. V. Shevelev, O. E. Tereshchenko, A. S. Yaroshevich, and A. S. Terekhov, "Energy Distributions of Photoelectrons Emitted from p -GaN ( Cs , O ) with Effective Negative Electron Affinity," *JETP Lett.*, vol. 79, no. 10, pp. 479–483, 2004.